

**CENTRAL NORTH ATLANTIC PALEOCEANOGRAPHY DURING THE
LATE EARLY PLEISTOCENE (SPANNING MARINE ISOTOPE STAGE 21)
BASED ON A HIGH-RESOLUTION DINOFLAGELLATE CYST RECORD**

Mukudzei Mswazi Dube

Department of Earth Sciences

A thesis submitted in partial fulfilment of the degree of M.Sc. in Earth Sciences,

Faculty of Mathematics and Science, Brock University, St. Catharines, Ontario

©2019

ABSTRACT

A high-resolution dinoflagellate cyst record from Integrated Ocean Drilling Program Site U1313, constrained by an ultra-high resolution $\delta^{18}\text{O}$ record from the same sample set, is established to enhance our understanding of the paleoceanography and structure of Marine Isotope Stage (MIS) 21 in the central North Atlantic. Changes in cyst abundance, composition of cyst assemblages, and their diversity reflect major regional shifts in climate and ocean circulation for this time interval (866–814 ka). The following paleoenvironmental indicators are used: *Operculodinium centrocarpum* sensu Wall & Dale (North Atlantic Current), *Nematosphaeropsis labyrinthus* and *Impagidinium pallidum* (subpolar gyre), total *Impagidinium* species (subtropical gyre), and proteridiniacean cysts (biological productivity). The integration of stable isotope and the generated dinoflagellate cyst data shows MIS 21 to have been climatically unstable and interrupted between 830 and 840 ka by two significant cool episodes. These are resolved using the relative abundance of cooler-water species and by tracking the abundance of *O. centrocarpum*. During MIS 21, Site U1313 was predominantly under the influence of the subtropical gyre until after 835 ka when the NAC was re-established until the end of MIS 21. This study also extends the stratigraphic range of *Fibrocysta? fusiforma* from its previously documented range top in the Lower Pleistocene at 2.3 Ma to ~812 ka in the present study. An unnamed *Spiniferites* species (*Spiniferites* sp. 1) is confined to the latest phase of MIS 22. Two unidentified acritarchs (Acritarch spp. 1 and 2) occur throughout MIS 21 and merit further investigation.

Dedicated to my wife and children

ACKNOWLEDGMENTS

I am greatly indebted to Professor Martin J. Head for his endless patience, supervision and guidance in making this research a success; may he continue to be the source of inspiration for many. I am also indebted to Professor Francine McCarthy for her insightful discussions and her ever willingness to lend an ear when needed. Dr. Patrizia Ferretti kindly made available samples used in this study, which were based on her own high-resolution work on the isotopes for IODP Site U1313.

This research was supported a Natural Science and Engineering Research Council of Canada (NSERC) Discovery Grant awarded to Professor Martin J. Head.

Lastly, I would also like to extend my gratitude to all members of staff in the Department of Earth Sciences at Brock for their unwavering support throughout the research.

Table of Contents

1	INTRODUCTION	1
2	BACKGROUND INFORMATION.....	3
2.1	OVERVIEW OF MARINE ISOTOPE STAGES (MIS) 22–19	3
2.1.1	MIS 22 (900–~870 ka)	4
2.1.2	MIS 21 (870–814 ka)	5
2.1.3	MIS 20 (814–790 ka)	11
2.1.4	MIS 19 (790–761 ka)	11
2.2	DINOFLAGELLATES	12
3	STUDY AREA AND SITE LOCATION.....	16
3.1	IODP Site U1313 (41°00'N, 32°58'W) and Modern Oceanography	16
3.2	Lithostratigraphy	18
3.2.1	Unit 1	18
3.2.1.1	Subunit 1A	19
3.2.1.2	Subunit 1B	19
3.2.2	Unit 2	20
4	MATERIALS AND METHODS.....	20
4.1	AGE MODEL	20
4.2	SEA SURFACE TEMPERATURES	21
4.3	STRUCTURE OF MARINE ISOTOPE STAGE 21	22
4.4	SAMPLE SELECTION	22
4.5	SAMPLE PREPARATION	22
4.5.1	<i>PALYNOLOGICAL PROCESSING</i>	22
4.6	DINOFLAGELLATE CYST ANALYSIS	23
4.7	DINOFLAGELLATE CYST TAXONOMY	24
4.8	DINOFLAGELLATE CYST CONCENTRATIONS.....	25
4.9	MODERN DINOFLAGELLATE CYST DATASET.....	26
4.10	MODERN ANALOGUE TECHNIQUE.....	28

4.11	MULTIVARIATE ANALYSIS	30
4.12	OTHER STATISTICAL ANALYSES	33
5	RESULTS	37
5.1	DINOFLAGELLATE CYST COUNTS AND CONCENTRATIONS	37
5.2	DINOFLAGELLATE CYST ASSEMBLAGES AT IODP SITE U1313	40
5.3	COOL WATER SPECIES	43
5.4	AUTOTROPHIC DINOFLAGELLATE CYSTS	47
5.5	HETEROTROPHIC DINOFLAGELLATE CYSTS	48
5.6	EXTINCT DINOFLAGELLATE CYST SPECIES	49
5.7	ACRITARCHS	50
5.8	REWORKED PALYNOMORPHS	52
5.9	MODERN ANALOGUE TECHNIQUE	53
5.10	STATISTICAL ANALYSIS	60
6	DISCUSSION	72
6.1	Dinoflagellate Cysts Preservation and Primary Productivity	72
6.2	<i>Fibrocysta? fusiforma</i> Edwards, 1984	73
6.3	<i>Spiniferites</i> sp. 1	74
6.4	Climate Instability of MIS 21	74
6.5	Paleoceanography changes in the North Atlantic Ocean	76
6.6	Reliability of paleo-reconstructions using MAT	81
7	SUMMARY AND CONCLUSIONS	82
8	REFERENCES	84
APPENDIX A	PLATES	89
APPENDIX B	PALYNOLOGICAL PROCESING AT BROCK UNIVERSITY	95

LIST OF FIGURES

Figure 1. Stable isotope records from IODP Site U1313.	6
Figure 2. Comparison of planktonic and benthic foraminiferal $\delta^{18}\text{O}$ residual from Site U1313 to different insolation records (Laskar et al., 2004):	8
Figure 3. Locations of the cores investigated in the North Atlantic Ocean juxtaposed with the corresponding isotopic correlations for the four interstadials MIS 21.1, 21.3, 21.5 and 21.7	10
Figure 4. Generalized dinoflagellate life cycle (Figueroa and Garces, 2010). Usually only the resistant hypnozygotic cyst fossilizes.	13
Figure 5. The North Atlantic Ocean showing modern mean SSTs, North Atlantic Current, Gulf Stream, North Atlantic Deep Water (NADW) and Arctic Front.	17
Figure 6. Lithostratigraphy of Site U1313 correlated with two other North Atlantic sites (U1312 and U1313) drilled on the same IODP expedition (Backman et al., 2006).	18
Figure 7. Chronology of Site U1313. Sedimentation rates at U1313 (red), carbonate content of DSDP Site 607 .	21
Figure 8. Location of surface sediments samples (red dots) in the n=1207 reference dataset.	27
Figure 9 In-situ dinoflagellate cyst concentrations per gram dry weight of sediment.	40
Figure 10. Abundance/concentration signatures of selected dinoflagellate cysts (a–j) and synoptic diagram of dinoflagellate cyst assemblage compositions (j) for IODP Site U1313.	42
Figure 11. Present geographic distribution of <i>Spiniferites elongatus</i>	43
Figure 12. Present geographic distribution of <i>Impagidinium pallidum</i>	44
Figure. 13. Present geographic distribution of <i>Bitectatodinium tepikiense</i>	45
Figure 14. Relative abundances of cool-related dinoflagellate cyst species	46
Figure 15. Relative abundance of total heterotrophic dinoflagellate cyst species at Site U1313	48
Figure 16 showing semi-crumpled specimens of <i>F.? fusiforma</i>	50
Figure 17. Acritarchs from Site U1313.	51
Figure 18. IODP Site U1313 with respect to the IRD belt in the North Atlantic	52

Figure 19. Results of cross-validation tests using the leave-one-out technique for the combined North Atlantic, Arctic and Pacific (n=1207) dataset	54
Figure 20. Results of cross-validation tests using the leave-one-out technique for the combined North Atlantic, Arctic and Pacific (n=1207) dataset	55
Figure 21. Results of cross-validation tests using the leave-one-out technique for the combined North Atlantic and Arctic (n=667) dataset	56
Figure 22. Plot of planktonic foraminiferal (<i>G. bulloides</i>) $\delta^{18}\text{O}$ data against reconstructed primary productivity, sea surface temperature and sea surface salinity using MAT n=1207.	58
Figure 23. Plot of planktonic foraminiferal (<i>G. bulloides</i>) $\delta^{18}\text{O}$ data against reconstructed primary productivity, sea surface temperature, and sea surface salinity using MAT n=667.	60
Figure 24. Canonical correspondence analysis (CCA) for samples and species in U1313	62
Figure 25. Detrended correspondence analysis plot with dispersion of species in Site U1313	65
Figure 26. Constrained cluster analysis for Site U1313	70
Figure 27. Plot showing species richness and evenness for Site U1313.	71
Figure 28. North Atlantic IODP Site U1314 records from 1069 to 779 ka.	75
Figure 29 Dinoflagellate cyst concentrations.	81

LIST OF TABLES

Table 1. Codes for taxa employed in the DCA analysis in the current study	31
Table 2. Samples analysed for palynology in the present study of IODP Site U1313	34
Table 3. Dinoflagellate cyst and acritarch counts for IODP Site U1313	38
Table 4. Reconstruction measurements for sea surface temperature (SST, in °C) and sea surface salinity (SSS, in PSU) for Site U1313 using the n=1207 modern calibration dataset.	57
Table 5. Reconstruction measurements for sea surface temperature (SST, in °C) and sea surface salinity (SSS, in PSU) for Site U1313 using the n=667 modern calibration dataset.	59
Table 6 Showing results on permutations calculated to the test the null and alternative hypotheses using XLstats software.	61
Table 7 Showing eigenvalues and percentage of inertia for CCA at Site U1313	63

1 INTRODUCTION

The North Atlantic Ocean has long been known to be climatically sensitive and its Quaternary history has been the subject of much palynological research (e.g. de Vernal et al., 2001 and references therein, Hernandez-Almeida et al. 2012, etc.). The study of sediment cores obtained from deep-sea drilling in the high-latitude North Atlantic Ocean has shown that the interval between 1400 and 400 ka was highly variable and characterized by an increase in the amplitude of climate oscillations. It has been referred to as the Early–Middle Pleistocene transition (EMPT) (Head and Gibbard, 2015). The EMPT represents a shift in the overall periodicity of glacial–interglacial cycles from a dominant 41 kyr prior to 0.9 Ma to a dominant Middle Pleistocene ~100 kyr variance (Ferretti et al., 2010; Hernandez-Almeida et al., 2012; Head and Gibbard, 2015). The exact mechanism or cause of this shift is poorly understood although many researchers (Head et al., 2005; Ferretti et al., 2010; Hernandez-Almeida et al., 2012) agree that orbital forces alone cannot explain this structure, with the implication that changes in the internal climate system are involved. In particular, the build-up of ice volume in the northern hemisphere may have resulted in changes in the deep ocean circulation, thereby affecting global climate.

In addition to changes across the EMPT, modelling studies have shown that climate variability at the suborbital scale may reflect a non-linear response to Milankovitch forcing. Milankovitch forcing describes the significant changes in global climate as a response to temporal changes in insolation that are astronomically driven in response to changes in the following parameters: eccentricity, axial tilt, and both axial and perihelion precession. As a consequence, many researchers agree that significant orbital forcing cannot alone explain the internal structure of Quaternary climate cycles, although the exact feedback mechanisms resulting in nonlinearity are still poorly understood and subject to intensive research (e.g., Ferretti et al., 2015). According to Stein et al. (2006), possible causes for these fluctuations may include increases in melt

water volumes delivered to downwelling areas of the northern North Atlantic, interrupting North Atlantic Deep Water (NADW) formation. NADW is formed from the northward flow of warm, saline surface waters that undergo cooling at high latitudes. This further increases their density and causes sinking through convection, ultimately driving global thermohaline circulation (Talley, 2000). Meltwater lowers the surface density, prevents sinking, and disrupts the deep-ocean circulation systems with attendant abrupt changes to the ocean–atmosphere–cryosphere system. Finally, it should be noted that climate cycles may reflect not only the periodicity of the orbital driver but also its harmonics, adding to the complexity of Milankovitch cyclicity (Ferretti et al., 2010).

Advances in studies using ocean surface and sea-floor proxies have provided invaluable information to our understanding of changes occurring in the deep ocean over geological time. Ocean proxies include planktonic and benthic organisms (e.g. planktonic and benthic foraminifera) and their geochemical signatures, and the nature and provenance of accumulated sediments. Micropaleontological records of the North Atlantic (Marino et al. 2000, 2011; Shimada et al. 2008) have shown that variations in the composition and structure of planktonic assemblages are linked to changes in the cold-water system associated with ice-sheet expansion and ice-rafted debris (IRD) throughout the EMPT. Dinoflagellate cysts are used to investigate water mass properties through qualitative and quantitative approaches. Numerous methods and techniques, including the Modern Analogue Technique (MAT) are used: for example Radi and de Vernal (2008) used dinoflagellate cyst quantitative data to reconstruct such sea-surface parameters as temperature (SST), salinity (SSS), primary productivity, and duration of sea-ice cover on an annual or even seasonal/monthly basis. Planktonic foraminifera are also used widely to assess the role of the surface ocean in climate change because the oxygen-isotopic signature within their calcium carbonate tests is related to surface water temperature and salinity as well as global

ice volume (Kucera, 2007). It must be emphasized that while inferences can be made using a single proxy in reconstructing past climate, multiple proxies especially when based on a common sample set, may provide more reliable and nuanced identification of the timing, magnitude, and variability of climatic change.

The present study focuses on the qualitative and quantitative composition of the late Quaternary dinoflagellate cyst record at Integrated Ocean Drilling Program (IODP) Site U1313 in the central North Atlantic. It uses filtrates saved from the samples used by Ferretti et al. (2010) to construct a foraminiferal isotope record through Marine Isotope Stage (MIS) 21. The 111 samples used comprise the upper part of MIS 22, through MIS 21, and the lower part of MIS 20, representing the interval 866–814 ka. In making use of, and complementing, the stable isotope data published by Ferretti et al. (2010), this study aims to refine our understanding of the structure and paleoceanography of MIS 21 in the central North Atlantic. Ferretti et al. (2010) focused on North Atlantic millennial-scale climate variability (910–790 ka) and the role of equatorial insolation forcing. MIS 21 is of particular significance within the EMPT. Representing a recovery after the extensive glaciation of MIS 24–22 (Head and Gibbard, 2015), it is the first climate cycle to develop the distinctly saw-toothed structure that becomes dominant in the later Quaternary. Its unusual structural complexity, seven substages (MIS 21a–g; Railsback et al., 2015) having been defined, is also more characteristic of later Quaternary climate cycles. Therefore, an enhanced understanding of MIS 21 might ultimately yield insights into the EMPT itself.

2 BACKGROUND INFORMATION

2.1 OVERVIEW OF MARINE ISOTOPE STAGES (MIS) 22–19

Marine isotope stages reflect alternating warm and cold periods in Earth's paleoclimate, deduced from isotope data obtained from foraminiferal tests deposited

in deep sea sediment and recovered in core samples. In-depth analysis of sediment cores obtained from the high-latitude North Atlantic has demonstrated the persistence of cyclical ice-volume variation accompanied by global climate changes (Hernandez-Almeida et al., 2012). The large build-up of ice sheets in the northern hemisphere is linked to the higher-amplitude climate oscillations experienced during the EMPT (Ruddiman, 2006). According to Head and Gibbard (2005, 2015), during the EMPT, low-amplitude 41 ka obliquity-forced cycles were progressively replaced by high-amplitude asymmetrical quasi-100 ka cycles that point to a slow ice build-up and rapid melting, implying a transition to a strongly non-linear forced climate system.

2.1.1 MIS 22 (900–~870 ka)

This glacial stage is considered the first of the major cold events that typify glaciations of the later Pleistocene and the most severe of the Early Pleistocene (Head and Gibbard, 2005, 2015). It may be related to the weak preceding interglacial MIS 23. MIS 22 was characterized by a large increase in ice volume in the Northern Hemisphere which caused a subsequent drop in sea level of 20–30 m compared with the earlier glaciation during MIS 28 (Kitamura and Kawagoe, 2006). Climatic events during MIS 22 seem to be influenced by an obliquity-driven climate cycle, characterized by an increase in millennial scale fluctuations in climate suggesting further the link with an increase in ice-sheet growth (Weirauch et al., 2008). MIS 22 was also associated with significant changes in oceanic circulation. The study of deep-water carbon isotope signals during MIS 22 reflects a depletion of ^{13}C , which can be associated with the transfer of carbon from organic to inorganic pools in the ocean during a global event (Clark et al., 2006). Benthic ^{13}C reached its most depleted levels in both the Pacific and Atlantic oceans in the last 5 million years during MIS 22, resulting from the 120-m sea-level lowstand exposing continental shelves globally and facilitating an increase in transport of organic carbon into the oceans (Raymo et al., 1990). Overwhelming

evidence across continents, and marine indicators including nannofossil assemblage changes as studied at eastern North Atlantic Ocean Drilling Program (ODP) Site 980/981, all reflect severe cooling (Marino et al., 2011). Indeed, nearly barren intervals in the foraminiferal record of the central Arctic Ocean testify to the severity of the glaciation at the time.

2.1.2 MIS 21 (870–814 ka)

Several studies on the EMPT (Muttoni et al., 2013; Ferretti et al., 2010; Kender et al., 2013) show MIS 21 to have been climatically unstable. The preceding stage (MIS 22) is noted to be the first prominent cooling event and glacioeustatic lowstand of the Pleistocene (Ferretti et al., 2010). MIS 22 was characterized by a large increase in ice volume over North America which caused a subsequent drop in sea level by between 20 and 30 m more than during MIS 28 (Kitamura and Kawagoe, 2006), as already mentioned. Presently, MIS 21 (Figure 1) has seven assigned substages (MIS 21.1–21.7) according to the work of Ferretti et al. (2010) and MIS 21a–g by Railsback et al. (2015). Rudman et al. (1986) treated MIS 21 as a single obliquity cycle, whereas Hilgen (1991) assigned it to two obliquity cycles, and Shackleton et al. (1990) and Bassinot et al. (1994) considered it to have three precession peaks. The seven substages of MIS 21 are evident in many reconstructed marine records (Hodell et al., 2008; Naafs et al., 2011), but less clearly so in LR04. These precession peaks parallel the seven lettered substages recognized by Railsback et al. (2015).

Ferretti et al. (2010) subdivided MIS 21 into four interstadials using foraminiferal isotopic data from IODP Site U1313 in the central North Atlantic Ocean, core being sampled continuously at 1 cm spacing. Records were obtained from the planktonic *Globigerina bulloides* and the benthic *Cibicidoides wuellerstorfi* and range from MIS 23 to MIS 20. The planktonic (*G. bulloides*) record of MIS 21 revealed four discrete peaks that Ferretti et al. (2010) labelled MIS 21.1, 21.3, 21.5 and 21.7 (Figure 1).

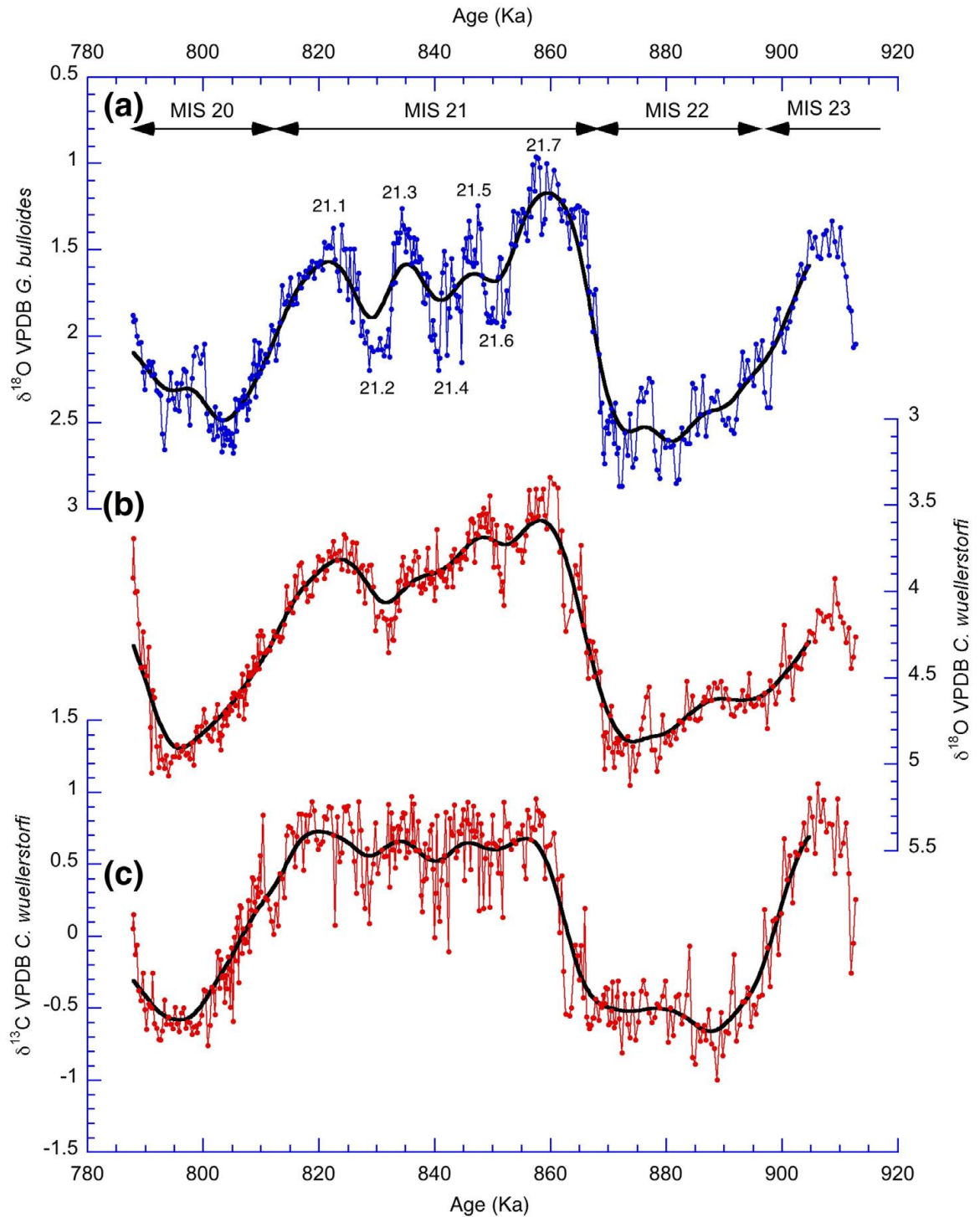


Figure 1. Stable isotope records from IODP Site U1313. (a) *Globigerina bulloides* $\delta^{18}\text{O}$; (b) *Cibicidoides wuellerstorfi* $\delta^{18}\text{O}$; (c) *C. wuellerstorfi* $\delta^{13}\text{C}$ (thin lines with data point markers). The $\delta^{18}\text{O}$ values of *C. wuellerstorfi* were adjusted by +0.64‰ to bring them into presumed oxygen isotopic equilibrium with ambient sea water (Shackleton and Opdyke, 1973). Also shown is the Gaussian interpolation of the three isotopic records using a 15 kyr Gaussian window (thick line without marker) (Ferretti et al., 2010, fig. 2.)

Early work on MIS 21 shows that the number of cycles identified may depend on the resolution of the record, the region, and climate proxy studied (Ferretti et al., 2010). For example, Ruddiman (1986) compressed this stage into a single obliquity cycle in Deep Sea Drilling Project (DSDP) Site 607, whereas Hilgen interpreted it as having two obliquity cycles. Ferretti et al. (2010) were able to correlate the four interstadials at Sites 983, U1308 and 1063 across the North Atlantic (Figure 3) and suggested that the frequency of these cycles cannot be explained by simple orbital geometry. The four peaks from Site U1313, correlated across the North Atlantic (Figure 3), confirm that these events were recorded at various ocean depths and latitudes, showing that benthic isotope variations are a reflection of regional deep ocean circulation and not a mere reflection of localized processes (Ferretti et al., 2010). Of interest, is the difference in amplitude of the $\delta^{18}\text{O}$ signal across the correlated sites. Site 983, located shallower in the depth transect than other sites under the same influence of deep-source waters of the NADW (U1308, U1313 and 1063), has a $\delta^{18}\text{O}$ record reflecting warmer intermediate source waters. However, according to Ferretti et al. (2010), temperature alone is not enough to account for the disparity in benthic $\delta^{18}\text{O}$ between Site 983 and the other deeper sites, and salinity changes could have also played a major role.

There is strong agreement in the $\delta^{18}\text{O}$ residual records (between benthic and planktonic foraminifera) and insolation at the equator during the equinoxes (Figure 2). The two oxygen isotope records closely mimic the amplitude of insolation, with both the *G. bulliodes* and *C. wuellerstorfi* $\delta^{18}\text{O}$ records between ~880 to ~830 ka mirroring the multiple high-amplitude insolation variations.

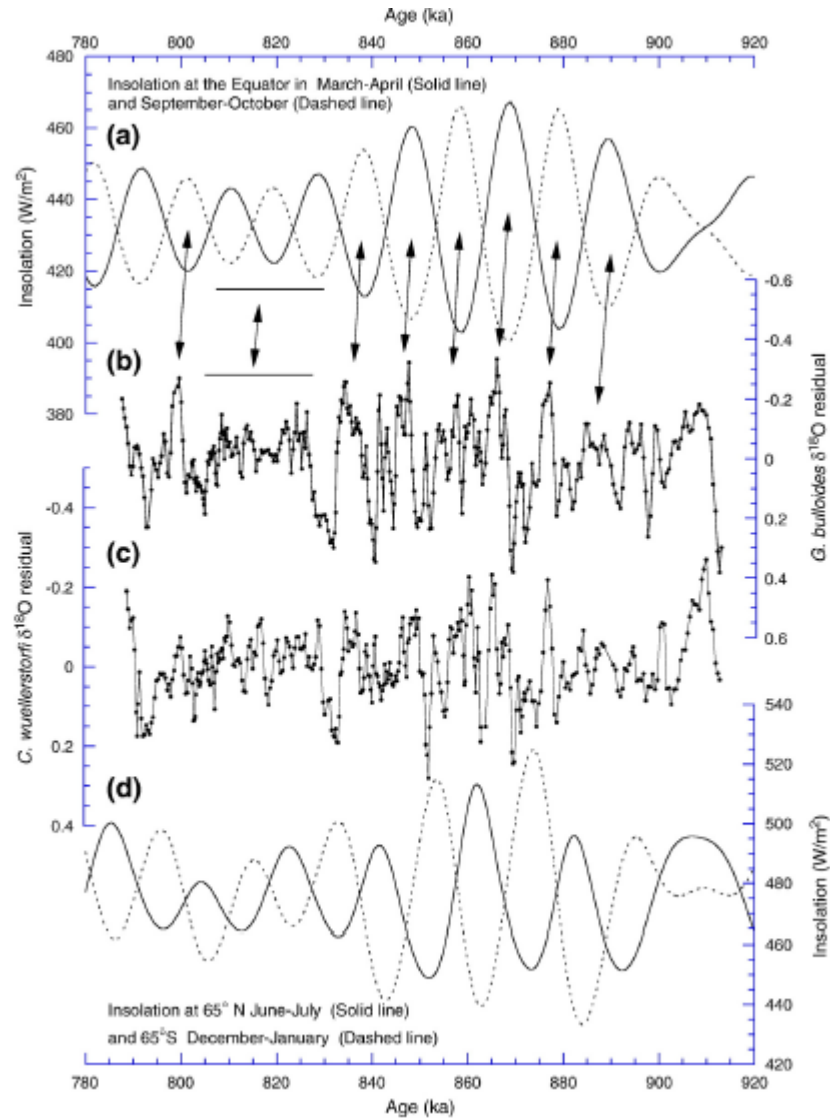


Figure 2. Comparison of planktonic and benthic foraminiferal $\delta^{18}\text{O}$ residual from Site U1313 to different insolation records (Laskar et al., 2004): (a) the insolation at the equator in spring (solid line) and autumn (dashed line); (b) the residual obtained by subtracting the Gaussian interpolation from the measured records of *Globigerina bulloides* $\delta^{18}\text{O}$; (c) the residual obtained by subtracting the Gaussian interpolation from the measured records of *Cibicidoides wuellerstorfi* $\delta^{18}\text{O}$; (d) Northern Hemisphere summer insolation (65°N, June–July) (solid line) and Southern Hemisphere summer insolation (65°S, December–January) (dashed line). (Ferretti et al., 2010, fig. 6.)

Ferretti et al. (2010) found clear evidence of millennial-scale variability in the time series analysis of benthic and planktonic oxygen isotope records at periods of 10.7 and 6 kyr, which corresponds to the second and fourth harmonics of precession cycles. The climate signal at Site U1313 is interpreted to be a result of low-latitude insolation

with the equatorial response being advected to the high latitudes through oceanic and atmospheric circulation and amplified possibly by moisture feedback. The 10.7 and 6 kyr cycles recorded at U1313 provide support for a linked atmosphere-ocean-cryosphere system controlled by low-latitude insolation forcing at these periodicities.

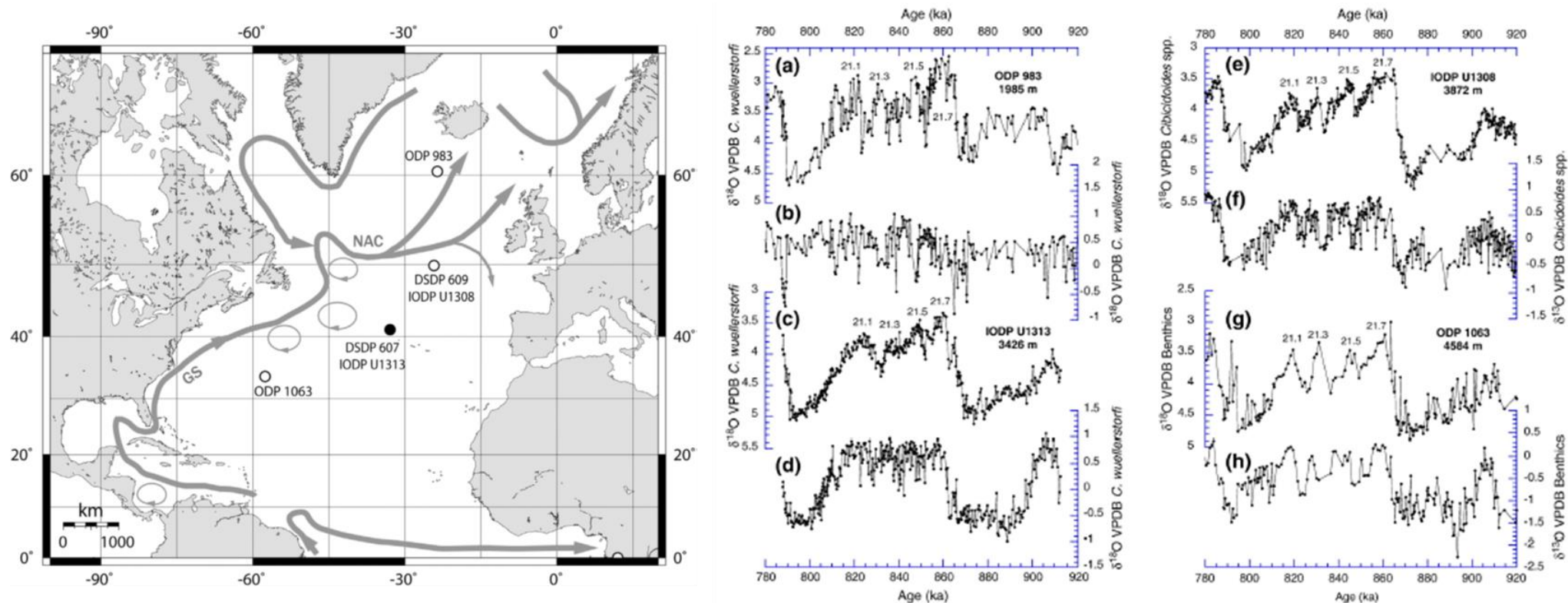


Figure 3. Locations of the cores investigated in the North Atlantic Ocean juxtaposed with the corresponding isotopic correlations for the four interstadials MIS 21.1, 21.3, 21.5 and 21.7 identified by Ferretti et al. (2010): Major surface water currents are from Frantantoni (2001): GS=Gulf Stream; NAC=North Atlantic Current (Ferretti et al., 2010, fig 1). Oxygen (a) and carbon (b) isotope records for benthic foraminifera *Cibicides wuellerstorfi* from ODP Site 983 (Kleiven et al., 2003). Oxygen (c) and carbon (d) isotope records for benthic foraminifera *C. wuellerstorfi* from IODP Site U1313 (Ferretti et al., 2010). Oxygen (e) and carbon (f) isotope records for benthic foraminifera *C. wuellerstorfi* and *C. kullenbergi* from IODP Site U1308 (Hodell et al., 2008). Oxygen (g) and carbon (h) isotope records for benthic foraminifera from ODP Site 1063 (Ferretti et al., 2005) (Ferretti et al., 2010, fig. 5).

2.1.3 MIS 20 (814–790 ka)

MIS 20 represents a short-lived and severe glacial event, characterized by relatively high (for a glacial cycle) summer insolation values (65°N) as a result of low precession/eccentricity and obliquity forcing (Head and Gibbard, 2015). MIS 20 was characterized by a global sea level drop of about 120m, with a slightly heavier isotope maximum than for MIS 22. According to Anastasakis and Piper (2005), stratigraphic evidence studied off the coast of Greece supports a more severe eustatic drop during MIS 20 than recorded during MIS 16. During MIS 20, alkenone-based SSTs at northern North Atlantic ODP Site 983 show a drop of 6°C with a simultaneous increase in the geochemical proxy %C_{37:4} for arctic-sourced waters (McClymont et al., 2008). Notably, a significant decline among “extinction group” deep-sea foraminifera is recorded in the SW Pacific Ocean and elsewhere starting in the late MIS 21–20 transition (Hayward et al., 2007).

2.1.4 MIS 19 (790–761 ka)

Based on its astronomical and paleoclimate signature, MIS 19 appears to be the closest analogue of the present interglacial. This is associated with the lowered amplitude of the 400-ky eccentricity cycle in both stages (MIS 1 and MIS 19), resulting in the suppression of precessional forcing (Head and Gibbard, 2015). The widely documented Younger Dryas cooling event is associated with deglaciation during MIS 1. In addition, numerous widely distributed locations, including Site IODP U1308 in the North Atlantic, Lake Baikal, Montalbano Jonico in Southern Italy, and ODP Site 1123 in the south western Pacific (Hodell et al., 2008; Prokopenko et al., 2006; Elderfield et al., 2012), show a Younger Dryas-like event just prior to MIS 19. The Matuyama–Brunhes Chron boundary lies in the upper part of MIS 19 at around 773 ka, and serves as primary guide to the Early–Middle Pleistocene boundary. According to Elderfield et al (2012), the MIS 20–19 transition is characterized by a rapid lightening of isotope values which represents a lowstand–highstand eustatic rise from minus 120m to plus

20m relative to present sea level. Montalbano Jonico, a former candidate Global Boundary Stratotype Section Point (GSSP) located in southern Italy, shows detailed changes through MIS 19. During MIS 19.3, conditions were similar to the present day, and during MIS 19.2 conditions were possibly drier and cooler with a lowering of the sea level at this site (Marino et al., 2015).

2.2 DINOFLAGELLATES

Dinoflagellates are unicellular protists belonging to the division Dinoflagellata. They inhabit various types of aquatic environments including lakes, estuaries, epicontinental seas, and oceans. Dinoflagellates have complex life cycles involving several stages, asexual and sexual, motile and non-motile (Figure 4). However, with a few exceptions only dinoflagellates that produce resting cysts leave a fossil record. Resting cysts may allow survival during unfavourable conditions, and aid in dispersal (Mertens et al., 2012). Dinoflagellates exhibit various feeding strategies that include autotrophy (photosynthesis), heterotrophy, and symbiosis with marine invertebrates such as corals (de Vernal et al., 2013). Autotrophic dinoflagellates live in the photic zone at relatively shallow depths within the upper 50–100 m where they can access light and nutrients. Heterotrophic dinoflagellates depend on the overall biological activity of the environment and hence are found in areas in which their prey exist.

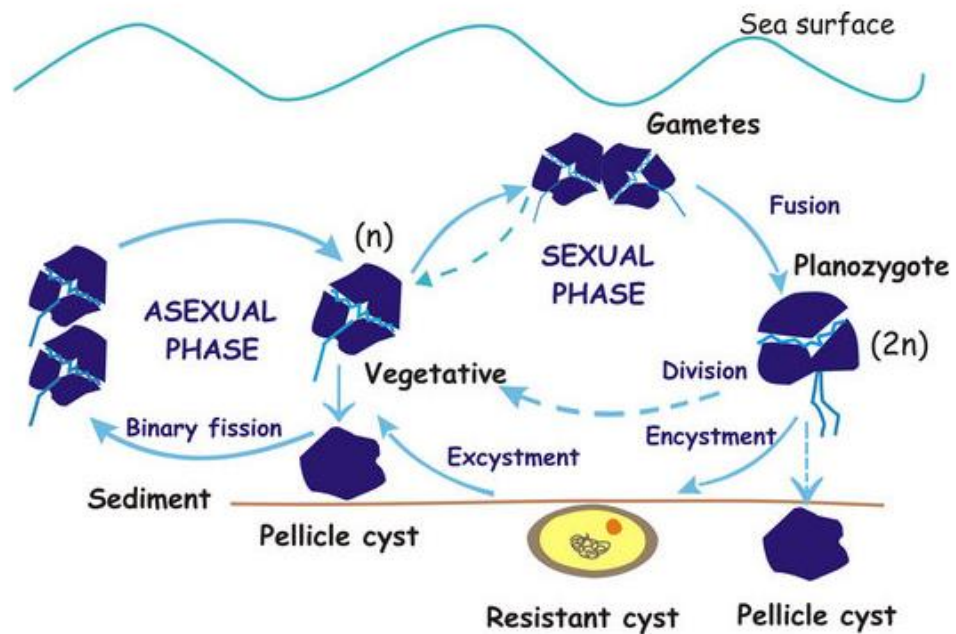


Figure 4. Generalized dinoflagellate life cycle (Figueroa and Garces, 2010). Usually only the resistant hypnozygotic cyst fossilizes.

Dinoflagellate cyst assemblages found in sediments play a key role in reconstructing hydrographic parameters that include, temperature, salinity, sea ice cover, nutrient levels, and productivity. Quantitative palaeoceanographic reconstructions for the Quaternary using dinoflagellate cysts mostly rely on databases developed from studies of surface sediments linked to observations of modern hydrographic parameters. Transfer functions (a mathematical operation) apply modern assemblage data to interpret fossil assemblages and thereby derive quantitative estimates of sea surface conditions such as temperature and salinity back through time (de Vernal et al., 2013). This approach has been used to identify hydrographic changes in the North Atlantic Ocean during the Quaternary (e.g. de Vernal et al., 2001). Most palaeoceanographic reconstructions based on dinoflagellate cyst data are conservative in that they are based on the modern analogue technique (MAT) which uses interpolation and is therefore heavily dependent on the modern calibration set (de Vernal et al., 2001). The MAT measures the degree of similarity between fossil dinoflagellate cyst assemblages

and modern distributions, assuming that they represent comparable environmental conditions. Dinoflagellate-cyst based transfer functions accordingly reconstruct summer and winter sea surface temperatures (SST), months of ice cover, and sea surface salinity (SSS) with high correlations between produced and measured environmental values, producing low predictive errors (Telford, 2006). However, these low predictive error values have been viewed with scepticism, and the robustness of these reconstructions therefore called into question (Dale, 1996, 2001, 2006). It is argued that the use of transfer functions ignores the strong spatial structure of the dataset and hence the low values in the predictive errors. The bias is introduced if observations are not evenly distributed along the environmental gradient (Telford and Birks, 2001). For the under-sampled portions of the environmental gradient, the uncertainty can be larger than the root mean squared error of prediction (RMSEP) and for the over-sampled portions the uncertainty can be smaller than the RMSEP (Telford and Birks, 2001). According to Telford (2006), the dinoflagellate cyst calibration sets exhibit strong spatial autocorrelation, but the estimates of transfer function performance statistics used in MAT assume that these calibration set observations are independent, and this exaggerates the performance of the transfer functions. In defence, Guiot and de Vernal (2011) argued that the spatial autocorrelation for a dinoflagellate cyst database with a large environmental gradient does not affect MAT more than other transfer techniques being used. Aside from statistical issues is the affect of transport, which displaces a cyst from the surface waters in which it was produced to its final resting place on the ocean floor. This reduces the reliability of any transfer function using any planktonic microfossil group. Dale (2006) has remarked that the reliability of transfer functions can be improved by using and applying a calibration data set and core samples from areas of high local production with minimal cyst transport (continental shelf). The application of MAT in marine environments which is inherently spatially structured is problematic as this method ignores this aspect.

Eutrophication, productivity, and upwelling have a strong influence on dinoflagellate assemblages in any environmental setting. Studies conducted along the coasts of Europe, America, Japan, and elsewhere have shown increased fluxes of dinoflagellates along with higher percentages of heterotrophic taxa (notably cysts of *Protoperidinium* spp.) due to increased nutrient levels. The occurrence of nutrient upwelling in oceanic environments results in increased productivity particularly among diatoms and other primary producers, followed by the heterotrophic dinoflagellates that feed on them (e.g., Pospelova et al., 2008; Radi and de Vernal, 2004).

3 STUDY AREA AND SITE LOCATION

3.1 IODP Site U1313 (41°00'N, 32°58'W) and Modern Oceanography

IODP Site U1313 is located approximately 400 km WNW of the Azores in the North Atlantic on the middle western flank of the Mid-Atlantic Ridge (Figure 5) at a depth of 3426 m. This site was chosen to obtain Miocene to Quaternary sedimentary records of the North Atlantic that would improve understanding of paleoenvironmental variability in terms of ice sheet–ocean interactions, deep ocean circulation, and sea-surface conditions (Channell et al., 2010). This site is a re-occupation of DSDP Leg 94, Site 607 drilled in 1983. U1313 was drilled during the months of March and April in 2005 during Expedition 306 of the IODP. The rationale for re-occupying DSDP Site 607 is that it constitutes a benchmark for long-term (millions of years) as well as short-term surface and deep ocean climate records from the subpolar North Atlantic (Expedition 306 Scientists, 2006). This site is in an open ocean setting and lies at the northern margin of the North Atlantic subtropical gyre. Today, it is predominantly under the influence of the surface waters of the North Atlantic Current; while on the ocean floor, at a depth of 3426 m, it is under the influence of NADW (Ferretti et al., 2015).

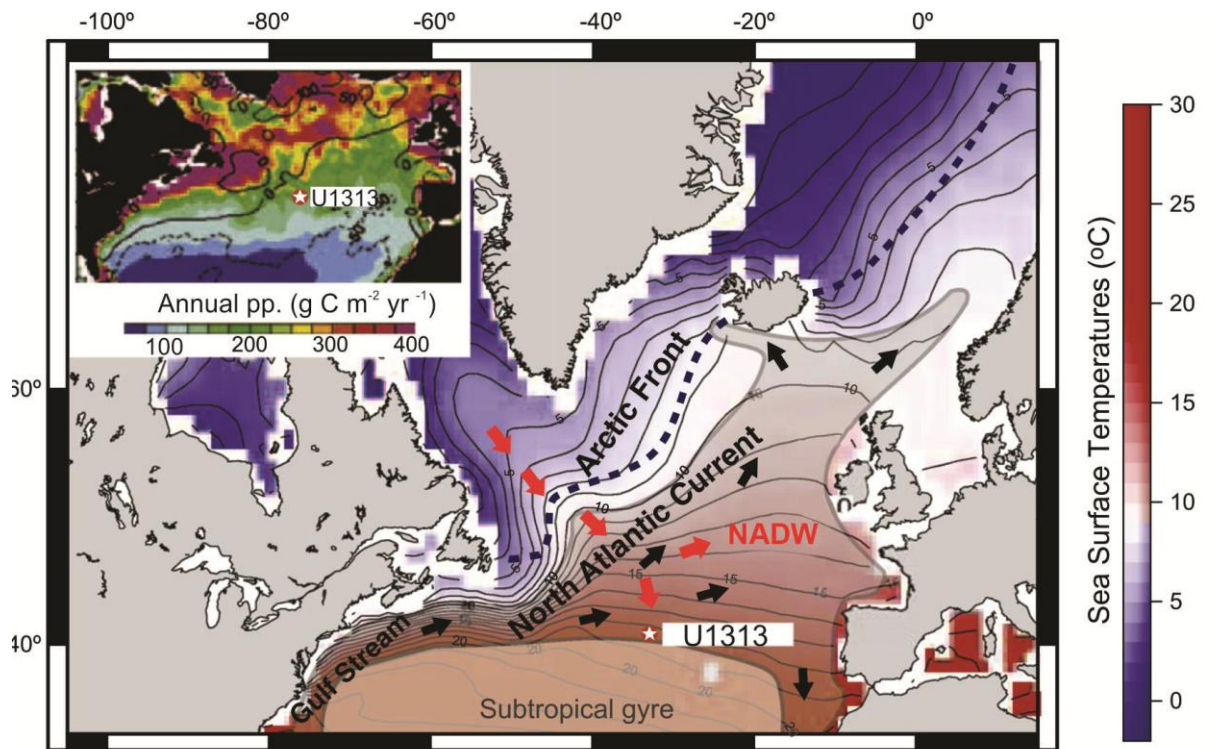


Figure 5. The North Atlantic Ocean showing modern mean SSTs, North Atlantic Current, Gulf Stream, North Atlantic Deep Water (NADW) and Arctic Front. Black arrows indicate surface currents. Red arrows indicate deep water masses. Insert shows annual primary productivity (Mantilla, 2013 modified from Naafs et al., 2010, fig. 1).

CaCO_3 and benthic $\delta^{18}\text{O}$ and $\delta^{13}\text{C}$ records for the Pleistocene are of paramount importance for understanding the influence of NADW over time (Ruddiman et al., 1989). In addition, the location of Site U1313 in the northern most part of the oligotrophic subtropical gyre, in close proximity to the nutrient-enriched subpolar gyre system, makes it ideal for studying the near-surface-water response of the North Atlantic to climate change. Climate change would influence the movement of either gyre system north or south of the location of U1313. Four holes were drilled at Site U1313 (U1313A, U1313B, U1313C and U1313D) to construct a composite section down into the Upper Miocene using an advanced hydraulic piston coring (APC) system and nonmagnetic core barrels to a maximum depth of 308.64, 302.67, 293.45, and 152.34 mbsf, respectively (Expedition 306 Scientist, 2006).

3.2 Lithostratigraphy

The sedimentary succession at Site U1313 comprises mainly nannofossil ooze with varying amounts of foraminifera with some clay to gravel-size terrigenous components. Two major lithological units are identified. Unit 2 is not covered in detail as it falls outside of the interval of interest in this study. Unit 1 is further subdivided into subunits based on changes in the percentage of variability of clay and nannofossil content (Figure 6).

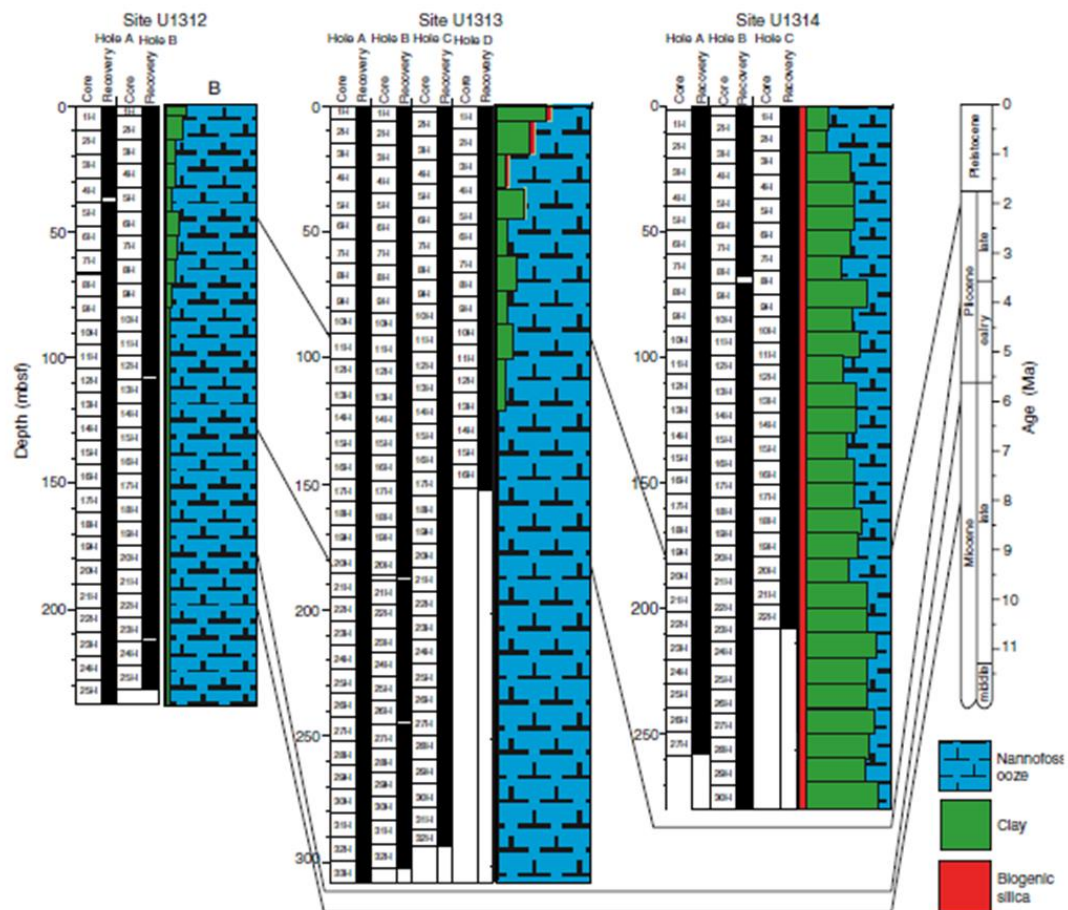


Figure 6. Lithostratigraphy of Site U1313 correlated with two other North Atlantic sites (U1312 and U1313) drilled on the same IODP expedition (Backman et al., 2006).

3.2.1 Unit 1

This unit comprises mainly silty-clay nannofossil ooze, nannofossil ooze with clay, and nannofossil ooze with variable colours (grey, light grey and white). The unit is defined by centimetre- to decimetre-scale variability in detrital clay and biogenic carbonate with decreased variability downcore. This unit spans 0–111.86 meters below sea floor (mbsf) in Hole U1313A, 0–111.28 mbsf in Hole U1313B, 0–112 mbsf in Hole U1313C and 0–113.14 mbsf in Hole U1313D, and it represents deposition spanning the Early Pleistocene through Holocene (Backman et al., 2006). Lithological variability in this unit can be seen visually through colour changes on a centimetre to decimetre scale. The present interval of study occurs within Subunit 1A and Subunit 1B.

3.2.1.1 Subunit 1A

The top part of this sedimentary succession is made up of silty-clay nannofossil ooze (~65 cm) and has a characteristic yellow-brown colour caused by the interaction of sediments with oxygen rich sea-waters leading to oxidation. The remainder of the subunit consists of nannofossil silty clay, silty clay nannofossil ooze, nannofossil ooze with clay, nannofossil ooze, and subordinate intervals of silty clay nannofossil ooze with diatoms and nannofossil ooze with diatoms and clay. Depths of Subunit 1A are 0–41.00 mbsf in Hole U1313A, 0–39.38 mbsf in Hole U1313B, 0–41.08 mbsf in Hole U1313C, and 0–39.7 mbsf in Hole U1313D, this subunit representing deposition mostly during the Middle Pleistocene–Holocene. Colour variations are noted in this unit (white, grey, light grey, light olive grey and olive grey).

3.2.1.2 Subunit 1B

This subunit consists of nannofossil ooze, nannofossil ooze with clay, and silty clay nannofossil ooze. This subunit also displays colour variations (white, light grey and grey) reflecting a decimetre-scale variation in clay and biogenic carbonate content. Subunit 1B spans 41–111.86 mbsf in Hole U1313A, 39.38–111.28 mbsf in Hole U1313B, 41.08–112.00 mbsf in Hole U1313C, and 39.7–113.14 mbsf in Hole U1313D.

The time interval represented by Subunit IB is Early Pleistocene (Backman et al., 2006).

3.2.2 Unit 2

Unit 2 consists of nannofossil ooze of latest Miocene – Late Pliocene age. The transition from Unit 1 to Unit 2 is gradational over approximately 40 m. This unit spans 111.86–308.64 mbsf in Hole U1313A, 111.28–300.67 mbsf in Hole U1313B, 112.00–293.45 mbsf in Hole U1313C, and 113.14–152.34 mbsf in Hole U1313D.

4 MATERIALS AND METHODS

4.1 AGE MODEL

The age model adopted for this study for Site U1313 is taken from Naafs et al. (2011) which makes use of the adjusted composite meter depth (amcd), an update of the original meter composite depth (mcd) scheme that enhances the correlation of features in the lightness, magnetic susceptibility and paleomagnetic data between the four holes (U1313A, U1313B, U1313C and U1313D). The model makes use of $\delta^{18}\text{O}$ data from the benthic foraminifer *Cibicidoides wuellerstorfi* in addition to other previously published data (Stein et al., 2009; Ferretti et al., 2010; Voelker et al., 2010). All benthic foraminiferal $\delta^{18}\text{O}$ data from U1313 for the interval between 960 and 320 ka were tuned to the LR04 stack (Lisiecki and Raymo, 2005). At the same time the lightness of the primary splice (L^*) from U1313 was tuned to the carbonate content of DSDP Site 607 (Ruddiman et al., 1989), Site 607 being part of the LR04 stack (Figure 7).

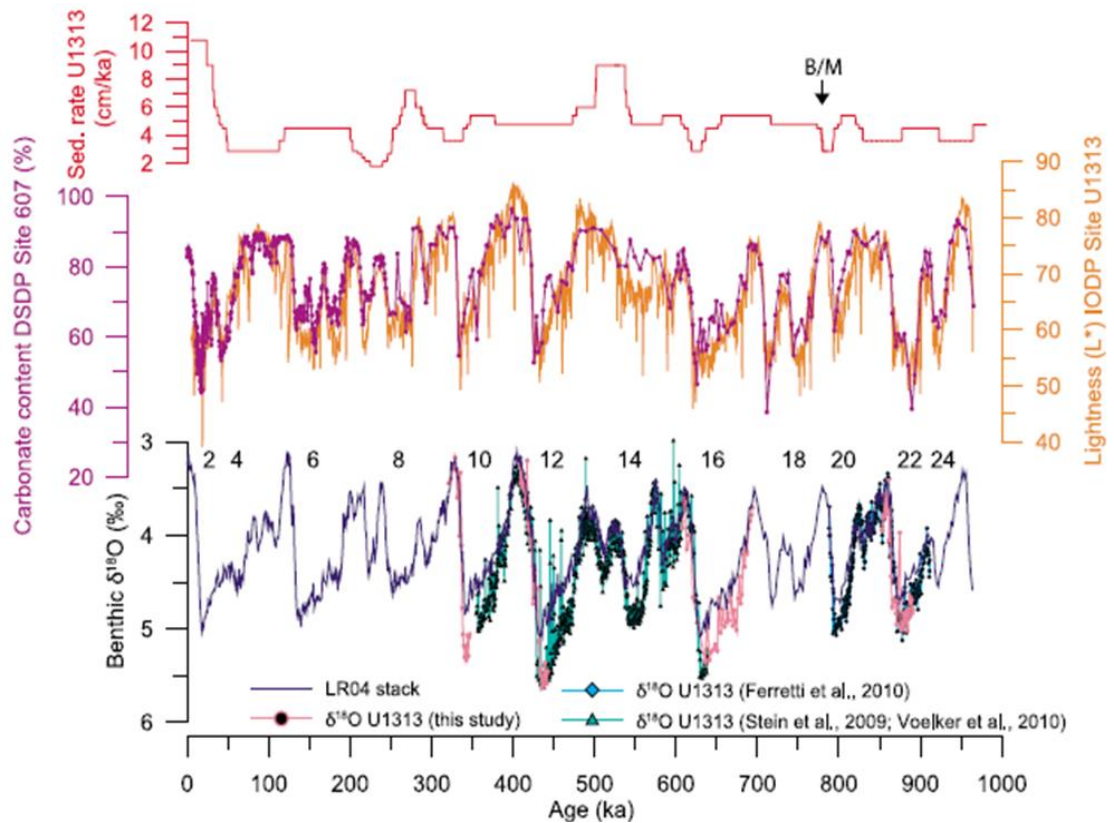


Figure 7. Chronology of Site U1313. Sedimentation rates at U1313 (red), carbonate content of DSDP Site 607 (Ruddiman et al., 1989) (purple), together with lightness of the primary splice from U1313 (orange), and benthic $\delta^{18}\text{O}$ of Site U1313 (Stein et al., 2009; Ferretti et al., 2010; Voelker et al., 2010; this study) together with the global benthic $\delta^{18}\text{O}$ stack (Lisiecki and Raymo, 2005). Arrow with B/M indicates the position of the Matuyama/Brunhes paleomagnetic boundary (Naafs et al., 2011).

4.2 SEA SURFACE TEMPERATURES

Alkenones and Mg/Ca ratios have been widely used in paleoceanography for assessing past sea-surface temperature (SST) changes. Naafs et al. (2011) used alkenones along with Mg/Ca ratios on the planktonic foraminifer *Globigerina bulloides* to reconstruct mean sea-surface paleotemperatures at IODP Site U1313. In this study, I make use of the age model developed by Naafs et al. (2011) and adopt the postulated MIS boundaries of that publication. The ages of the MIS boundaries follow the work of Lisiecki and Raymo (2005) and are available from: http://www.lorraine-lisiecki.com/LR04_MISboundaries.txt.

4.3 STRUCTURE OF MARINE ISOTOPE STAGE 21

Several studies on the EMPT (Muttoni et al., 2013; Ferretti et al., 2010; Kender et al., 2013; Head and Gibbard., 2015) show MIS 21 to have been climatically unstable. The preceding stage (MIS 22) is noted as being the first prominent cooling event and glacioeustatic lowstand of the Pleistocene (Ferretti et al., 2010). MIS 22 was characterized by a large increase in the ice volume in North America which caused a subsequent drop in sea level by more than 20 to 30 m more than during MIS 28 (Kitamura and Kawagoe, 2006) (see Chapter 2). MIS 21 (Figure 1) has seven assigned substages (MIS 21.1–21.7) according to the numerical nomenclature used by Ferretti et al. (2010) and MIS 21a–g based on the alphabetical nomenclature of Railsback et al. (2015).

4.4 SAMPLE SELECTION

Samples used in the present study were obtained from the published research of Ferretti et al. (2010) in which benthic and planktonic foraminifera from Site U1313 were analysed for isotopes at the University of Cambridge, U.K. The sediment samples were prepared in that study by disaggregation in an orbital shaker, and wet sieving at 63 µm using reverse osmosis water to retain the foraminifera for isotopic analysis (Ferretti et al., 2010). The <63 µm filtrate was then dried overnight at 50°C and stored. This stored <63 µm sediment fraction was made available to us by Dr. Patrizia Ferretti (now at the University of Venice), and was processed for palynology at Brock University (Section 4.5.1 below). A total of 240 samples were provided within the chosen interval of study (866–814 ka). However, owing to limitations of time, alternate samples were selected for processing and this resulted in the analysis of 111 samples for palynology (Table 2). These samples are from a splice using Holes U1313D and U1313A. Samples were grouped into five batches for palynological processing.

4.5 SAMPLE PREPARATION

4.5.1 PALYNOLOGICAL PROCESSING

The dried <63 µm fraction from each sediment sample was processed using standard palynological processing methods at Brock University. This involves demineralizing the sample using hydrochloric acid (HCl) and hydrofluoric acid (HF) to release palynomorphs from the sediment matrix (Riding and Kyffin-Hughes, 2004). The 111 samples were weighed, crushed and treated initially with cold 20% concentrated HCL for 72 hours to remove carbonates. After neutralizing with distilled water to pH 6 (the pH of distilled water), the samples were further macerated for five days using cold 48% HF to demineralize and remove silica. The resultant samples were neutralized again to a pH 6 through a repetitive process of centrifugation and decanting. One tablet of *Lycopodium clavatum* (Batch # 1031; $x=20848$, $s= \pm 3457$) was added to each sample to permit the statistical estimation of its dinoflagellate cyst concentration (Table 2). To each sample, 30 ml of 3% wt. sodium metahexaphosphate solution was added and the sample placed in a warm water bath for 30 minutes to remove excess amorphous organic material (AOM). Safranin-o stain was then added to samples to increase dinoflagellate cyst visibility, after which the residue was then sieved through a 10 µm nylon mesh. A wet preparation was made for each sample after sieving to check that each residue was well sieved and to ensure excessive AOM had been removed.

The resultant sample residue with concentrated palynomorphs was mounted onto a microscope slide using a glycerine jelly following the method of Evitt (1984). A duplicate slide was made for each sample sieved, where sufficient residue was available. A combined total of 190 slides were made for samples processed for IODP Site U1313.

4.6 DINOFLAGELLATE CYST ANALYSIS

Qualitative and quantitative data were obtained from the palynological analysis of mounted slides using a Leica DM2500 transmitted light microscope at Brock University. Dinoflagellate cysts were identified either to genus or species level

depending on the preservational state and orientation of specimens. Dinoflagellate cysts were counted using a 40x dry objective lens. A 100x oil objective lens was used to identify folded and poorly oriented specimens and to study the morphology of uncommon taxa.

Other palynomorphs including pollen, algae and invertebrate fragments were also counted to aid taphonomic interpretation. Each sample was counted ideally until 300 dinoflagellate cysts had been enumerated, but not all samples yielded this number of cysts (Table 3).

4.7 DINOFLAGELLATE CYST TAXONOMY

Dinoflagellate cysts were identified to the highest taxonomic resolution possible, at least to the genus and where possible the species. Taxonomy and nomenclature used in this study largely follow Rochon et al. (1999) and De Schepper and Head (2008). Rochon et al. (1999) contains an extensive database documenting the distribution of dinoflagellate cysts in surface sediments from the North Atlantic Ocean and adjacent seas, allowing site-to-site comparison of assemblages. The database has 41 taxa. In the present work, *Operculodinium centrocarpum* refers to the cyst commonly known in the Quaternary literature as *Operculodinium centrocarpum* sensu Wall and Dale (1966) and which has been shown to be the cyst of *Protoceratium reticulatum* (Paez-Reyes & Head, 2013). Several taxa were grouped together on the basis of morphological similarities. For example, *Spiniferites elongatus* and *Spiniferites frigidus* are grouped as *Spiniferites elongatus*, and species of the genus *Brigantedinium* (mostly comprising *B. simplex* and *B. cariacense*) are grouped as *Brigantedinium* spp. because the folding or poor orientation of specimens may prevent the observation of their archeopyle and hence hinder identification to species level. *Spiniferites mirabilis* and *S. hyperacanthus* were grouped together as the *Spiniferites mirabilis* group because of the difficulty in distinguishing one from the other when unfavourably oriented

(Rochon et al., 1999). In addition, several marine palynomorphs lacking clear dinoflagellate attributes were documented as acritarchs, and placed in open nomenclature as Acritarch sp. 1, Acritarch sp. 2 etc. for further investigation beyond the scope of this thesis. Reworked dinoflagellate cysts were recognised by preservational characteristics, and in some cases because they do not range into the Quaternary.

4.8 DINOFLAGELLATE CYST CONCENTRATIONS

The dinoflagellate cyst concentrations were estimated by adding *Lycopodium clavatum* marker grains during palynological processing to each sample according to the method described by Stockmarr (1971). In this study, the absolute abundances of dinoflagellate cysts were estimated using the equation proposed by Benninghof (1962) shown as:

$$C = \frac{d_c \times L_t \times t}{L_c \times w}$$

Where:

C	Concentration of dinoflagellate cysts / gram of dried sediment
d _c	Number of counted dinoflagellate cysts
L _t	Number of <i>Lycopodium</i> spores / tablet
L _c	Number of counted <i>Lycopodium</i> spores
t	Number of tablets added to the sample
w	Weight of dried sediment (g)

As mentioned above, one tablet was added to each sample during processing. Batch number 1031 was used, each tablet containing 20,848 *Lycopodium* spores with a

standard deviation of 3.3%. The method of Stockmarr (1971) was used to calculate the error on the estimate of abundance. The total error (e) is the sum of e_1 (error of spores in the marker tablets or tablet calibration), e_2 (error on dinocysts counted), and e_3 (error on *Lycopodium clavatum* spores counted).

$$e = \sqrt{e_1^2 + e_2^2 + e_3^2} = 100 \cdot \sqrt{\left(\frac{\sigma_1}{r_1}\right)^2 + \left(\frac{\sigma_2}{r_2}\right)^2 + \left(\frac{\sigma_3}{r_3}\right)^2}$$

σ_1 : standard deviation on number of spores in marker tablets

σ_2 : standard deviation on dinocysts counted = $\pm \sqrt{r_2}$

σ_3 : standard deviation on *Lycopodium* spores counted = $\pm \sqrt{r_3}$

r_1 : number of spores in marker tablets

r_2 : number of dinocysts counted

r_3 : number of *Lycopodium* spores counted

4.9 MODERN DINOFLAGELLATE CYST DATASET

The modern dataset used for the North Atlantic reconstruction is an update of that published by Rochon et al. (1999) and de Vernal et al. (1997, 2001, 2005), Radi and de Vernal (2008) and Bonnet et al. (2010), and contains 1207 sites covering the North Atlantic Ocean and adjacent seas, the Arctic Ocean, and eastern North Pacific (Figure 8). The modern dataset was used for the reconstruction of surface water parameters at Site U1313 during MIS 21 and its transition to glacial stages MIS 22 and MIS 20. The North Atlantic subset contains dinoflagellate counts from 524 surface sediment samples.

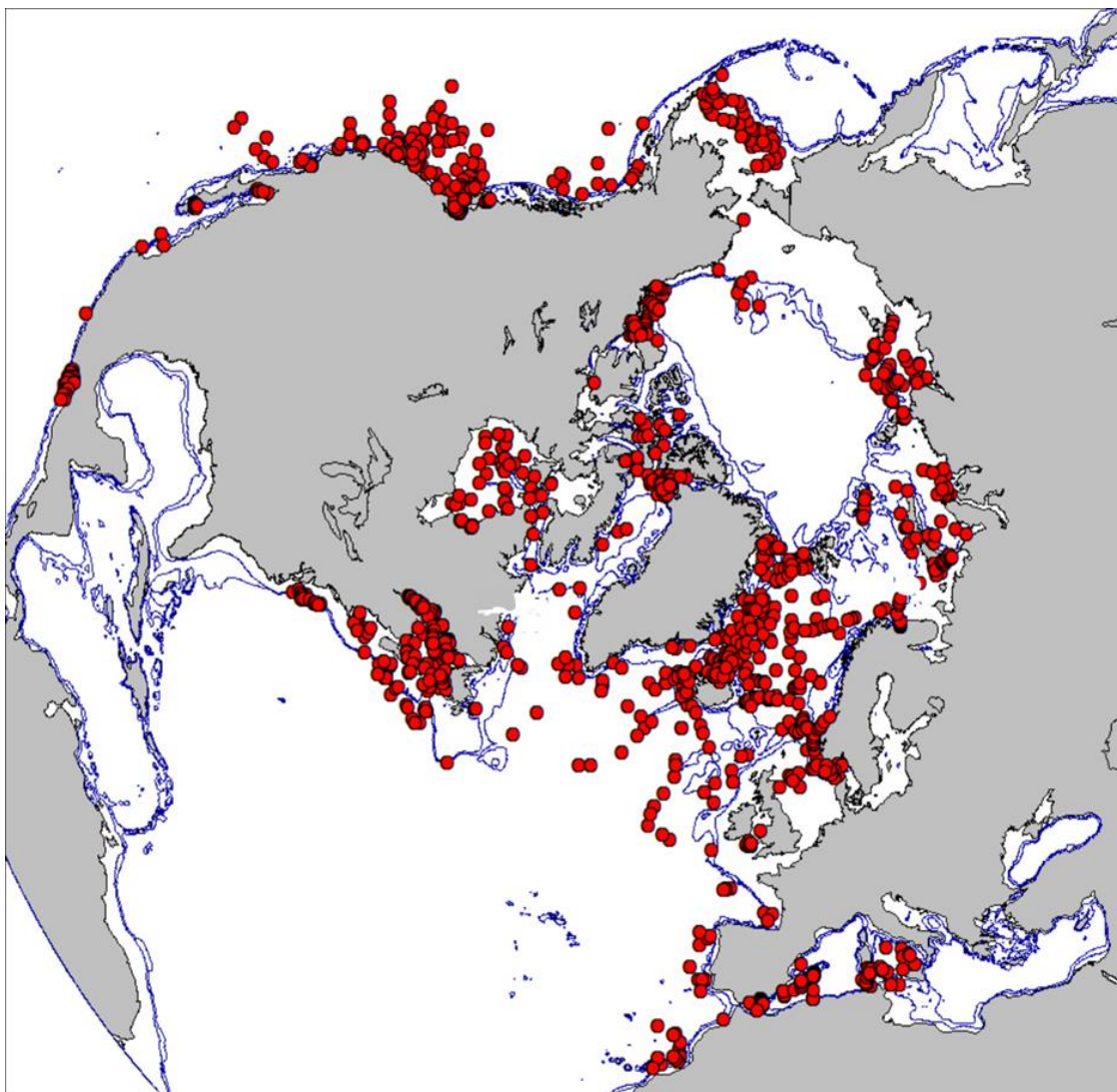


Figure 8. Location of surface sediments samples (red dots) in the n=1207 reference dataset (Radi and de Vernal, 2008; Bonnet et al., 2010) (from Bonnet et al., 2010, fig. 5a).

Each of these sample locations provides vital information on sea-surface temperature (SST), salinity (SSS), duration of sea-ice cover (I_Cover) and primary productivity (PP) parameters. These parameters are collected from various data sources: sea surface temperature and salinities are compiled from the World Ocean Atlas 2001; sea ice cover data are from the National Snow and Ice Data Centre (NSIDC) in Boulder, Colorado; and ocean primary productivity data are derived from satellite observations (moderate resolution imaging Spectro radiometer of the NASA).

4.10 MODERN ANALOGUE TECHNIQUE

The Modern Analog Technique (MAT) works on the principle that species assemblages that resemble one another are derived from similar environments (Prell, 1985). Transfer functions were initially used to compare fossil planktonic foraminiferal assemblages and modern core-top assemblages using distance measures (Imbrie and Kipp, 1971). The method employs a measure of faunal dissimilarity to compare down-core samples to each reference sample in a modern oceanographic database. MAT uses the coefficient of dissimilarity, or square chord distance, as a measure of resemblance between fossil and modern dinoflagellate cyst assemblages (Radi and de Vernal, 2008). The two main basic assumptions for MAT are that 1) recovered dinoflagellate cyst assemblages from recent surface sediments are contemporaneous with the reference hydrographic data, which are averaged over a few tens of years, and reflect the hydrographic conditions of the surface waters immediately above the sea floor from which they were recovered; and 2) microfossil assemblages result from vertical fluxes from surface waters to the sea floor, and thus are representative of local sea-surface conditions above the coring site, with limited impact of lateral transport through intermediate or deep currents (de Vernal et al., 2001). According to Zonneveld et al. (1997), the preservation of organic walled dinoflagellates cysts in the fossil sediment is dependent on several factors that include, ecological preference of the cysts, cyst production, transport and preservation. Assumptions made in MAT include an absence of lateral transport of cysts from surface waters to the ocean floor, yet long-distance travel is a documented fact (Dale, 1979). It is difficult to ascertain if the long-distance transport equally affected both the fossil and modern-day assemblage, but we know that surface and bottom water currents during glacial intervals would have been vastly different from those of today. Dinoflagellates also present another unique challenge in that different species have different responses to the damaging effects of oxidizing bottom waters which can cause bias in the preserved assemblage. For example, *Protoperidium* species are highly susceptible to damage in oxidizing

environments while *Impagidinium aculeatum* is known to be resistant under the same conditions (Zonneveld et al., 1997). This has an overall effect on the calibration set and fossil assemblage used in the transfer functions.

Quantitative reconstructions using transfer functions were performed using R software (Rx64 version 3.3.3) running on a script first developed for dinoflagellate transfer functions by Guiot and Brewer (www.cerege.fr/IMG/pdf/formationR08.pdf) obtained from GEOTOP (<http://www.geotop.uqam.ca>). Two sets of transfer functions were used: One based on the entire dataset (North Atlantic, Arctic and Pacific) denoted as n=1207, and another on the North Atlantic and Arctic denoted as n=667 in this thesis. MAT allows for the validation of data by using the “leave one out” approach that permits the calculation of the coefficient of correlation (R^2) between observed and reconstructed values, and also calculation of the Root Mean Square Error (RMSE). The leave-one-out procedure uses 1/6th of the calibration data for verification purposes of the reconstruction. Taxa abundances were expressed as per 1000 so that logarithmic transformation could be run using MAT. The use of logarithmic transformation helps to enhance the signals of species with lower abundances found in the midst of dominant taxa (Mantilla-Duran, 2013).

The dinoflagellate cyst species *Impagidinium cantabrigiense* and *Corrudinium labradorii* were omitted from the MAT analysis because they are extinct. “*Pyxidinosia striatoconulus*” and *Fibrocysta fusiforma* were also removed because of their uncertainty in the modern-day database. In addition to the above, samples with low dinoflagellate cyst counts were also excluded to avoid unnecessary bias to sample data (see Chapter 5). Finally, reworked dinoflagellate cysts were excluded because, while they have value in deciphering taphonomic processes, they do not contain relevant paleoecological information.

4.11 MULTIVARIATE ANALYSIS

PAST (Paleontological statistics software) was used to conduct multivariate analysis on the data using the **Detrended Correspondence Analysis** (DCA) method. The DCA is an ordination technique based on **Correspondence Analysis** (CA) and, like CA, it ordines both samples and species simultaneously (Toledo et al., 2009). The DCA technique emphasizes variation among individual sampling entities by defining gradients of maximum total sample variance. The DCA is widely accepted as it aims to correct the faults in CA in the following way;

- 1) Detrending with the aim to remove 'spurious' curvature in the ordination of strong single gradients.
- 2) Rescaling to correct shrinking at the ends of ordination axes resulting in packing of sites at gradient ends.
- 3) Down-weighting to reduce the influence of rare species.

According to McCune and Grace (2002), the DCA method reduces the number of ecological dimensions with minimal loss of information. Included in the dataset used to run the DCA, are relative dinoflagellate cyst abundances and two Pleistocene acritarchs denoted Acritarch sp. 1 (ACR1) and Acritarch sp. 2 (ACR2). These acritarchs were included because of their relative persistence at Site U1313 between 874 ka and 814 ka. The following dinoflagellate cysts were removed from the dataset: *Impagidinium plicatum*, *Polysphaeridium zoharyi*, *Selonopemphix quanta* and *Protoperidinium stellatum* because of their scarcity. All cysts identified under the genus *Brigantedinium* were grouped together as *Brigantedinium* spp. because of preservational difficulties. All taxa, with their abbreviations, used in the DCA analysis in the current study are listed in Table 1.

Table 1. Codes for taxa employed in the DCA analysis in the current study

Code	Taxon Name
BTEP	<i>Bitectatodinium tepikiense</i>
IACU	<i>Impagidinium aculeatum</i>
IPAL	<i>Impagidinium pallidum</i>
IPAR	<i>Impagidinium paradoxum</i>
IPAT	<i>Impagidinium patulum</i>
ISPH	<i>Impagidinium sphaericum</i>
ISTR	<i>Impagidinium striatum</i>
NLAB	<i>Nematosphaeropsis labyrinthus</i>
OCEN	<i>Operculodinium centrocarpum</i>
PRET	<i>Pyxidinopsis reticulata</i>
SELO	<i>Spiniferites elongatus</i>
SMIR	<i>Spiniferites mirabilis</i> group
SSPP	<i>Spiniferites</i> spp. indet.
BSSP	<i>Brigantedinium</i> spp. total
FFUS	<i>Fusiforma fibrocysta</i>
ICANT	<i>Impagidinium cantabrigiense</i>
ACR1	Acritarch sp. 1
ACR2	Acritarch sp. 2
USSP	<i>Spiniferites</i> sp. 1. Unique to MIS 22
PSTR	<i>"Pyxidinopsis striatoconulus"</i>

Cluster analysis was also performed on the data using R-Studio software. Cluster analysis comprises a series of multivariate methods that are used to find true groups of data or stations (Nair et al., 2013). For the U1313 data, this produced a dendrogram that was used to divide the data into biostratigraphic assemblage zones (biozones). This method uses an Unweighted pair-group average logarithm (UPGMA) and the Morisita Index. The Morisita index is ideal in this case, as this index measures the similarity between two communities, being most easily interpreted as a probability. It varies from 0 (no similarity) to 1 (complete similarity). It is nearly independent of sample size, except for very small samples (Krebs, 1999).

Canonical Correspondence Analysis (CCA) was also used on the sample data from U1313. CCA explores the relationships between two multivariate sets of variables (vectors), all measured on the same individual. CCA was developed to help ecologists relate the abundance of species to environmental variables (ter Braak, 1986). Using CCA in the realm of palynology has gained considerable traction in recent decades, with many researchers using this application (Hennissen et al., 2017). CCA analysis was performed using XLstats (2017) software, and the following six listed variables below were utilized:

1. Summer sea surface temperature (SST) derived from reconstruction data obtained using MAT.
2. Summer sea surface salinity (SSS) derived from reconstruction data obtained using MAT.
3. Primary productivity (PP) derived from reconstruction data obtained from MAT.
4. AGE (ka) based on the age model of Ferretti et al. (2010).
5. Sedimentation rates (Sed/Rate) based on Ferretti et al. (2010).
6. $\delta^{18}\text{O}$ measured on the tests of *G. bulloides* from Ferretti et al. (2010).

Taxon abbreviations used for the CCA map are the same as those used in the DCA (see Table 1).

4.12 OTHER STATISTICAL ANALYSES

4.12.1 Species richness

Species richness is the number of species in a given sample, community or area. It is a measure of diversity (biodiversity). Diversity is attributed to stability, productivity and trophic structure of the community (Colwell and Lees, 2000). It must be pointed out that species richness does not take into account the population and distribution of each species in the sample. Nonetheless, species richness is currently the most widely used measure of taxonomic diversity (Stirling and Wilsey, 2001).

4.12.2 Species evenness

Evenness is a measure of the relative abundance of the different species making up the richness of an area. The Simpson D Index is commonly used in calculating diversity. The formula below illustrates how to derive the Simpson D index:

$$D = 1 - \frac{\sum n(n-1)}{N(N-1)}$$

Where n is the number of individuals displaying one trait

N = the total number of individuals

The measure ranges from 0 to 1, the higher the value the more even the species are. Greatest evenness is achieved when all species in a sample share the same abundance.

Table 2. Samples analysed for palynology in the present study of IODP Site U1313. The following information is provided: Brock University Lab ID, IODP hole, core, type, section number, sample interval (from and to, in cm), depth (meters below sea floor), age, number of *Lycopodium* tablets added, weight of each dried filtrate processed for palynology, and duration of hot sodium metahexaphosphate (minutes) and ultrasound (seconds) treatment.

Lab ID #	Sample details								Age (ka) Ferretti et al. 2015	Total Dry Weight (g)	<i>L. clavatum</i> tablets	Sodium metahexaphosphate	Ultra sound treatment (secs)
	Hole	Core	Type	Section	Half	Top (cm)	Bot (cm)	Depth (mbsf)					
MD 100	D	4	H	5	W	48	49	34.98	810.582	9.90	1	30	30
MD 99	D	4	H	5	W	51	52	35.01	811.207	10.30	1	30	30
MD 98	D	4	H	5	W	54	55	35.04	811.832	11.40	1	30	30
MD 97	D	4	H	5	W	57	58	35.07	812.457	10.20	1	30	30
MD 96	D	4	H	5	W	60	61	35.10	813.082	13.40	1	30	30
MD 95	D	4	H	5	W	63	64	35.13	813.707	6.80	1	30	30
MD 94	D	4	H	5	W	66	67	35.16	814.332	10.80	1	30	30
MD 93	D	4	H	5	W	69	70	35.19	814.958	10.30	1	30	30
MD 92	D	4	H	5	W	72	73	35.22	815.583	11.40	1	30	30
MD 91	D	4	H	5	W	75	76	35.25	816.266	12.90	1	30	30
MD 90	D	4	H	5	W	78	79	35.28	817.066	12.60	1	30	30
MD 89	D	4	H	5	W	81	82	35.31	817.866	11.30	1	30	30
MD 88	D	4	H	5	W	84	85	35.34	818.666	12.20	1	30	30
MD 87	D	4	H	5	W	87	88	35.37	819.466	11.10	1	30	30
MD 86	D	4	H	5	W	90	91	35.40	820.266	11.80	1	30	30
MD 85	D	4	H	5	W	93	94	35.43	821.066	12.50	1	30	30
MD 84	D	4	H	5	W	96	97	35.46	821.866	13.00	1	30	30
MD 83	D	4	H	5	W	99	100	35.49	822.666	9.70	1	30	30
MD 82	D	4	H	5	W	102	103	35.52	823.466	12.30	1	30	30
MD 81	D	4	H	5	W	105	106	35.55	824.266	12.50	1	30	30
MD 80	D	4	H	5	W	108	109	35.58	825.066	12.10	1	30	30
MD 79	D	4	H	5	W	111	112	35.61	825.866	11.10	1	30	30
MD 78	D	4	H	5	W	114	115	35.64	826.666	11.90	1	30	30
MD 77	D	4	H	5	W	117	118	35.67	827.466	12.60	1	30	30
MD 76	D	4	H	5	W	120	121	35.70	828.266	11.50	1	30	30
MD 75	D	4	H	5	W	123	124	35.73	829.066	13.60	1	30	30
MD 74	D	4	H	5	W	126	127	35.76	829.866	10.30	1	30	30
MD 73	D	4	H	5	W	129	130	35.79	830.666	10.40	1	30	30
MD 72	D	4	H	5	W	132	133	35.82	831.466	13.19	1	30	30
MD 71	D	4	H	5	W	135	136	35.85	832.236	11.70	1	30	30

MD 70	D	4	H	5	W	138	139	35.88	832.937	14.31	1	30	30
MD 69	D	4	H	5	W	141	142	35.91	833.641	11.90	1	30	30
MD 68	D	4	H	5	W	144	145	35.94	834.344	12.69	1	30	30
MD 67	D	4	H	5	W	147	148	35.97	835.048	13.10	1	30	30
MD 66	D	4	H	5	W	149	150	35.99	835.517	14.30	1	30	30
MD 65	D	4	H	6	W	1	2	36.01	835.986	9.10	1	30	30
MD 64	D	4	H	6	W	3	4	36.03	836.455	11.70	1	30	30
MD 63	D	4	H	6	W	6	7	36.06	837.158	13.70	1	30	30
MD 62	D	4	H	6	W	9	10	36.09	837.861	12.70	1	30	30
MD 61/A	D	4	H	6	W	11	12	36.11	838.330	11.40	1	30	30
MD 61	D	4	H	6	W	12	13	36.12	838.560	13.80	1	30	30
MD 60	D	4	H	6	W	15	16	36.15	839.268	9.00	1	30	30
MD 59	D	4	H	6	W	18	19	36.18	839.972	13.20	1	30	30
MD 58	D	4	H	6	W	21	22	36.21	840.675	15.30	1	30	30
MD 57	D	4	H	6	W	24	25	36.24	841.400	12.60	1	30	30
MD 56	D	4	H	6	W	27	28	36.27	842.157	6.30	1	30	30
MD 55	D	4	H	6	W	30	31	36.3	842.914	14.10	1	30	30
MD 54/A	D	4	H	6	W	32	33	36.32	843.419	12.50	1	30	30
MD 54	D	4	H	6	W	33	34	36.33	843.671	13.30	1	30	30
MD 53/A	D	4	H	6	W	35	36	36.35	844.426	11.60	1	30	30
MD 53	D	4	H	6	W	36	37	36.36	844.428	13.10	1	30	30
MD 52	D	4	H	6	W	39	40	36.39	845.186	13.80	1	N/A	N/A
MD 51	D	4	H	6	W	42	43	36.42	845.943	12.90	1	30	30
MD 50	D	4	H	6	W	45	46	36.45	846.700	16.00	1	N/A	N/A
MD 49	D	4	H	6	W	48	49	36.48	847.457	12.60	1	30	30
MD 48	D	4	H	6	W	51	52	36.51	848.214	13.90	1	N/A	N/A
MD 47	D	4	H	6	W	54	55	36.54	848.971	12.80	1	30	30
MD 46	D	4	H	6	W	57	58	36.57	849.728	11.60	1	N/A	N/A
MD 45	D	4	H	6	W	59	60	36.59	850.233	10.30	1	30	30
MD 44	D	4	H	6	W	61	62	36.61	850.738	13.60	1	N/A	N/A
MD 43	D	4	H	6	W	63	64	36.63	851.242	11.40	1	30	30
MD 43/A	D	4	H	6	W	64	65	36.64	851.495	12.40	1	30	30
MD 42/A	D	4	H	6	W	65	66	36.65	851.747	14.00	1	30	30
MD 42	D	4	H	6	W	66	67	36.66	851.740	14.80	1	N/A	N/A
MD 41	D	4	H	6	W	69	70	36.69	853.220	12.30	1	30	30
MD 41/A	D	4	H	6	W	70	71	36.70	853.626	10.70	1	30	30
MD 40/A	D	4	H	6	W	71	72	36.71	854.033	14.00	1	30	30
MD 40	D	4	H	6	W	72	73	36.72	854.030	13.30	1	N/A	N/A
MD 39	D	4	H	6	W	75	76	36.75	855.464	13.40	1	30	30
MD 38/A	D	4	H	6	W	77	78	36.77	856.061	11.40	1	30	30
MD 38	D	4	H	6	W	78	79	36.78	856.359	14.00	1	N/A	N/A
MD 37	D	4	H	6	W	81	82	36.81	857.253	12.40	1	30	30
MD 36/A	D	4	H	6	W	83	84	36.83	857.849	12.30	1	30	30
MD 36	D	4	H	6	W	84	85	36.84	858.148	13.10	1	N/A	N/A
MD 35	D	4	H	6	W	87	88	36.87	859.042	9.80	1	30	30
MD 34	D	4	H	6	W	89	90	36.89	859.638	14.50	1	30	30
MD 33	D	4	H	6	W	91	92	36.91	860.235	14.40	1	30	30
MD 32	D	4	H	6	W	93	94	36.93	860.831	13.80	1	N/A	N/A
MD 31	D	4	H	6	W	95	96	36.95	861.427	10.20	1	30	30

MD 30	D	4	H	6	W	97	98	36.97	862.023	11.10	1	N/A	N/A
MD 29	D	4	H	6	W	99	100	36.99	862.620	13.70	1	30	30
MD 27	D	5	H	2	W	121	122	36.41	859.265	6.70	1	30	30
MD 26	D	5	H	2	W	123	124	36.43	859.939	12.40	1	30	30
MD 25	A	5	H	2	W	125	126	36.45	860.612	11.60	1	N/A	N/A
MD 24	A	5	H	2	W	127	128	36.47	861.285	8.60	1	30	30
MD 23	A	5	H	2	W	129	130	36.49	861.629	10.90	1	N/A	N/A
MD 22	A	5	H	2	W	131	132	36.51	862.632	8.80	1	30	30
MD 21	A	5	H	2	W	133	134	36.53	863.306	13.30	1	30	30
MD 20	A	5	H	2	W	134	135	36.54	863.642	10.60	1	30	30
MD 19	A	5	H	2	W	136	137	36.56	864.316	10.90	1	N/A	N/A
MD 16	A	5	H	2	W	142	143	36.62	866.261	11.30	1	N/A	N/A
MD 13	A	5	H	2	W	148	150	36.68	867.560	8.60	1	N/A	N/A
MD 11	A	5	H	3	W	3	4	36.73	868.877	9.90	1	N/A	N/A
MD 10/A	A	5	H	3	W	4	5	36.74	869.360	13.20	1	30	30
MD 10	A	5	H	3	W	5	6	36.75	869.362	8.90	1	N/A	N/A
MD 08	A	5	H	3	W	9	10	36.79	870.533	8.90	1	N/A	N/A
MD 07/A	A	5	H	3	W	4	5	36.80	870.766	12.60	1	30	30
MD 07	A	5	H	3	W	11	12	36.81	870.999	8.80	1	N/A	N/A
MD 06	A	5	H	3	W	14	15	36.84	871.697	7.70	1	N/A	N/A
MD 05	A	5	H	3	W	17	18	36.87	871.936	7.60	1	N/A	N/A
MD 03	A	5	H	3	W	21	22	36.91	873.327	8.60	1	N/A	N/A
MD 02	A	5	H	3	W	23	24	36.93	873.792	8.50	1	N/A	N/A

5 RESULTS

5.1 DINOFLAGELLATE CYST COUNTS AND CONCENTRATIONS

All slides analysed contained in-situ dinoflagellate cysts. A target count of 300 cysts was set for each sample (Table 3) although it was not possible to meet this target for all slides. Slides containing 200 cysts and above were deemed fit for use in statistical analyses whereas those with fewer were used for qualitative purposes.

Dinoflagellate cyst concentrations from Site U1313 (873.793 – 810.582 ka) averaged 677 cysts/gram, with the highest concentrations occurring in the bounding glacials MIS 22 and 20, averaging 1804 and 2399 cysts/gram respectively. The MIS 21–20 interglacial–glacial transition shows an increase in cyst concentrations from 826 ka possibly indicating a sudden change in conditions favourable for increased dinoflagellate productivity (Figure 9). MIS 21 concentrations average 523 cysts/gram with intermittent spikes above 500 cysts/gram in samples MD64 (836.455 ka), MD58 (840.676 ka), MD54/A (843.419 ka) and MD43/A (851.495 ka). In MIS 21, the lowest sustained cyst concentrations are observed between 862 and 854 ka.

Table 3 Dinoflagellate cyst and acritarch counts for IODP Site U1313

[illegible]

Table 3 (continued)

MD59	4H6W	36.18	840		4						26	5	18	4		20		1		8	37			1	16				13	7				8	55	2						7	2	4		160	3823	121.6		
MD58	4H6W	36.21	840.7		5			4			2	18	3	14	3		37	1			22	39		1		20				22	17				15	84	5						14	1	1		208	962	665.3	
MD57	4H6W	36.24	841.4				6	2				44	4	2	2		39				52	6				2				7	10				6	18							2				176	2435	171.2	
MD56	4H6W	36.27	842.2				5	7				38	21	39	1	1	70		2		52	26				12		1	15	4	8					3	2					5	6	3		302	3387	187.7		
MD55	4H6W	36.3	842.9		11		4	3				33	19		4		55		2		76	26		1	7	9		3	14	5					12	22	1					1	4	4		272	1301	490.4		
MD54	4H6W	36.33	843.7				2					9	2				5		1		9	7			1	3			1	2					1	8										42	1567	67.85		
MD53	4H6W	36.36	844.4				3					18	8	2	1		5				17	5									5				6	1						2				64	1432	103.4		
MD51	4H6W	36.42	845.9			1	13				1	66	9	3	8	1	10		2		56	14			2	9		1	2	1	3			37	2	3					5	12	1		202	4711	106.7			
MD49	4H6W	36.48	847.5		6		14	1				25	6	5	2		9	1	3		31	9		1	1	3					4			21	2	2					13	1	3		121	2559	117.3			
MD47	4H6W	36.54	849		6		15	3				44	18	5	9		5	3			47	13		2	1	6		3	1						1					14	3			181	1403	269				
MD45	4H6W	36.59	850.2			1	12					68	11	2	8		5	3	1		74	10		2	2	14					1			25		3				9	22	4	1	217	1360	371				
MD43	4H6W	36.63	851.2				6	5				12	5		2		2	2			15	1				7			1		1			1							2				59	1243	100.6			
MD43/A	4H6W	36.64	851.5	1	6	1	7				2	83	16	10	6		21		6		92	21		1	1	18				3	6									5				301	855	733.9				
MD42/A	4H6W	36.65	851.7								2	27	3		4		3	3			25	7		1	1	19				2	2			6	1			2					6				109	2664	90	
MD41	4H6W	36.69	853.2				15	2				65	11	2	5		3		1		67	11		2	1	22								1							7				207	3014	143.9			
MD41/A	4H6W	36.7	853.6				8	1				90	7		1	4	4				38	4		1	1	26				2	2		10			1		7				10	7	1		199	2987	139.6		
MD40/A	4H6W	36.71	854				4	2				108	5		1		1		1		50	6			1	25				2	3		11		1						1			3				220	2631	175.9
MD39	4H6W	36.75	855.5								2	129	8	1	10				1		18	2				27				1				1								4	3			199	2930	142.3		
MD37	4H6W	36.81	857.3		13						5	105	11	2	14		5		1		45	7				19			3						1		3					4	5	3		230	3835	125.6		
MD36/A	4H6W	36.83	857.8				13		1		4	107	3		25		4	2	3		96	13				18				2			12		1			1					1	2			303	2500	255.2	
MD36	4H6W	36.84	858.1		4							8		1	1						3				1			1							4									19	505	94.95				
MD35	4H6W	36.87	859				7	3			5	80	7	1	19				1		40	6		1		34			1		1					1	3					9	4	1	1	206	3049	141.5		
MD34	4H6W	36.89	859.6								1	5	1					1			10	1			1	3					3					3							5				26	970	62.33	
MD33	4H6W	36.91	860.2		9			1			6	75	6	2	27		2	1	5		53	7		1		36					3											5	14	3	2	234	2849	171.2		
MD31	4H6W	36.95	861.4				1	1			4	36	5		6		4	2			15					13					2					3							4		1		89	1265	151.6	
MD30	4H6W	36.97	862									4			1						4	1				1										13								11	400	125.1				
MD29	4H6W	36.99	862.6		9			1			5	64	7	1	9		1	1			78	4			3	28					3	5				77	4	1					2	3	9		219	1220	512.7	
MD27	5H2W	36.41	859.3			9						15	2		1		2	1			12	4		1		5									3							4				52	2348	48.83		
MD26	5H2W	36.43	859.9		2	3	28	1			5	64	3	1	14		2	1	1		55	7		2		21			2	1					25		2					9	7			213	3072	161.5		
MD24	5H2W	36.47	861.3				5	1				26	1	1	8		4		1		23	2		5		2			1						2								2				80	1243	134.2	
MD23/A	5H2W	36.48	861.6				17					63	10	2	7		1	5	1		56	8			1	9		1		3	6					16							4				190	3056	140.5	
MD22	5H2W	36.51	862.6		25			4			11	61	9	5	7	1	4	2	2		79	15			1	23		2	2	4	6				2		4					9	1	6	1	263	2721	206.9		
MD20	5H2W	36.54	863.6		8		16				7	57	4		23		2	4	1		38	6			3	27			2		2				15					1		3	1	4	3	200	1942	231.9		
MD19	5H2W	36.56	864.3				11				5	60	4	2	34		2	3			56	8		3		24				1	5	1	12								1	4			231	2330	207.6			
MD16	5H2W	36.62	866.3				3	1				11	3		7		1				10	5		1		7					1		1									2				51	1732	61.39		
MD11/A	5H3W	36.72	868.9				12					31	4		7		1				12	2		2	1	3				1														8				76	2122	74.67
MD10/A	5H3W	36.74	869.4				16					19	3		26						21	2		1		15					2	6											7				111	1378	167.9	
MD08	5H3W	36.79	870.5		12		12					106	3	11	45		1		2		77	13			2	13					2						1					8	17	8	2	299	1176	531.8		
MD07/A	5H3W	36.8	870.8				11	1				43	6		32			2	4		24	5			2	26				2	2	11					1						3				171	670	535.2	
MD07	5H3W	36.81	871				28		1			70	6	6	23	1	3	2	3		52	7		1	1	19					3	9											17				235	750	653.2	
MD06	5H3W	36.84	871.7				10	6				79	22	63	14	2	4		5		69	4			1	17		1	1						1							7	28	13		300	764	821.4		
MD05/A	5H3W	36.85	871.9				11	6				53	37	33	24	2	1		3	1	60	8			1	44			2			2	10						1	1				12				298	356	1757
MD03	5H3W	36.91	873.3				4	16		2		37	68	24	17				1	5	21	8			9	14		15		2	18	26		2		11						51				287	340	1840		
MD02	5H3W	36.93	873.8					9		2		30	74	37	18	2	1		2		24	22			2	8		10		3	20	38		3		11						36				302	567	1162		

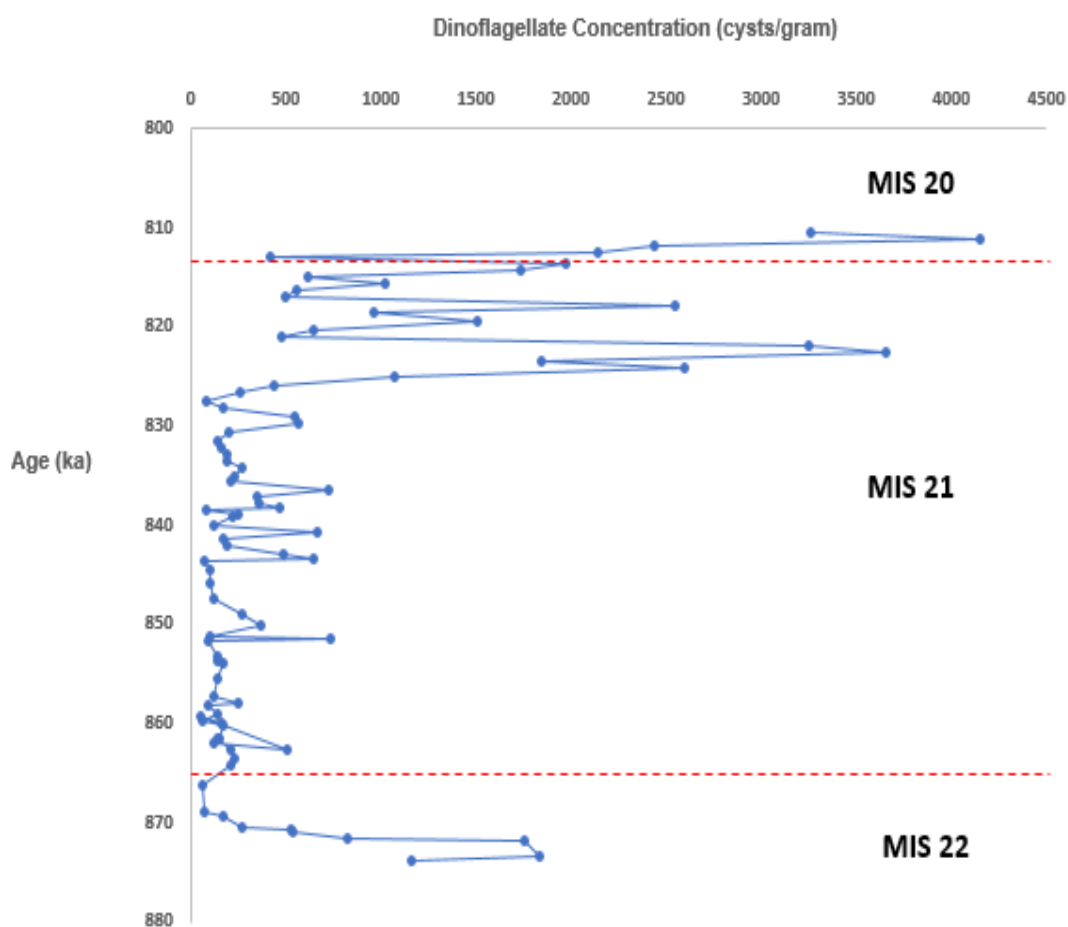


Figure 9 In-situ dinoflagellate cyst concentrations per gram dry weight of sediment. The dashed red lines show the boundaries between marine isotope stages following Lisiecki (2004: http://www.lorraine-lisiecki.com/LR04_MISboundaries.txt).

5.2 DINOFLAGELLATE CYST ASSEMBLAGES AT IODP SITE U1313

On average, 230 specimens were counted per sample. A total of 111 samples were processed and analysed, 18 genera and 22 species of in-situ dinoflagellate cysts were identified. The count data are shown in Table 3. Assemblages are dominated by *Nematosphaeropsis labyrinthus* and *Impagidinium aculeatum* (Figure 10a, f). Other common taxa occurring throughout the succession are *Operculodinium centrocarpum* sensu Wall and Dale (1966), *Impagidinium pallidum*, *I. paradoxum*, and *I. patulum*, and *Brigantedinium* spp. total. The latter collectively represent *Brigantedinium cariacense*, *Brigantedinium simplex*, and specimens that could not be identified routinely to species

level owing to crumpling or poor orientation. *Spiniferites elongatus*, *Bitectatodinium tepikiense* and “*Pyxidinopsis striatoconulus*” are consistently present but in small proportions.

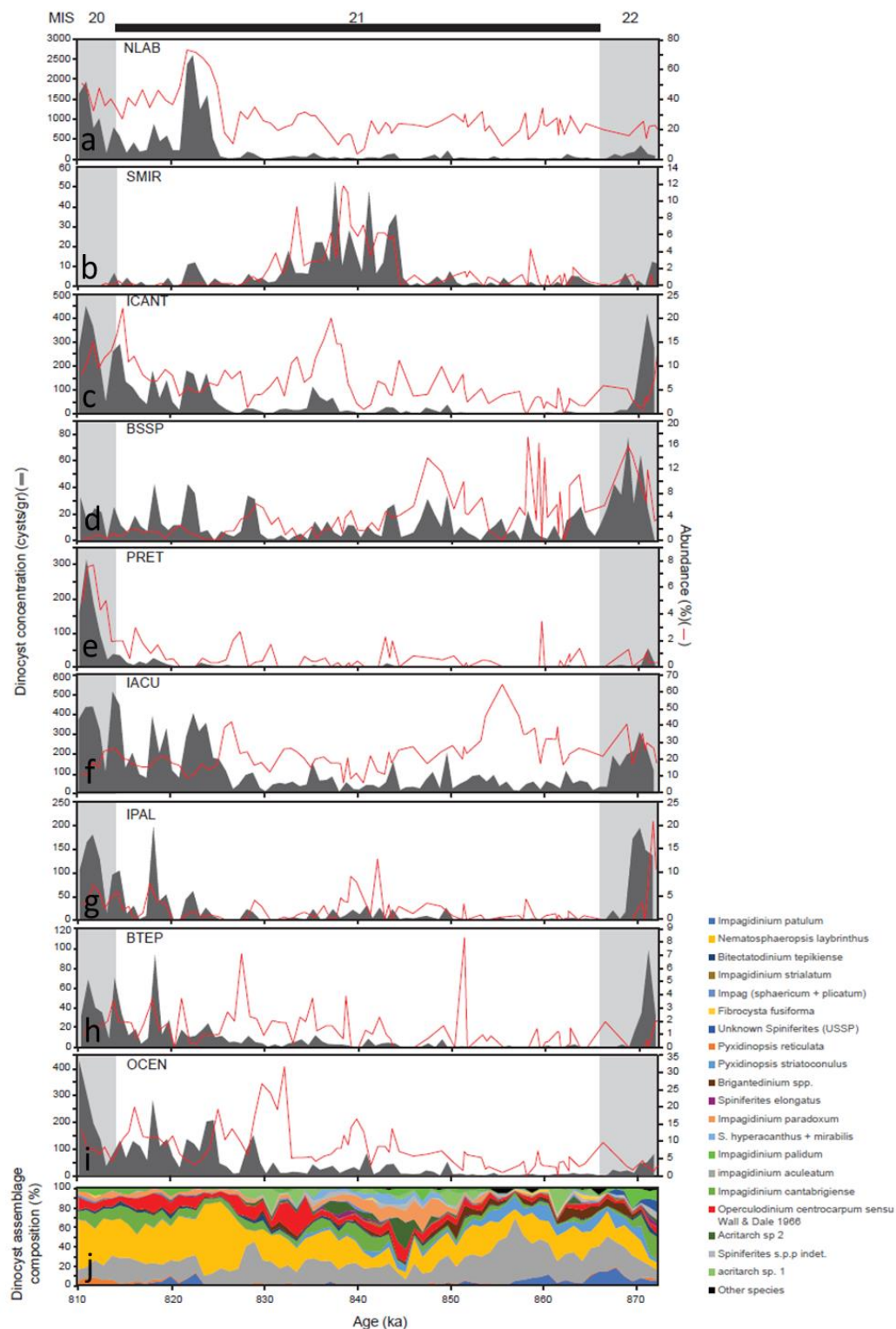


Figure 10. Abundance/concentration signatures of selected dinoflagellate cysts (a–j) and synoptic diagram of dinoflagellate cyst assemblage compositions (j) for IODP Site U1313. Species abbreviations as in Table 1. Codes for taxa employed in the DCA analysis in the current study. The grey columns indicate even-numbered ('cold') marine isotope stages.

5.3 COOL WATER SPECIES

Three cool-water related species, *Spiniferites elongatus*, *Impagidinium pallidum* and *Bitectatodinium tepikiense*, were identified at Site U1313.

Spiniferites elongatus is a Northern Hemisphere species with a polar to sub-tropical distribution (Figure 11). It occurs in fully marine settings, with highest abundances in eutrophic settings such as the North Atlantic frontal system (Zonneveld et al., 2013). According to Rochon et al. (1999), *Spiniferites elongatus* is typically used as a cold-water indicator and has been grouped with the similar morphotypes *Spiniferites frigidus* and *Rottnestia amphiacavata*. At Site U1313, the relative abundances of *S. elongatus* are low, varying from 0 to 5.4% of the total counts, with the highest peak in MIS 21 (835.517 ka). There is a continuous sustained presence of *S. elongatus* between 831.467 and 838.565 ka in MIS 21 with abundances fluctuating between 0.47% and 5.4%.

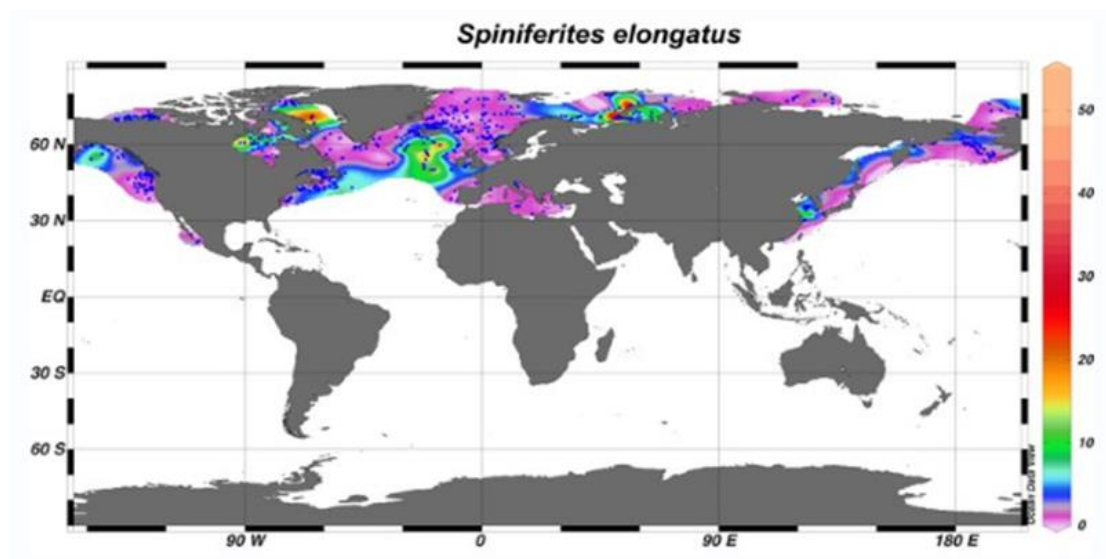


Figure 11. Present geographic distribution of *Spiniferites elongatus* (from Zonneveld et al., 2013, fig. 232).

Based on its modern distribution (Figure 12), *Impagidinium pallidum* can be considered a polar species, and is typically found in regions that have high nitrate and phosphate

concentrations associated with low chlorophyll a concentrations in the upper waters (Zonneveld et al., 2013). *I. pallidum* can also be present in high abundances in places that are seasonally covered by sea ice and in areas of very low salinities. In borehole U1313, *I. pallidum* is consistently found in the present study where its abundance varies from 0 to 21%. Its highest abundance of 21% is found in the glacial MIS 22 (871.698 ka) in sample MD06, and in MIS 21 the highest relative abundance occurs in sample MD56 (842.158 ka). In the bounding glacial MIS 20, *I. pallidum* varies from 3.27 to 7.30%. However, it should be noted that the status of this species as an exclusively cold-water indicator has been questioned by De Schepper et al. (2011) who recorded abundances in the Plio–Pleistocene of the North Atlantic exceeding 10% where reconstructed SSTs were around 12–14°C.

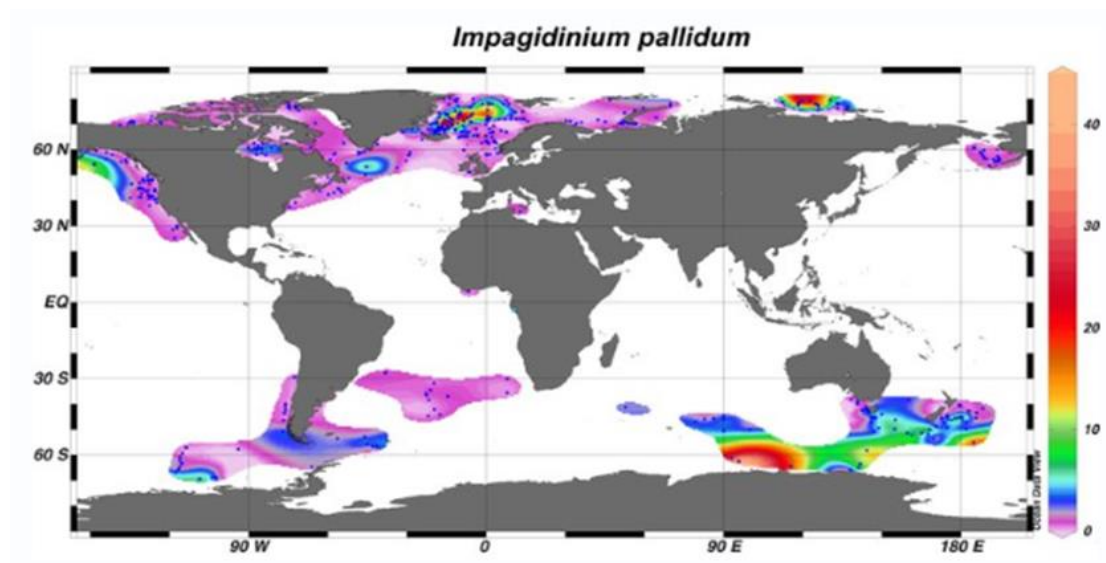


Figure 12. Present geographic distribution of *Impagidinium pallidum* (Zonneveld et al., 2013, fig. 84).

Another cold-water indicator species found at Site U1313 is *Bitectatodinium tepikiense*. This species has been described as a cool water neritic species (De Schepper et al., 2009) and has a restricted bipolar distribution. It is found today in sub-polar and temperate regions between the subtropical and arctic frontal systems on both hemispheres (Figure. 13). It occurs in both eutrophic and oligotrophic environments

(Zonneveld et al., 2013). According to Gunderson (1988), *B. tepikiense* is associated with reduced salinities, as occurs with melting ice (Bakken and Dale, 1986). At Site U1313, *B. tepikiense* is found fairly consistently throughout the studied interval, with a relative abundance varying from 0 to 8.33%. The highest recorded abundance is found in MIS 21 in sample MD43 (851.243 ka).

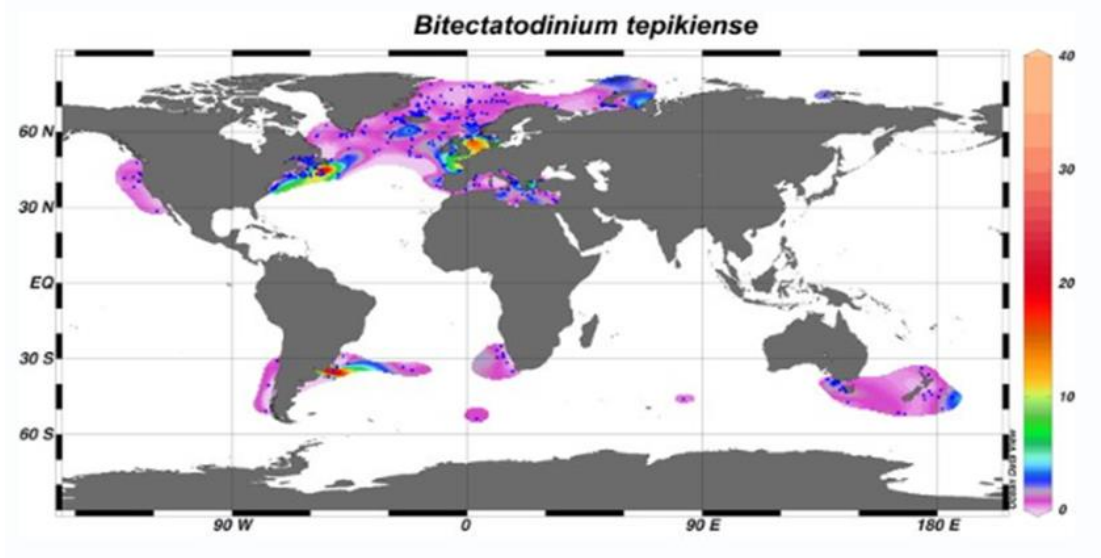


Figure. 13. Present geographic distribution of *Bitectatodinium tepikiense* (Zonneveld et al., 2013, fig. 16).

The relative abundances of *B. tepikiense*, *S. elongatus* and *I. pallidum* are plotted against the planktonic isotopic data ($\delta^{18}\text{O}$) on Figure 14. *I. pallidum* has the highest relative abundances amongst these three species. The cosmopolitan species *Operculodinium centrocarpum* sensu Wall & Dale 1966 has been added to the plot because its distribution during the Quaternary is related to the nutrient-enhanced North Atlantic Current (NAC) which influences Site U1313 during southward shifts associated with Northern Hemisphere ice sheet growth.

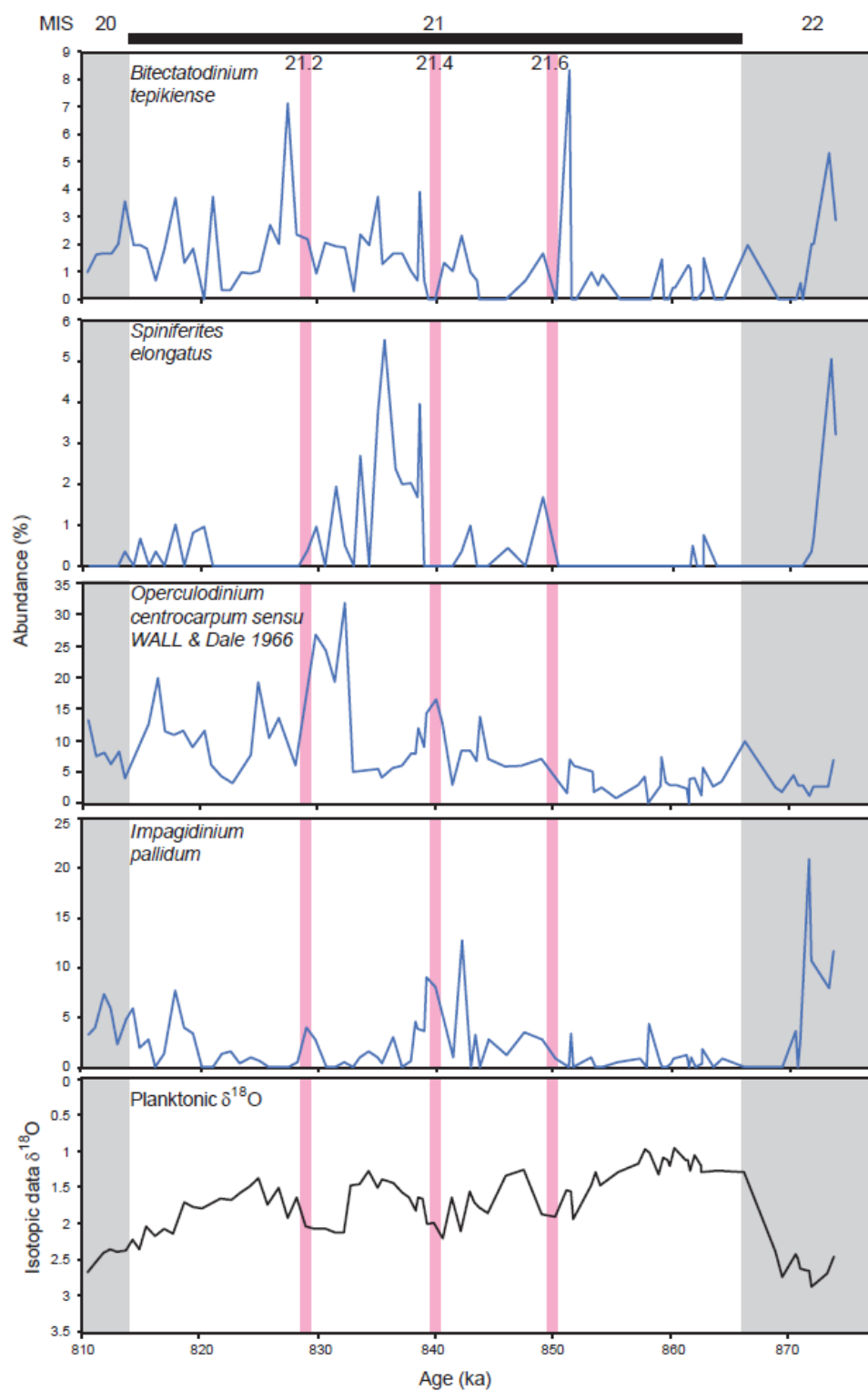


Figure 14. Relative abundances of cool-related dinoflagellate cyst species *B. tepikiense*, *S. elongatus*, and *I. pallidum*, and the North Atlantic Current indicator *O. centrocarpum sensu* Wall and Dale (1966) plotted against planktonic foraminifera *G. bulloides* isotopic data ($\delta^{18}\text{O}$) obtained from the same samples. Isotopic units (‰VPDB)

5.4 AUTOTROPHIC DINOFLAGELLATE CYSTS

Spiniferites spp. indet., *Spiniferites hyperacanthus–mirabilis*, and *Operculodinium centrocarpum* sensu Wall & Dale (1966) comprise most of the autotrophic dinoflagellate cysts found in the present study. *Spiniferites mirabilis* and *Spiniferites hyperacanthus* were combined as the *Spiniferites mirabilis* group because of their comparable morphology (de Vernal et al., 1992) and the difficulty in distinguishing one from the other when unfavourably oriented (Rochon et al., 1999). According to Zonneveld et al. (2013), the modern geographic distribution of *Spiniferites mirabilis* is bounded north and south by the subtropical fronts and has a temperate and equatorial distribution. Its relative abundance at Site U1313 varies from 0 to 11.76%, with the highest recorded abundance in sample MD 61 (838.565 ka). The relative abundance of *Spiniferites* spp. indet. varies from 0 to 10.34%. The highest recorded abundance is in MIS 21 in sample MD 34 (859.639 ka). *Lingulodinium machaerophorum* has a notable absence in MIS 21 and bounding MIS 20. It is recorded in just two samples in MIS 22, MD 05/A and MD 03 with abundances of 0.33 and 1.66%, respectively.

Operculodinium centrocarpum sensu Wall & Dale (1966) is the dominant autotrophic species. Its relative abundance varies from 0 to 31.75% with the highest recording in sample MD71 (832.234 ka) (Figure 14). *O. centrocarpum* is found consistently throughout the studied interval and has been used in the North Atlantic as an indicator of the NAC which is associated with elevated nutrient levels. De Schepper et al. (2009, 2013) and Hennissen et al. (2014, 2015) have used variations in the abundance of *O. centrocarpum* to track shifts in the position and strength of the NAC during the Pliocene and Pleistocene, respectively. *O. centrocarpum* is described as a cosmopolitan species present in all types of environments and tolerant of a wide range of temperature and salinity conditions (Rochon et al., 1999).

5.5 HETEROTROPHIC DINOFLAGELLATE CYSTS

Brigantedinium cariacense, *Brigantedinium simplex* and *Selenopemphix quanta* comprise most of the heterotrophic dinoflagellate cysts found in the present study. Most *Brigantedinium* specimens were identified as *Brigantedinium* spp. indet. because most could not be identified to species level because of crumpling or poor orientation. The heterotrophic dinoflagellate cysts are dominated by *Brigantedinium* spp. which are consistently found throughout the study interval (Figure 15). *Brigantedinium* spp. have a relative abundance that fluctuates between 0 and 17.39%, the highest is recorded in sample MD 36 (858.148 ka) in MIS 21.

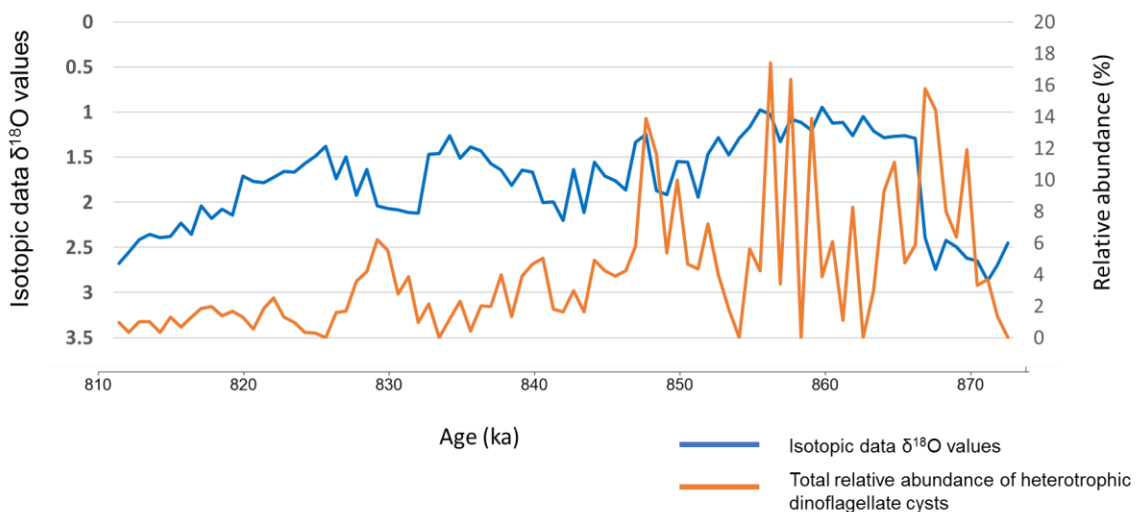


Figure 15. Relative abundance of total heterotrophic dinoflagellate cyst species in Site U1313 vs planktonic foraminifera *G. bulloides* isotope data ($\delta^{18}\text{O}$) obtained from the same samples. Isotopic units (‰VPDB)

Figure 15 shows a corresponding increase in relative abundances of heterotrophic dinoflagellates cysts with increasing $\delta^{18}\text{O}$ notably around 830, 848 and 870 ka. According to Rochon et al. (1999), the genus *Brigantedinium* is widely associated with high nutrient levels, and several authors (Zonneveld et al., 2010; Pospelova et al., 2010; Rochon et al., 1999) have linked this genus to upwelling zones.

5.6 EXTINCT DINOFLAGELLATE CYST SPECIES

5.6.1 *Impagidinium cantabrigiense*

This is one of only two apparently extinct species encountered in the present study. This species has a known range of Late Pliocene through Middle Pleistocene (De Schepper and Head, 2008). It is found consistently and persistently throughout the studied interval, its relative abundance varying from 0 to 23.42%. Its highest occurrence is in sample MD 02 (873.793 ka) in MIS 22. According to De Schepper and Head (2008), *I. cantabrigiense* seems to have preferred cooler conditions and is found in transitional phases from warm to cold surface waters in open marine paleoenvironments.

5.6.2 *Fibrocysta? fusiforma* Edwards, 1984

This species was first described from the eastern North Atlantic where it was documented from the upper Middle Miocene through Upper Miocene (Edwards, 1984). It was subsequently reported from the Piacenzian–Gelasian of southern Italy with a range of 2.70–2.32 Ma (Versteegh, 1994), and from the Piacenzian–Gelasian of central North Atlantic DSDP Holes 607/607A where it has a similar reported range of 2.79–2.31 Ma (Versteegh, 1997). In the studied interval, *F.? fusiforma* occurs consistently between samples MD 19 (864.316 ka) and MD 37 (857.254 ka). The relative abundance in this range varies between 0 and 4.35%. Specimens from the present study have a fusiform shape with an elongate rounded protrusion at the apex. The observed specimens conform with the description given by Edwards (1984). Figure 16 shows images of *F.? fusiforma* identified in this studied interval at Site U1313.

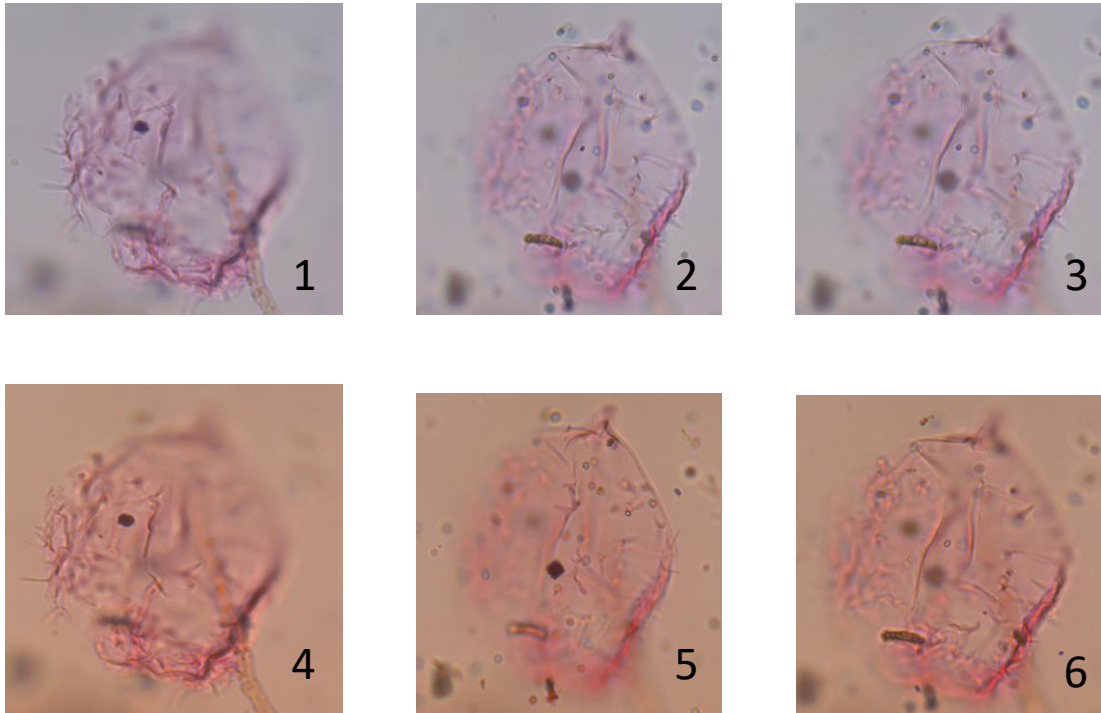


Figure 16 showing semi-crumpled specimens of *F.? fusiforma* taken from slide MD 02; diameter of central body 40 µm; England finder reference P35/1; under bright field illumination at different focal levels; process lengths 5–10µm.

5.7 ACRITARCHS

Two in-situ acritarchs, *Acritarch* sp. 1 and *Acritarch* sp. 2, were identified (Figure 17). *Acritarch* 1 has a lowest occurrence in MIS 22 in sample MD 06 (871.698 ka) and is absent from MIS 20. This acritarch is small, has a spherical central body with a smooth surface covered with hollow cone-shaped processes of similar size and even distribution. It has no discernible pylome, and is presumably a simple split. Its relative abundance fluctuates from 0 to 25%, with the highest abundance recorded in sample MD 76 (828.267 ka) in MIS 21.

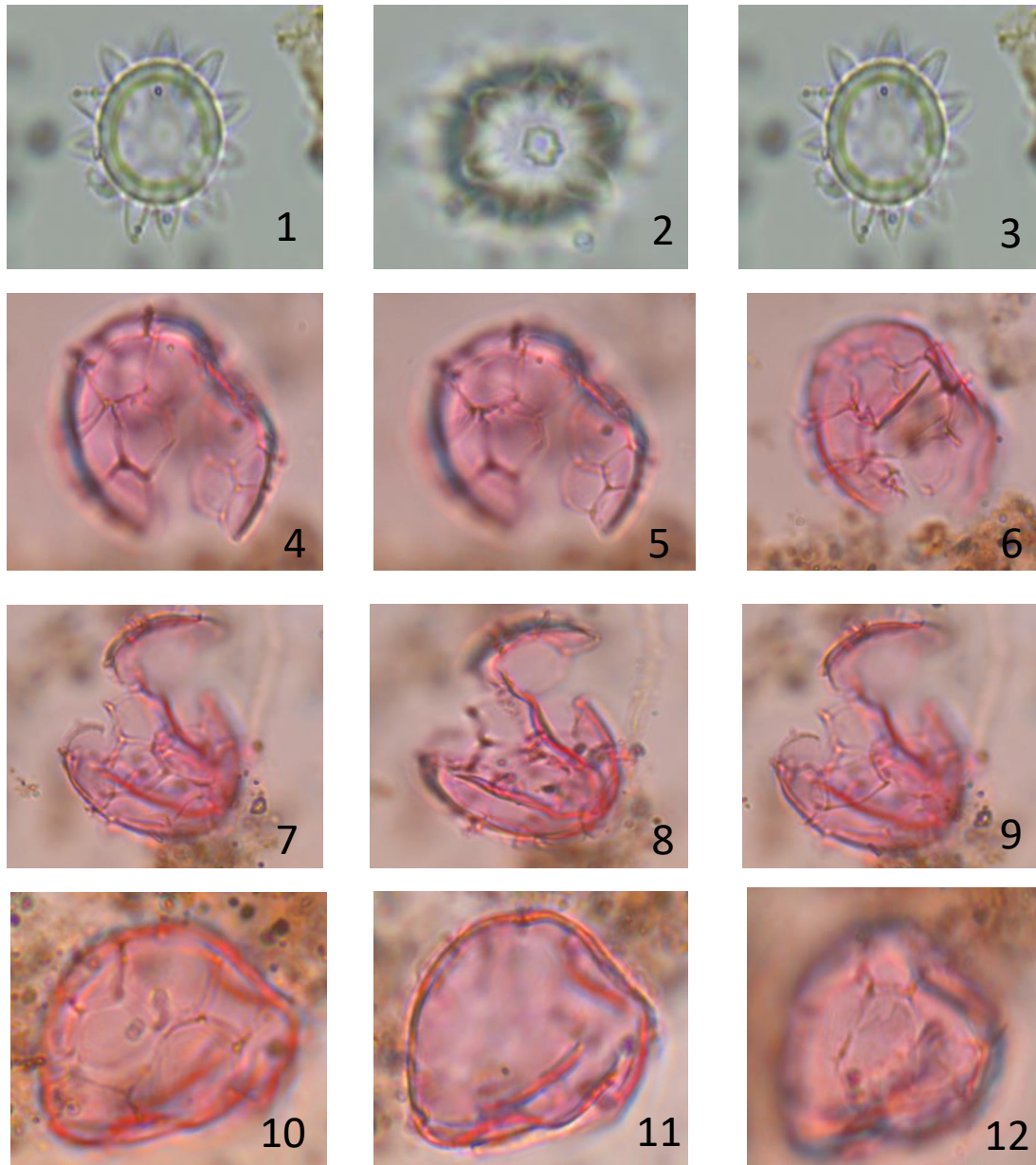


Figure 17. Acritarchs from Site U1313. Acritarch sp. 1 (1–3) showing hollow conical processes. Diameter of central body: 15 μ m. Process length: 3 μ m. Sample MD78; England Finder reference O15/0. Acritarch sp. 2 (4–12) showing low crests dividing the surface into polygonal fields. Note angular split along field contacts. Diameter of cyst: 25 μ m. Sample MD02; England Finder reference: N26/02.

Acritarch sp. 2 is a small cyst, has low crests dividing the smooth central body surface into polygonal fields, and an aperture formed by an angular split between the polygonal fields. Acritarch sp. 2 has its lowest occurrence in MD 02 (873.793 ka) and occurs sporadically throughout the studied interval. This acritarch is notably absent from MIS

20, but occurs continuously between MD 49 (847.457 ka) and MD 79 (825.867 ka). Its highest relative abundance is 27% found in sample MD 58 (840.676 ka).

5.8 REWORKED PALYNOMORPHS

The following reworked palynomorphs were found: the dinoflagellate cysts *Oligosphaeridium complex* and *Spinidinium* spp., and the acritarchs *Veryhachium* spp. as well as numerous other unidentified taxa. Most were found between sample MD 42/A (851.748 ka) and MD 36/A (857.850 ka). The relative abundances are very low as taxa were usually represented by single specimens. Reworked palynomorphs are nonetheless of crucial importance at Site U1313 as they can play a pivotal role in assessing the age and provenance of Ice Rafted Debris (IRD) (Mantilla, 2013), this site lying within the southern boundary of the IRD belt (Figure 18).

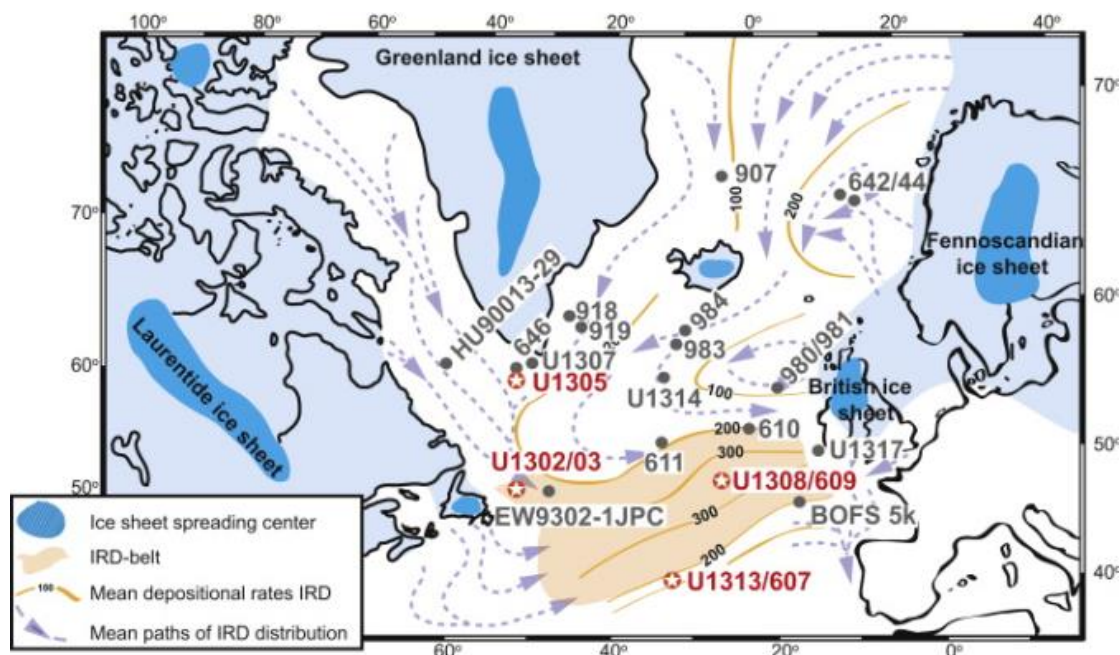


Figure 18. IODP Site U1313 with respect to the IRD belt in the North Atlantic (from Naafs et al., 2011, fig. 1).

5.9 MODERN ANALOGUE TECHNIQUE

A quantitative estimation of past sea surface parameters for the studied interval of U1313 was performed using the modern analogue technique (MAT). As stated in Section 4.10, this method calculates the algebraic distance (coefficient of dissimilarity or squared chord distance) between fossil and modern assemblages (Radi and de Vernal, 2008).

i. Cross validation tests (n=1207 and n= 667)

Results of cross validation tests conducted for the sea surface temperatures (SST) and sea surface salinity (SSS) parameters. For n=1207, the coefficient of correlation between the observed and estimated values is greater than 0.90% for the SST and between 0.68 and 0.74% for the SSS (Figure 19, Figure 20). The coefficient of correlation for the SSS falls outside of the reliability range, implying that any interpretation using this parameter must be made with due care. Results for n=667, the coefficient of correlation between the observed and estimated values for sea surface temperatures for August (SST_A) is greater than 0.90% while that for sea surface temperature for February (SST_F) is less than 0.90%. The coefficient of correlation for SSS for both August and February falls outside the reliability range (Figure 21) and as with the n=1207 dataset, interpretation using this parameter must be made with due care.

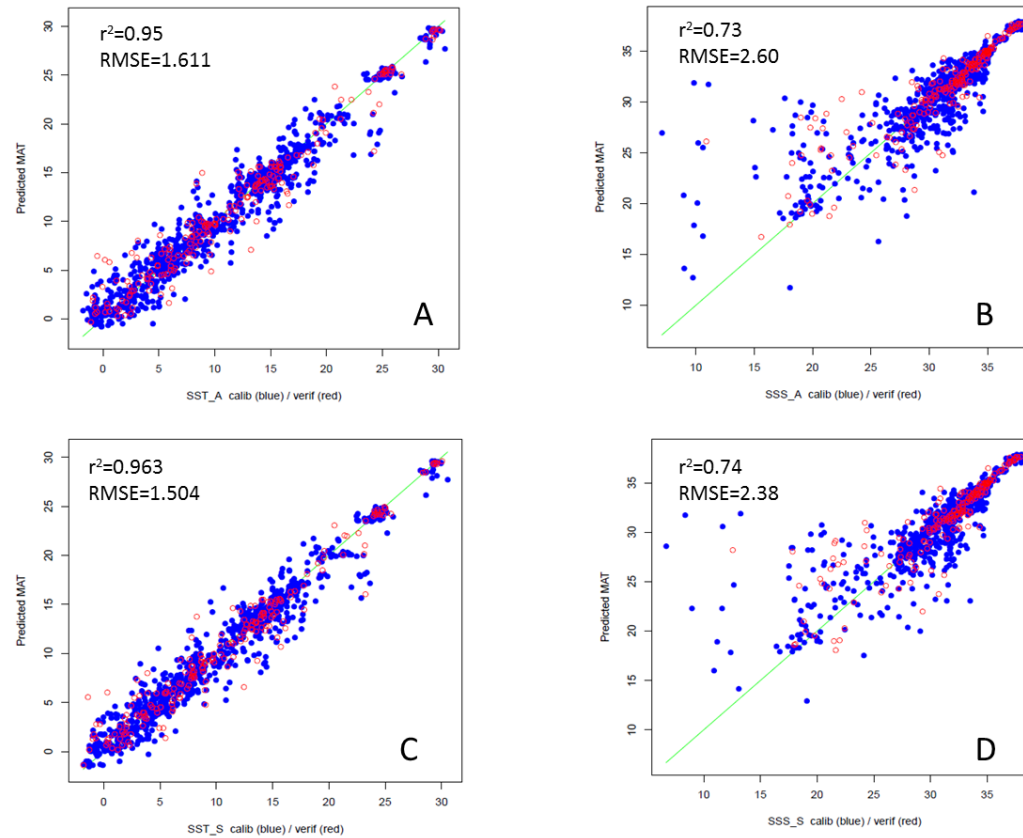


Figure 19. Results of cross-validation tests using the leave-one-out technique for the combined North Atlantic, Arctic and Pacific (n=1207) dataset, showing their coefficients of correlation and root mean square errors (RMSEs). A = August sea-surface temperature (SST_A), B = August sea-surface salinity (SSS_A), C =summer sea-surface temperature SST_S, and D =summer sea-surface salinity (SSS_S). Calibration (modern) datasets (blue dots) and validation (U1313) dataset (red circles).

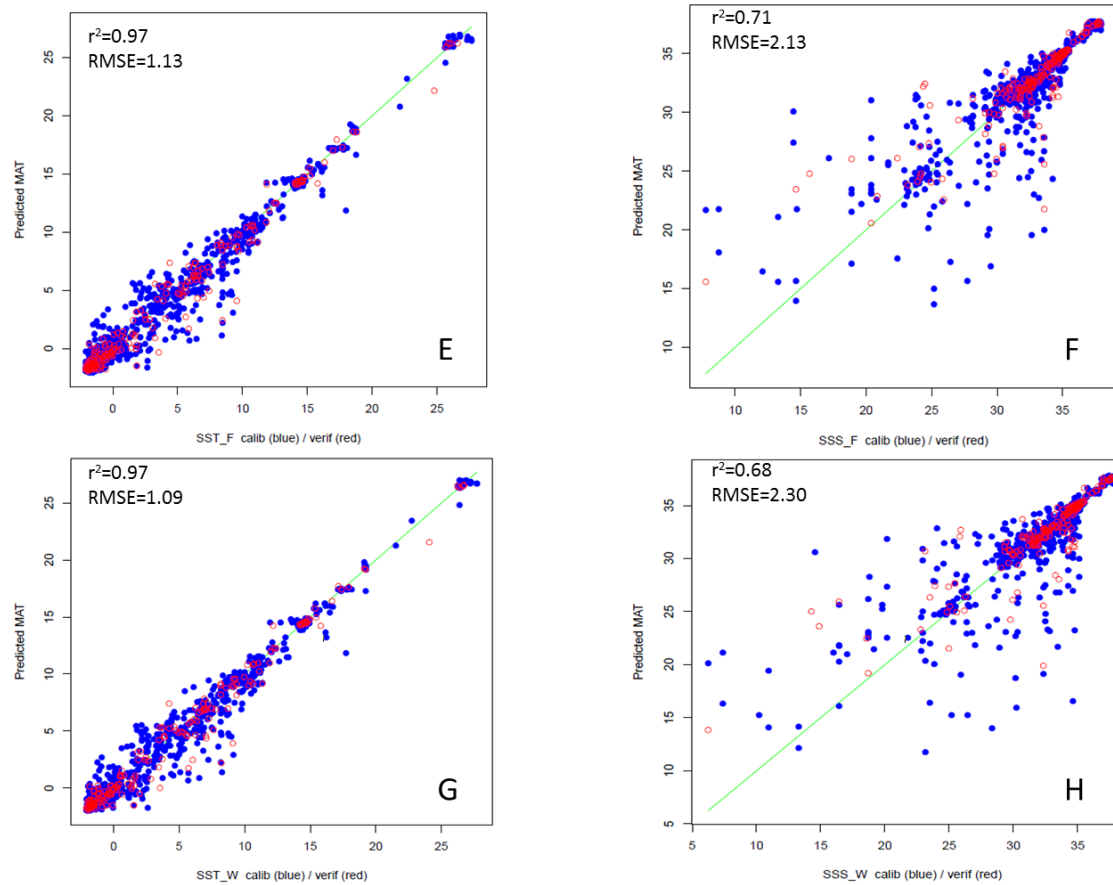


Figure 20. Results of cross-validation tests using the leave-one-out technique for the combined North Atlantic, Arctic and Pacific (n=1207) dataset, showing their coefficients of correlation and root mean square errors (RMSEs). E = February sea-surface temperatures (SST_F), F = February sea-surface salinity (SSS_F), G = Winter sea-surface temperature (SST_W), and H = Winter sea-surface salinity (SSS_W). Calibration (modern) datasets (blue dots) and validation (U1313) dataset (red circles).

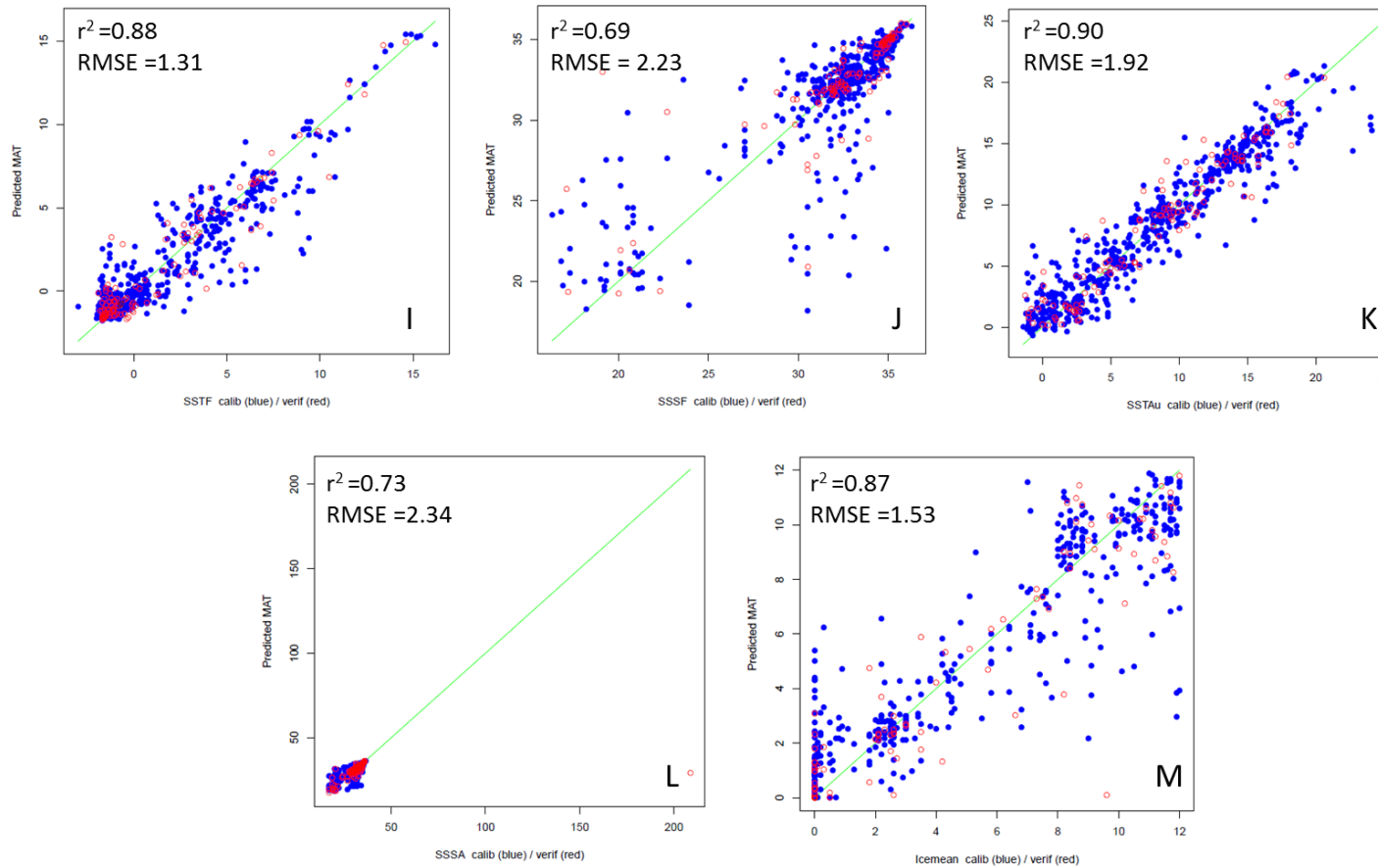


Figure 21. Results of cross-validation tests using the leave-one-out technique for the combined North Atlantic and Arctic (n=667) dataset, showing their coefficients of correlation and root mean square errors (RMSEs). I = February sea-surface temperature (SSTF), J = February sea-surface salinity (SSSF), K = August sea-surface temperature (SSTAu), L = August sea-surface salinity (SSSA), and M = sea ice cover (months/year). Calibration (modern) datasets (blue dots) and validation (U1313) dataset (red circles).

ii. Reconstruction based on the entire data set (N. Atlantic, Arctic and Pacific)

MAT reconstruction for sea surface temperatures (SST) and sea surface salinity (SSS) using the n=1207 dataset are summarized in Table 4. Of interest is the intermittent increases (spikes) in SSS between 830 and 850 ka (Figure 22) that correspond with an increase in cold water dinoflagellate cysts. MAT reconstructions of sea surface temperature in MIS 21 show fluctuations, with dips corresponding to glacial suborbital-scale climate events already recorded for U1313 (Figure 22).

Table 4. Reconstruction measurements for sea surface temperature (SST, in °C) and sea surface salinity (SSS, in PSU) for Site U1313 using the n=1207 modern calibration dataset.

Parameter	Reconstruction Measurement (Max)	Reconstruction Measurement (Min)
SST_Summer (°C)	20.76	13.45
SST_Winter (°C)	12.82	7.70
SSS_Summer (PSU)	36.03	32.59
SSS_Winter (PSU)	36.02	32.32

MAT reconstructions for primary productivity ($\text{gCm}^{-2}\text{yr}^{-1}$) were also performed. Primary productivity is the synthesis of organic matter from inorganic material mainly through the process of photosynthesis and to some extent through chemosynthesis. This process requires light, nutrients and other elements. Primary productivity can also be hampered by heterotrophs. A plot of planktonic foraminiferal $\delta^{18}\text{O}$ data against reconstructed primary productivity (Figure 22) shows that an decrease in $\delta^{18}\text{O}$ is met with a corresponding increase in primary productivity, with two major intermittent increases between 830 and 840 ka with a peak in primary productivity at 866.261 ka.

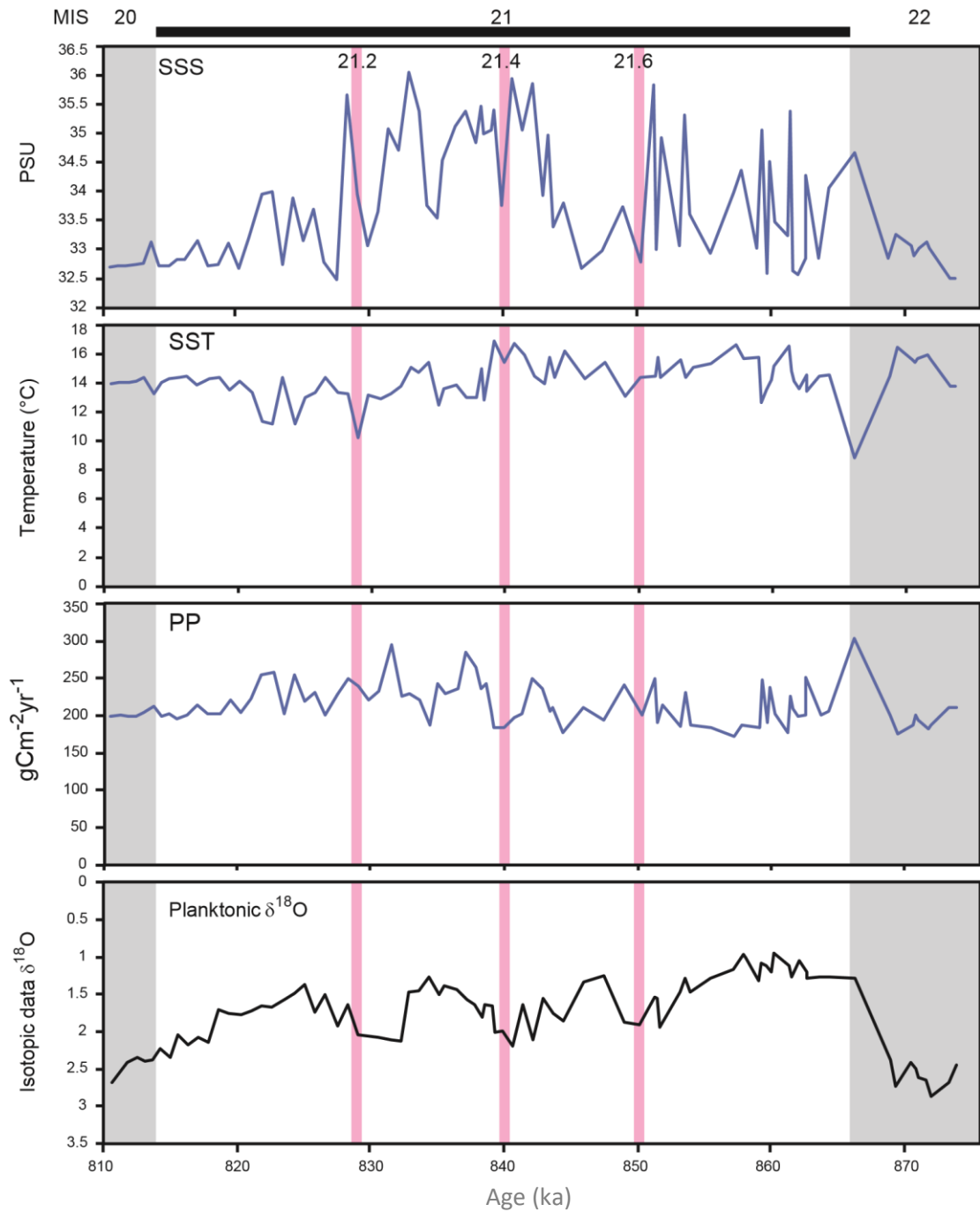


Figure 22. Plot of planktonic foraminiferal (*G. bulloides*) $\delta^{18}\text{O}$ data against reconstructed primary productivity, sea surface temperature and sea surface salinity using MAT n=1207. Isotopic units (‰VPDB)

5.9.3 Reconstruction using the N. Atlantic and Arctic dataset

MAT reconstructions for SST and SSS using the North Atlantic and Arctic combined (n=667) dataset are summarized in Table 5. The climate reconstructions are for sea surface temperature and salinity for the months of February and August, and no ice

cover and primary productivity parameters are calculated using this dataset as for n=1207.

Table 5. Reconstruction measurements for sea surface temperature (SST, in °C) and sea surface salinity (SSS, in PSU) for Site U1313 using the n=667 modern calibration dataset.

Parameter	Reconstruction	Reconstruction
	Measurement (Max)	Measurement (Min)
SST_ February (°C)	11.94	3.00
SST_ August (°C)	17.84	9.49
SSS_ February (PSU)	35.6	34.7
SSS_ August (PSU)	35.6	34.6

Of interest are the intermittent increases (spikes) in sea surface salinity between 830 and 850 ka (Figure 23) that correspond with an increase in cool-water dinoflagellate cysts. MAT reconstructions of SST in MIS 21 show significant fluctuations.

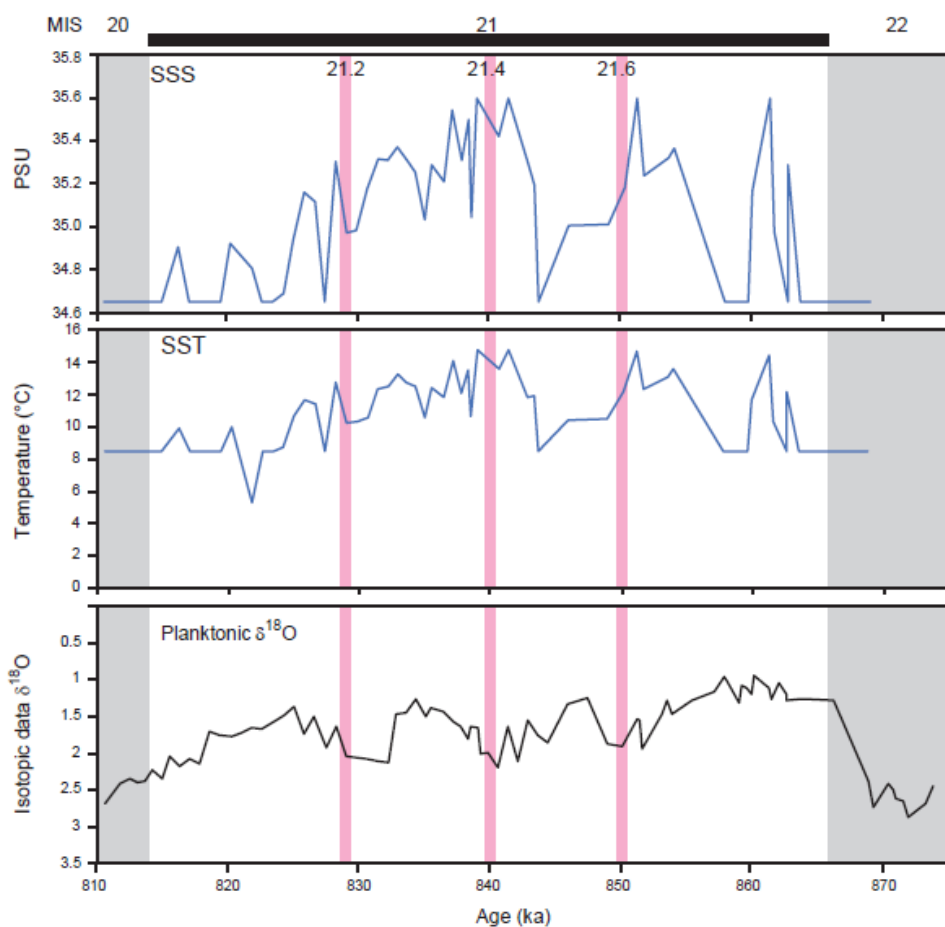


Figure 23. Plot of planktonic foraminiferal (*G. bulloides*) $\delta^{18}\text{O}$ data against reconstructed primary productivity, sea surface temperature, and sea surface salinity using MAT n=667. Isotopic units (‰VPDB)

5.10 STATISTICAL ANALYSIS

5.10.1 CANONICAL CORRESPONDENCE ANALYSIS

Canonical correspondence analysis (CCA) was carried out using XLstats 2017 software to relate the abundance of dinoflagellate cyst species to environmental variables (Figure 24). Using data from Site U1313, the null (H_0) and alternative (H_a) hypotheses were also tested. The H_0 states that the species data are not linearly related to the sites/variables data, whereas the H_a states that the species data are indeed linearly related to the sites/variables data. The computed p-values were lower than the significance level $\alpha=0.05$, which meant that the null hypothesis H_0 be

rejected in favour of the alternative hypothesis H_a . The risk of rejecting the null hypothesis H_0 as is true is lower than 0.01% (Table 6).

Table 6 Showing results on permutations calculated to the test the null and alternative hypotheses using XLstats software.

Permutations	500
Pseudo F	1.746
p-value	<0.0001
alpha	0.050

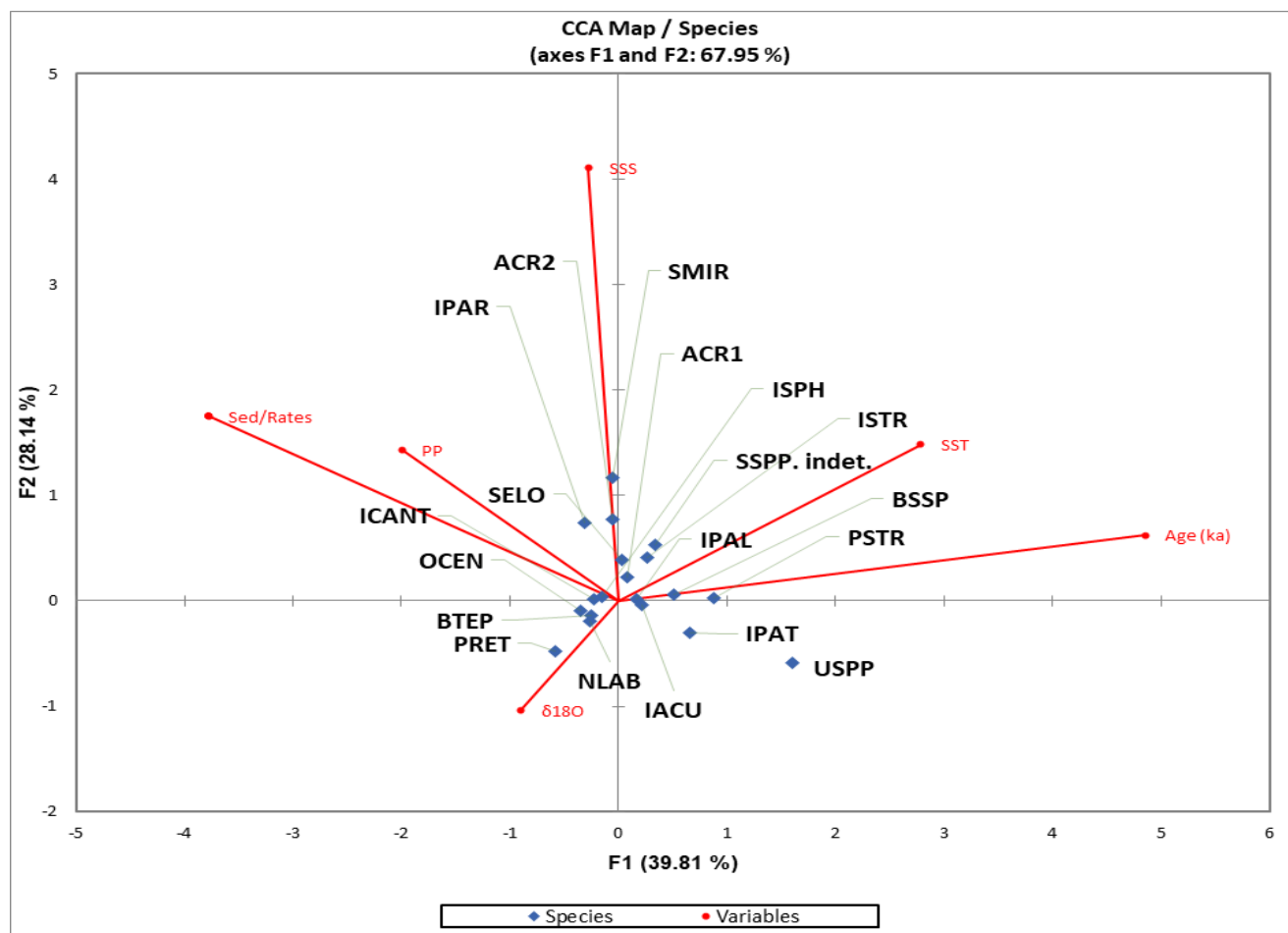


Figure 24. Canonical correspondence analysis (CCA) for samples and species in U1313, with $\delta^{18}\text{O}$, SST, SSS, primary productivity, sedimentation rates, and age as constraining factors. For taxa abbreviations see Table 1.

Within the Canonical Correspondence Analysis eigenvector analysis, most of the inertia is carried by the first axis. With the second axis, 67.95% of the inertia is obtained (Table 7). This means that the two-dimensional Canonical Correspondence Analysis map is sufficient to analyse the relationships between the dinoflagellate cyst species and the variables existing for the studied interval at Site U1313.

Table 7 Showing eigenvalues and percentage of inertia for CCA at Site U1313

	F1	F2	F3	F4	F5	F6
Eigenvalue	0.128	0.090	0.070	0.021	0.008	0.004
Constrained inertia (%)	39.806	28.142	21.846	6.476	2.442	1.288
Cumulative %	39.806	67.948	89.793	96.270	98.712	100.000
Total inertia	14.647	10.355	8.038	2.383	0.899	0.474
Cumulative % (%)	14.647	25.001	33.040	35.422	36.321	36.795

The canonical map above (Figure 24) shows that the frequency of *Spiniferites* sp. 1 is associated with age. *Impagidinium paradoxum*, *Spiniferites mirabilis* group and *Acritarch* sp. 2 are most strongly associated with high salinity (SSS based on the MAT for U1313). *Pyxidinopsis reticulata* seems to be affected or sensitive to sedimentation rates. On the other hand, "*Pyxidinopsis striolatoconulus*" is associated with low temperatures (SST based on the MAT for U1313). The bulk of the remaining species are closely clustered together and their frequency is associated with low salinities.

5.10.2 DETRENDED CORRESPONDENCE ANALYSIS

According to the species distribution in the DCA plot (Figure 25), dinoflagellate-DCA axis 1 reflects the MAT-derived SST. Dinoflagellate cyst species today associated with low temperatures (e.g. *Pyxidinopsis reticulata*, *Impagidinium pallidum*, and *Spiniferites elongatus*) ordinated on the negative part of DCA axis 1, whereas species that can survive in a wide range of conditions including warm water (e.g. *Spiniferites mirabilis*, *Operculodinium centrocarpum* sensu Wall and Dale 1966, and *Impagidinium aculeatum*) ordinated over the positive side of the same axis. Of interest is *Spiniferites*

sp. 1, recorded only in the bounding glacial MIS 22, which occupies the extreme end of axis 1.

Dinoflagellate-DCA axis 2 (Figure 25) in turn seems to be associated with nutrients, indicating a slight increase in nutrient enriched waters from left to right with the predominantly oligotrophic species *Impagidinium patulum* obtaining negative scores. Species that have wide ecological tolerances but that generally prefer lower trophic level waters or that have an ecological advantage when nutrients become limiting (e.g. *Nematosphaeropsis labyrinthus*, *Impagidinium aculeatum*) obtained positive DCA axis 2 scores.



Figure 25. Detrended correspondence analysis plot with dispersion of species at Site U1313 see Table 1 for abbreviations.

The DCA plot scatters the following, *Impagidinium aculeatum*, *Impagidinium paradoxum* and *Impagidinium patulum* despite these having similar distributions in modern sediments. These species are commonly found in oceanic and temperate to equatorial environments (Zonneveld et al., 2013) although each has its own particular set of ecological requirements. *Nematosphaeropsis labyrinthus* has low values on both axis 1 and 2, and this points to its cosmopolitan nature thriving successfully when nutrients have dwindled. *Spiniferites mirabilis*, *Impagidinium paradoxum* and *Operculodinium centrocarpum* sensu Wall and Dale (1966) are clustered together on the positive side of axis 1 in the DCA plot reflecting warm oligotrophic to slightly nutrient-enhanced waters of the central North Atlantic. These species appear to thrive in both oligotrophic and nutrient-enhanced conditions reflected in axis 2 of the DCA plot. This scenario points to change in the water properties at Site U1313 from warm and oligotrophic waters of the sub-tropical gyre to more eutrophic under the influence of the sub-polar gyre.

5.10.3 CLUSTER ANALYSIS

A clustered dendrogram (Figure 26) produced using R software was used to subdivide the palynological record into assemblage biozones, based on distinctive palynological relations, both for descriptive and paleoenvironmental purposes. Nine biozones are recognised. They are numbered from oldest to youngest, and the bounding samples and their ages are specified. Each is characterised below.

i. Assemblage biozone 1 (MD02–MD08; 873.793–870.534 ka)

This biozone is dominated by *Impagidinium aculeatum* varying between 9.49 and 35%. Other significant species important in this biozone are *Nematosphaeropsis labyrinthus* (7–25%), *Impagidinium cantabrigiense* (1–23%), *Impagidinium patulum* (4.65–18%) and *Impagidinium pallidum* (0–21%). Of interest is the gradual decline of *Spiniferites*

sp. 1 from the top of the biozone to the bottom with a relative abundance varying between 0 and 12%. Biozone 1 is also marked by the lowest occurrence of *Acritarch* sp. 1.

ii. Assemblage biozone 2 (MD10/A–MD36; 869.370–858.148 ka)

This biozone is characterized by the continued dominance of *Impagidinium aculeatum* (17–39%). *Nematosphaeropsis labyrinthus* (13–34%) continues to have a significant presence together with “*Pyxidinospis striolatoconulus*” (2.43–15%). There is a significant increase of *Impagidinium patulum* from the base of the biozone (4.32%) to the top (23%). This biozone marks the lowest occurrence of *Fibrocysta fusiforma* and is represented consistently throughout the zone with abundances ranging between 1.6 and 4.0%. This biozone is characterized by the highest occurrence of *Spiniferites* sp. 1. Also noteworthy is the sudden decline in *Impagidinium pallidum* (0–4.34%) in comparison with biozone 1.

iii. Assemblage biozone 3 (MD36/A – MD41/A; 857.850–853.627 ka)

This narrow biozone comprises five samples, and is characterised by a continued dominance of *Impagidinium aculeatum* (34–64%), with peak dominance in the middle of the biozone. *Nematosphaeropsis labyrinthus* continues to be significant, varying between 9 and 31%. There is a decline in *Impagidinium patulum* (0.5–8.16%) and *Operculodinium centrocarpum* (1–4.24%) in comparison with biozone 2. This biozone is also marked by the presence of a single specimen of *Protoperidinium stellatum*.

iv. Assemblage biozone 4 (MD41–MD54; 853.220–843.672 ka)

This biozone is characterized by the co-dominance of *Impagidinium aculeatum* (17–31%) and *Nematosphaeropsis labyrinthus* (17–32%). There is a continued decline of *Impagidinium patulum* with relative abundance varying between 0 and 4.9%. The cyst of *Protoperidinium stellatum* is consistently present from the base of the biozone through the middle, disappearing from the biozone at the top. This biozone is also

marked by the lowest occurrence of *Acritarch* sp. 2 with relative abundances varying between 0 and 15%. There is also a gradual decrease in *Operculodinium centrocarpum* sensu Wall and Dale (1966) from the base of the biozone to the top (1.66–13%). A single specimen of *Achomosphaera andalousiensis* was also identified.

v. Assemblage biozone 5 (MD54/A–MD61; 843.419–838.565 ka)

This biozone is marked by a continued decline in *Impagidinium patulum* (0.32–3.9%) and also a decline in *Nematosphaeropsis labyrinthus* (3.58–26%) and *Impagidinium aculeatum* (5.86–24%) which are consistently abundant in the lower biozones. An abrupt decline in the cyst of *Protoperidinium stellatum* is also noted with just two specimens recorded in the entire biozone. Increases relative to biozone 4 were recorded for *Operculodinium centrocarpum* (3–16%), *Acritarch* sp. 2 with its highest abundance at 27% in the middle of the biozone, and *Impagidinium paradoxum* (12–22%). Also noted are increases in *Spiniferites mirabilis* to between 1.30 and 10%, and *Impagidinium pallidum* with a peak at 8.07% in the middle of the biozone.

vi. Assemblage biozone 6 (MD61/A–MD70; 838.331–832.938 ka)

This biozone features a sharp decline in *Operculodinium centrocarpum* (5.15–7.9%) compared with biozone 5. Other noteworthy declines in relative abundances are documented for *Impagidinium paradoxum* (2.33–13%) and *Impagidinium pallidum* (0–4.63%). There is an increase in *Impagidinium aculeatum* with peak abundance recorded at the base of the biozone at 26%. *Nematosphaeropsis labyrinthus* also records an increase, with a peak abundance in the middle of the biozone at 31%. A slight increase in *Impagidinium patulum* also occurs. Eight specimens of *Fibrocysta fusiforma* were recorded in biozone 6 (0.3–2%).

vii. Assemblage biozone 7 (MD71–MD79; 832.234–825.867 ka)

This biozone is characterized by the continued co-dominance of *Impagidinium aculeatum* and *Nematosphaeropsis labyrinthus* with average abundances of 24 and

23%, respectively. Peak dominance of *Impagidinium aculeatum* is noted at the base of the biozone with an abundance of 42% whereas that of *Nematosphaeropsis labyrinthus* occurs in the middle of the biozone with a peak abundance of 35%. A sudden increase in relative abundance is also noted for *Operculodinium centrocarpum* (9.8–31%) which is characterized by an increase in abundance from the base of the biozone to the top. *Bitectatodinium tepikiense* (0.92–7.14%) also increases in this zone. A decline in *Impagidinium paradoxum* (0–4.30%) is also noted.

viii. Assemblage biozone 8 (MD80–MD84; 825.067–821.867 ka)

Another characteristically narrow biozone comprising just 5 samples. *Nematosphaeropsis labyrinthus* strongly dominates throughout, with abundances between 49 and 73%. *Impagidinium aculeatum* shows a sharp decline relative to biozone 7, with abundances varying between 8.82 and 16%. An increase in *Operculodinium centrocarpum* is also noted from the base to the top, with a peak abundance of 19% recorded at the top of the biozone with 4.24% recorded at the base of the biozone. A slight increase in the relative abundance of *Impagidinium paradoxum* is also noted (1.98–4.67%). Most of the other dinoflagellate taxa, including *Impagidinium patulum*, *Pyxidinopsis reticulata*, *Bitectatodinium tepikiense*, and *Brigantedinium* spp., have abundances of less than 1% in biozone 8.

ix. Assemblage biozone 9 (MD85–MD100; 821.067–810.582 ka)

This biozone is characterized by the continued dominance of *Nematosphaeropsis labyrinthus* (34–48%). Other increases in abundances are noted in *Impagidinium aculeatum* (14.9–26%), *Impagidinium pallidum* (0–7.66%), *Impagidinium patulum* (0.32–13%), and *Operculodinium centrocarpum* (4.19–19%). A slight increase in the relative abundance of *Impagidinium paradoxum* (1.97–7.33%) is also noted in this biozone. *Fibrocysta fusiforma* was also recorded in this biozone with an abundance of 2.6%.

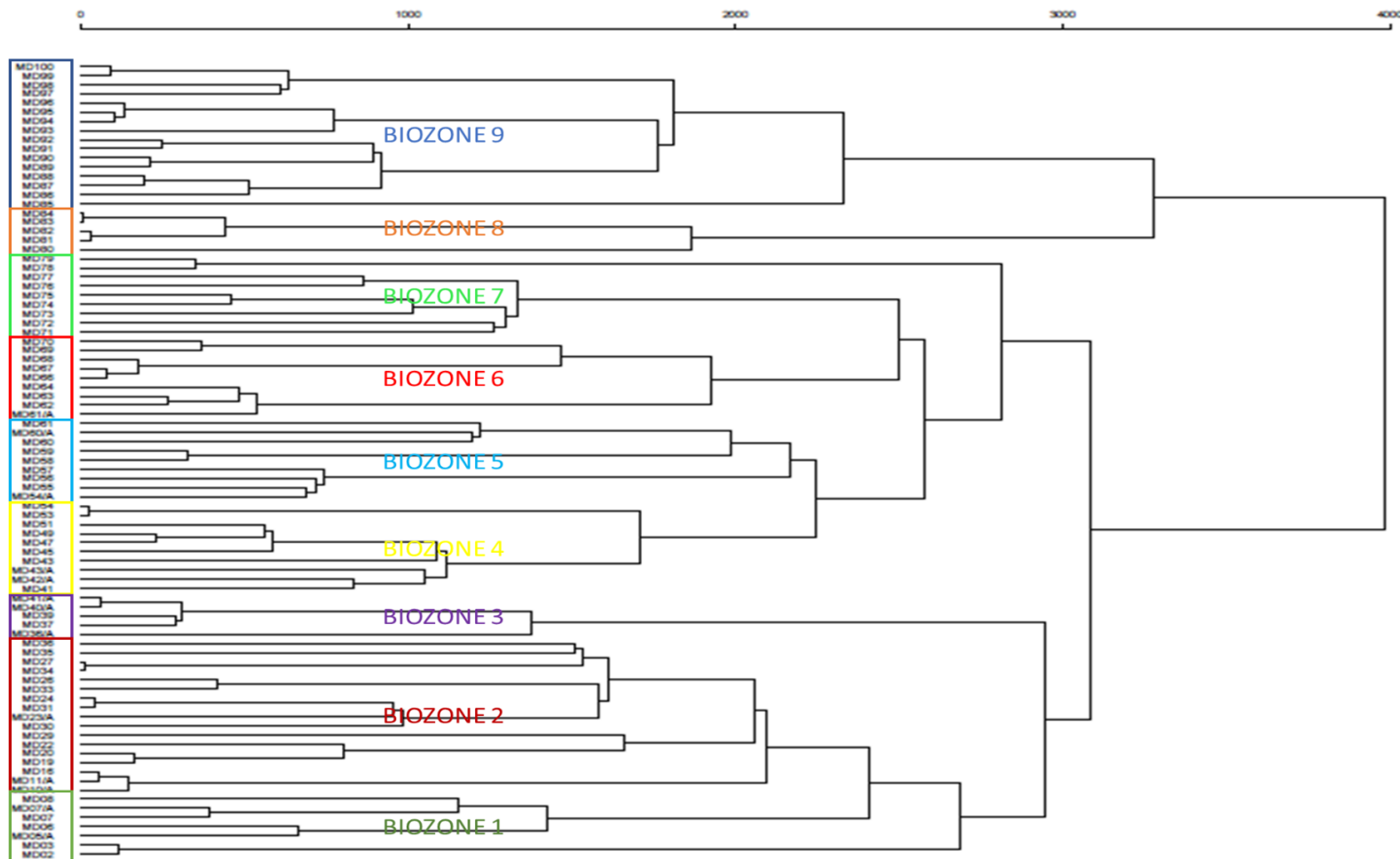


Figure 26. Constrained cluster analysis for Site U1313, with assemblage biozones shown by colour coded rectangles and their corresponding labels on the right.

5.10.4 SPECIES RICHNESS AND EVENNESS

The diversity index for Site U1313 was calculated. A diversity index as explained earlier is a measure of species diversity in a community and made up of two components, species richness and evenness (Figure 27). Species richness is the number of species occurring in each sample. The average species richness for the interval is 15 species. The lowest species richness of 6 was recorded in sample MD30 (862.023 ka) and the highest species richness of 22 species was recorded in sample MD64 (836.455 ka).

This study also considered species evenness (Figure 27). It looked at how dinoflagellate taxa are distributed in each sample. High species evenness occurs in a sample when all taxa share the same abundance and are equally distributed. The interval between 810 and 820 ka has a characteristically high species evenness with minimal fluctuations when compared with the remainder of the interval. The period between 820 and 870 is very variable with peak evenness reaching 0.64 and lowest recorded evenness of 0.09. None of the samples yielded species evenness of 1.

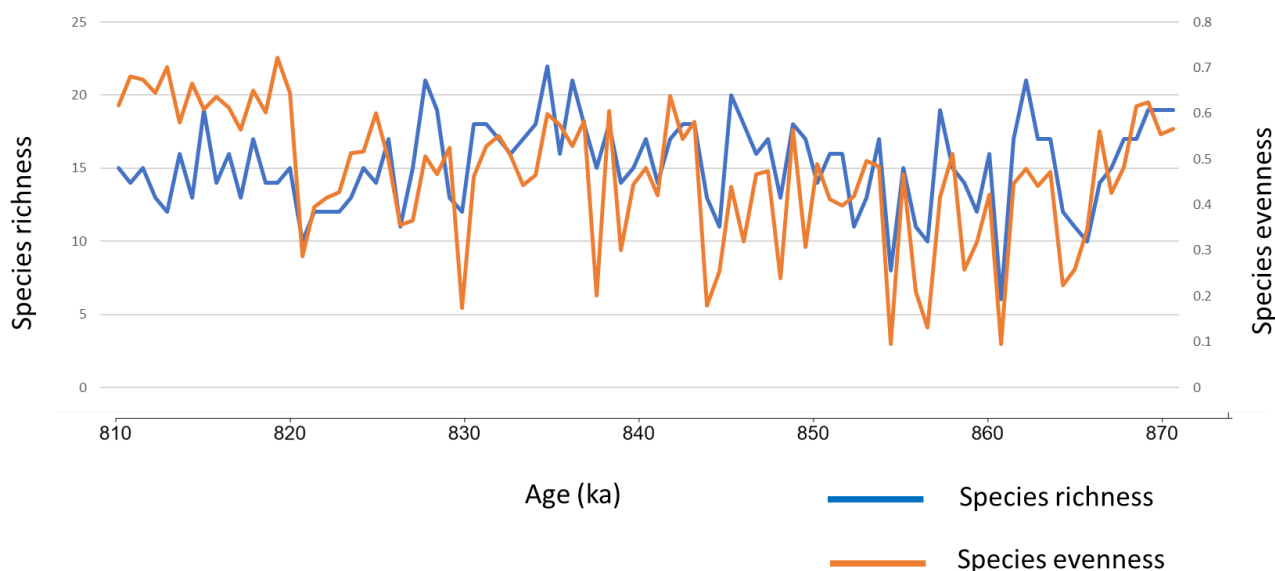


Figure 27. Plot showing species richness and evenness for Site U1313.

6 DISCUSSION

6.1 Dinoflagellate Cysts Preservation and Primary Productivity

Different species of dinoflagellate cysts have different preservation potentials which can potentially affect the accuracy of paleoenvironmental reconstructions. Studies have shown, for example, that protoperidiniacean cysts are more prone to degradation than gonyaulacaceans, explaining the need to exercise caution when using protoperidiniaceans in reconstructions of primary productivity (Zonneveld et al., 1997; Zonneveld et al., 2002). Nonetheless, Reichart and Brinkhuis (2003) have noted that trends in *absolute* protoperidinioid cyst abundances remain positively correlated with productivity even after prolonged oxygenation. Dinoflagellate cysts from the studied interval of Site U1313 appear well preserved, with walls of sensitive cysts, notably heterotrophic taxa, showing no signs of degradation. This suggests that the record contains a meaningful signal for productivity. *Brigantedinium* spp. is consistently present throughout the sampled interval and individual specimens of *Selonopemphix quanta* are also occasionally present, and as heterotrophic taxa feeding on diatoms and other primary producers they can be considered as reliable indicators of productivity and hence enhanced nutrient levels (Figure 15).

A plot of planktonic isotopic data against MAT-reconstructed primary productivity (Figure 22) shows that a general increase in $\delta^{18}\text{O}$ is met with a corresponding decrease in primary productivity. There are three major intermittent increases in primary productivity between 830 and 866 ka during MIS 21, with peak primary productivity at 866 ka. The corresponding increases in productivity for the three peaks is associated with lighter $\delta^{18}\text{O}$ values, low SST and SSS, and with an increase in *O. centrocarpum* relative abundance which signals the presence of nutrient rich waters of the NAC over Site U1313 – a site predominantly influenced by oligotrophic waters of the sub-tropical gyre. Outside of these peaks, a composite plot (heterotrophic cysts, *O. centrocarpum*, and MAT-reconstructed primary productivity) suggests that an increase in SST results

in warmer oceans, resulting in stratification of the surface mixed layer, which then inhibits the entrainment of nutrients from below this surface mixed layer and reduces primary production. Research by Aubry et al. (2016) and de Wet et al. (2016) on the warm “super interglacial” MIS 31 showed that warming resulted in the stratification of the water column, with low salinity surface waters attributed to the influx of meltwater from glaciers. This assertion is supported by low $\delta^{18}\text{O}$ values obtained from analysed foraminifera (*Uvigerina peregrina* and *Cibicidoides wuellerstorfi*) which is presumably a reflection of very low volumes of continental ice during intense interglacials. Increase in the relative abundance of heterotrophic dinoflagellate cysts is presumably an outcome of prey abundance and hence of nutrient availability (Figure 15). Intermittent increases in the relative abundances of heterotrophic dinoflagellate cysts during isotopically light intervals (after 855 ka) are characterized by reduced MAT-reconstructed primary productivity, although it is not clear why this is. *O. centrocarpum*, which is used to map the NAC, is also low during these intervals.

6.2 *Fibrocysta? fusiforma* Edwards, 1984

Fibrocysta? fusiforma was first described by Edwards (1984) from the Upper Miocene of the Rockall Plateau, eastern North Atlantic, and placed provisionally within the genus *Fibrocysta* because the processes and central body wall of this species are smooth rather than fibrous. There are surprisingly few reports of this species in the literature. Santarelli et al. (1998) reported *F.? fusiforma* from the Upper Miocene of Crete (Greece), and Versteegh (1997) reported it persistently between 2.8 and 2.3 Ma in DSDP Holes 607/607A in the central North Atlantic, and between 2.7 Ma and ~2.3 Ma in the Singa section, Italy. Versteegh et al. (1996) considered it to be an oceanic species, an interpretation supported by the present study. Specimens in the present study are fairly well preserved and show no physical indication of being reworked. Moreover, within its known range, *F.? fusiforma* does not typically occur in abundances more than about 4% (e.g. Versteegh, 1997), minimizing the likelihood of recycling into

younger sediments. In the present study, *F.?* *fusiforma* has a relative abundance fluctuating between 0 and 4.35%, a consistent presence between 864.316 and 857.254 ka, and a highest occurrence at 812 ka. This extends the range of this species at least into the latest Early Pliocene. Its peak relative abundance is highest during low isotopic $\delta^{18}\text{O}$ values which implies a preference for warmer SST (Figure 15). The DCA plot (Figure 25) shows *F.?* *fusiforma* having a negative score on the axis 2 which is associated with reduced nutrients. Its plot close to the meso-oligotrophic species *I. patulum* gives this species an assumed oceanic / oligotrophic preference.

6.3 *Spiniferites* sp. 1

This species has a spherical central body bearing characteristically short processes (Plate 5, figs. 1–3) that have both bifurcate and trifurcate terminations, indicating gonol and intergonol processes. It has been identified only in the upper part of bounding glacial MIS 22. It has a relative abundance of between 0 and 12%, which decreases towards MIS 21. The DCA plot (Figure 25) axis 1 shows this species to have a high preference for low SST and it occupies the extreme end of axis 1 on the negative side, and also has a preference for high nutrient waters (axis 2). *Spiniferites* sp. 1 is restricted to the sampled interval between 873.793–864.316 ka. This species warrants further investigation, as it may prove to be biostratigraphically as well as paleoecologically valuable.

6.4 Climate Instability of MIS 21

Research on MIS 21 by Ferretti et al. (2010) using sediment upon which the present study is based has shown this interval to be very climatically unstable (Figure 1). The high-resolution stable isotope records from benthic and planktonic foraminifera resolved MIS 21 into four interstadials and has been correlated across the North Atlantic Ocean (Figure 3). Ruddiman et al. (1986) working on sediments from DSDP Site 607 compressed this stage into a single obliquity cycle, work by Hilgen in 1991 interpreted it as having two obliquity cycles, and Bassinot et al. (1994) working on core

obtained from the tropical Indian Ocean identifying three peaks that he attributed to precession cycles. In this study the $\delta^{18}\text{O}$ signature used is that of the planktonic foraminifera *G. bulloides* as it records the full glacial–interglacial SST range in the North Atlantic, along with global ice volume and SSS effects (Ferretti et al., 2010). The findings on foraminiferal analysis at IODP Site U1314 by Hernandez-Almeida et al. (2012) covering the period MIS 31–MIS 19 in the North Atlantic Ocean concur with the earlier work of Ferretti et al. (2010) in showing climatic instability during MIS 21. In particular, the benthic foraminifera *C. wuellerstorfi* has similar interstadial periods for MIS 21 as described by Ferretti et al. (2010) (Figure 28A), *Neogloboquadrina pachyderma*, a planktonic polar foraminifera which is used to map the Arctic Front (AF), was generally low during MIS 21 (Figure 28B), and the Shannon Diversity Index (H) for planktonic foraminifera is high, indicating higher diversity during the interglacial (Figure 28C).

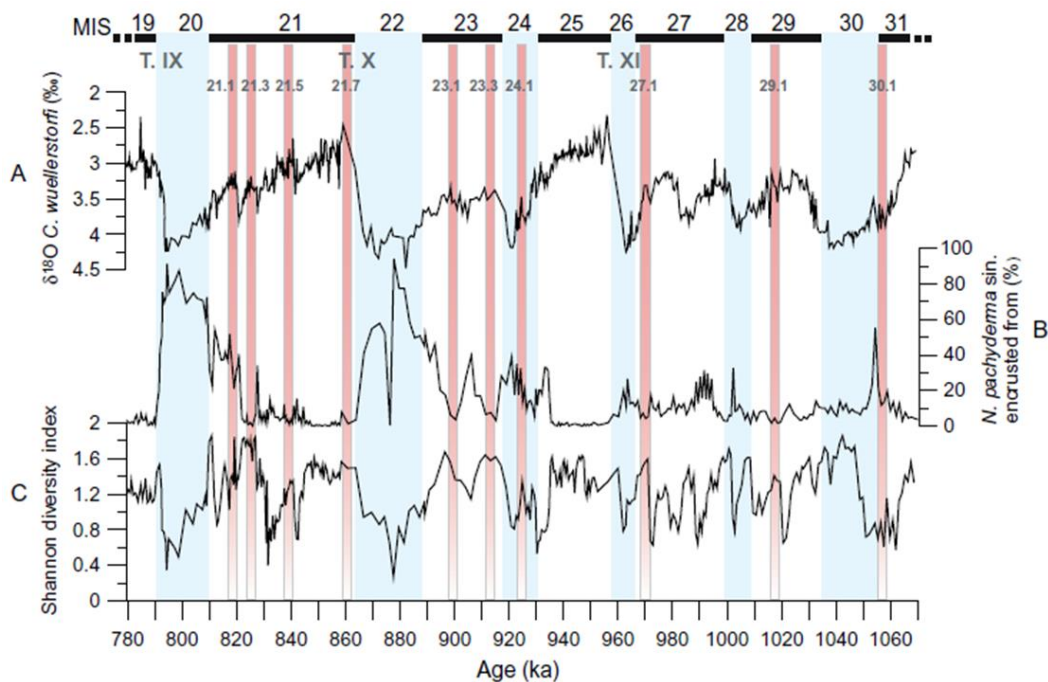


Figure 28. North Atlantic IODP Site U1314 records from 1069 to 779 ka. A. Benthic $\delta^{18}\text{O}$. B. Relative abundance of *N. pachyderma* sin. encrusted morphotype. C. Shannon diversity index (H). Glacial marine isotope stages (MIS) are shown with blue vertical bars. Suborbital-scale climate events (Hernandez-Almeida et al., 2012, fig. 3).

In the present study, the integration of two high resolution data sets (stable isotopes and dinoflagellate cysts from the same sample set) helps to clarify the evident paleoceanographic instability during MIS 21. Of particular importance are the following groups: cool-water dinoflagellate cyst indicators (Figure 14), heterotrophs (Figure 15) and *O. centrocarpum* (Figure 14) which has been identified as a tracer of the NAC in the northern hemisphere. In addition, the use of data (primary productivity and SST) generated using MAT contribute to a wider understanding (Figure 22). The primary productivity data show three peak periods around 831.466, 837.158 and 866.342 ka which has been interpreted to show the presence of the NAC over Site U1313. The southward shift of the NAC is supported by evidence of increased *N. pachyderma* presence in two peaks over Site U1314 during MIS 21, implying the south-eastward shift of the AF which then forces the NAC further southwards (Hernandez-Almeida et al., 2012). MIS 21 is known to have been interrupted by cold episodes and the three peaks labelled as MIS 21.2, 21.4 and 21.6 by Ferretti et al. (2010) closely coincide with cold peaks identified by Hernandez-Almeida et al. (2012) (Figure 1, Figure 28). The SSS plot in the present study shows a number of major intermittent peaks between 830 and 840 ka that are offset from the two major identified cooling episodes at 831.466 and 837.158 ka. During peak productivity, there is a gradual increase in the relative abundance of the NAC indicator *O. centrocarpum*. Furthermore, during periods of low $\delta^{18}\text{O}$, primary productivity is low possibly due to water mass stratification which results in the reduced upwelling of nutrients from deeper waters.

6.5 Paleocceanography changes in the North Atlantic Ocean

Stable isotopic data ($\delta^{18}\text{O}$) are combined with high-resolution dinoflagellate cyst data from the same sample set to show the influence of the subarctic front and NAC at Site U1313 through MIS 21. Site U1313 is predominantly bathed in oligotrophic waters of the subtropical gyre during interglacials, and during glacials the expansion of ice sheets to the north forces the nutrient rich NAC to shift southwards over Site U1313.

The bounding glacial MIS 22 (Biozone 1 and part of Biozone 2). Biozone 1 is dominated by *Impagidinium aculeatum* varying between 9.49 and 35%. Other significant species important in this biozone are *Nematosphaeropsis labyrinthus* (7–25%), *Impagidinium cantabrigiense* (1–23%), *Impagidinium patulum* (4.65–18%) and *Impagidinium pallidum* (0–21%). Highest relative abundances of *I. aculeatum* occur in central oceanic oligotrophic environments (Zonneveld et al., 2013). The co-dominance of *N. labyrinthus*, a subpolar species in this zone in addition to elevated abundances of *B. tepikiense*, *I. pallidum* and *Brigantedinium* spp. is evidence of cool nutrient-rich waters typical of the subarctic gyre. *Brigantedinium* spp. signals enhanced nutrients. The subarctic gyre persisted over Site U1313 and retreated rapidly at end of Biozone 1 (Figure 29).

Biozone 2 coincides with a sharp decline in the planktonic isotopic values ($\delta^{18}\text{O}$) signalling the rapid retreat of the subarctic front and ushering in oligotrophic conditions of the subtropical gyre (Figure 29). This biozone is characterized by the continued dominance of *Impagidinium aculeatum* (17–39%). *Nematosphaeropsis labyrinthus* (13–34%) continues to have a significant presence together with “*Pyxidinosia striolatoconulus*” (2.43–15%). There is a significant increase of *Impagidinium patulum* from the base of the biozone (4.32%) to the top (23%). The inferred presence of oligotrophic conditions is further supported by low numbers of *O. centrocarpum* and a decline of the nutrient indicator *Brigantedinium* spp.

Biozone 3 coincides with increasingly heavy planktonic isotopic values ($\delta^{18}\text{O}$) but is dominated by *Impagidinium* spp. and remains under the influence of the subtropical gyre (Figure 29). This biozone is characterised by a continued dominance of *Impagidinium aculeatum* (34–64%), with peak dominance in the middle of the biozone at 854.033 ka. *Nematosphaeropsis labyrinthus* continues to be significant, varying between 9 and 31%. There is a decline in *Impagidinium patulum* (0.5–8.16%)

Biozone 4 reflects nutrient-elevated conditions and is characterized by the brief shift to cooler conditions as seen by the increase in abundance of the *Brigantedinium* spp. peaking at 9% at 847.457 ka. This zone coincides with an increase in planktonic isotopic values at the beginning of the zone, peaking around 854 ka, and then a sudden decline in the middle of the zone and increasing again towards the end of the Biozone 4 (Figure 29). This biozone is characterized by the co-dominance of *Impagidinium aculeatum* (17–31%) and *Nematosphaeropsis labyrinthus* (17–32%).

Biozone 5 is characterized by peak summer temperature (MAT) recorded in the studied interval. There is a notable increase in *O. centrocarpum* concentration and a slight decline in *N. labyrinthus* from the bottom of the zone moving to the top (Figure 29). An increase in *I. pallidum* and *B. tepikiense* is also noted. This interval represents the heaviest planktonic foraminiferal isotope values of MIS 21 peaking at 842 ka. In Biozone 5 begins to show a modest influence of the NAC although it is not fully established over Site U1313.

Biozone 6 This biozone reflects a lightening of planktonic foraminiferal $\delta^{18}\text{O}$ values, dominated by *Impagidinium* spp. and is indicative of the influence of the subtropical gyre over Site U1313. This biozone features a sharp decline in *Operculodinium centrocarpum* (5.15–7.9%) compared with biozone 5. Other noteworthy declines in relative abundances are documented for *Impagidinium paradoxum* (2.33–13%) and *Impagidinium pallidum* (0–4.63%). There is an increase in *Impagidinium aculeatum* with peak abundance recorded at the base of the biozone at 26%. *Nematosphaeropsis labyrinthus* also records an increase, with a peak abundance in the middle of the biozone at 31% (Figure 29).

Biozone 7–9 (835–810 ka) is characterized by the sudden increase in *O. centrocarpum*. *O. centrocarpum* is a cosmopolitan species and is used as a tracer of the NAC (Rochon et al., 1999). Analysis of the *O. centrocarpum* trend in MIS 21 shows

a consistent presence and peak relative abundance between 828 and 832 ka indicating the strong influence of the NAC over U1313 and implying cooler conditions. The above assertion is supported by the sudden increase in $\delta^{18}\text{O}$ values coupled with an increase in presence of heterotrophic dinoflagellate cysts and peak productivity during this interval (Figure 29). The other bounding glacial, MIS 20, is dominated by *N. labyrinthus* (biozone 9) which also dominates the latter part of MIS 21. In summary, the bounding glacial MIS 22 was under the influence of the subpolar gyre whereas at least the early part of MIS 20 was under the influence of the NAC which implies a southward shift of this current over Site U1313 introducing nutrient-enhanced waters and displacing southwards the oligotrophic waters of the subtropical gyre. MIS 21 was predominantly under the influence of the subtropical gyre and was intermittently interrupted by two major cooling periods between 830 and 840 ka, signalling the return of the NAC to Site U1313 during MIS 21.

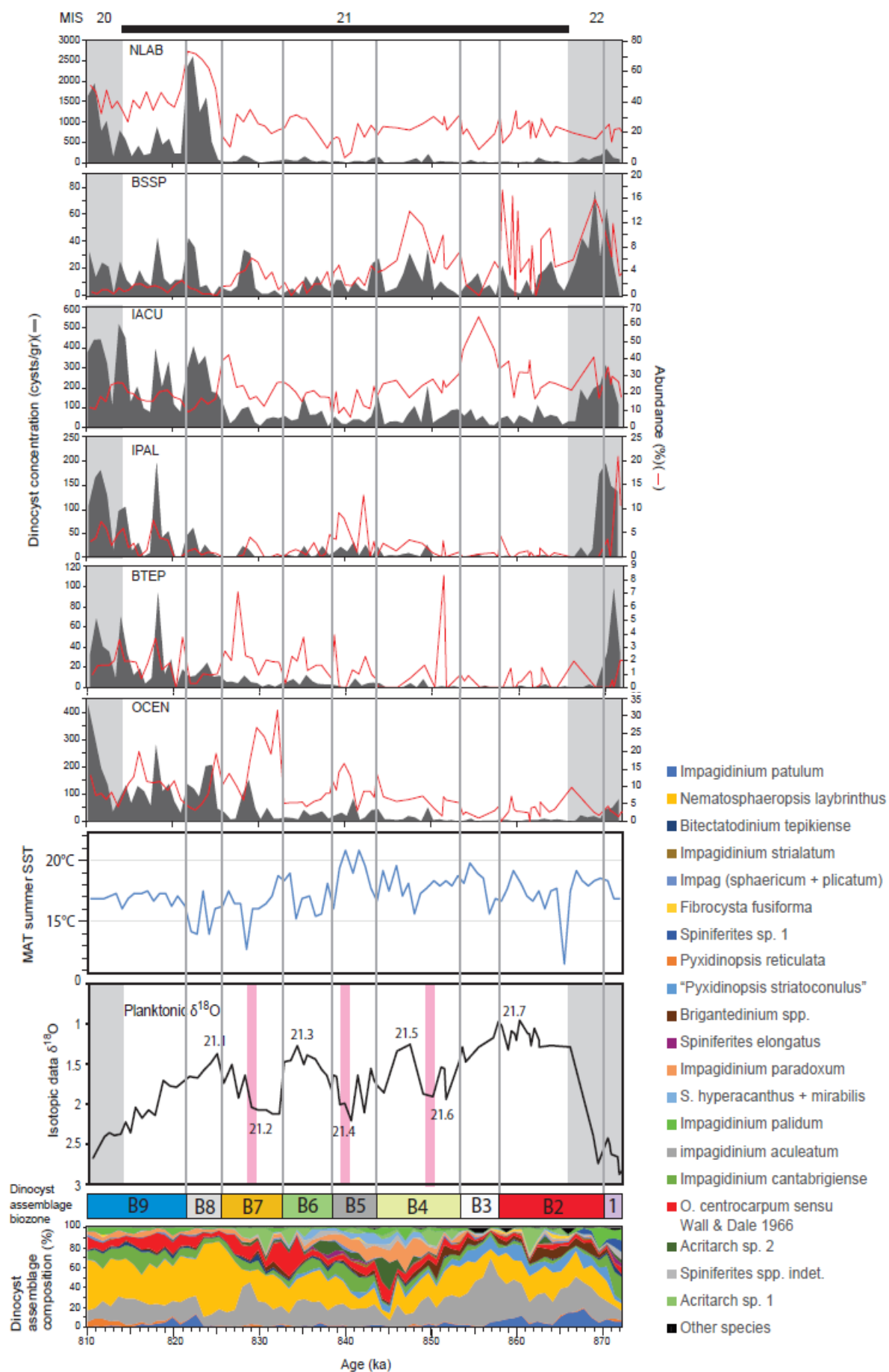


Figure 29 Showing dinoflagellate cyst concentrations for selected indicator species. *Operculodinium centrocarpum* sensu Wall & Dale: North Atlantic Current; *Nematosphaeropsis labyrinthus*: subpolar waters; *Impagidinium aculeatum*: subtropical gyre; *Impagidinium pallidum*: subarctic front; *Brigantedinium* spp. and *Bitectodinium tepikiense*: elevated nutrient indicators. Reconstructed summer sea surface temperatures (this study). Planktonic $\delta^{18}\text{O}$ VPDB. Marine Isotope Stages 20, 21, and 22. Assemblage biozones (1–9). Dinocyst assemblage composition graph.

6.6 Reliability of paleo-reconstructions using MAT

Validation tests performed on the studied samples demonstrate that MAT can be used with reasonable confidence to reconstruct past climate parameters in the North Atlantic Ocean (Figure 20). The climate parameters for Site U1313 using dinoflagellate cyst assemblages were reconstructed using those from modern dinoflagellate assemblages. According to Telford (2006), validations from MAT over-estimate accuracy because of spatial autocorrelation. However, spatial autocorrelation is not a major issue with MAT when using a dinoflagellate database characterized by large environmental gradients (Guiot and de Vernal., 2011). Values of correlation coefficients so obtained suggest that the sea surface parameters can be reconstructed with reasonable confidence for example;

$$\text{SST_Feb } (r^2=0.97)$$

$$\text{SST_Aug } (r^2=0.95)$$

$$\text{SSS_Feb } (r^2=0.71)$$

$$\text{SSS_Aug } (r^2=0.73)$$

Given the correlation coefficients, confidence in the SST predictions is better than for SSS, reiterating the need for caution when interpreting the SSS parameter. The RMSE, which is the standard deviation of the residuals or differences between observed and reconstructed values for each climatic parameter, is deemed to be within reasonable range for SST (Figure 20). The MAT method has notable constraints such as:

(1) Sea surface parameters (PP, SST, SSS etc.) are treated as independent variables yet in space they interact controlling the distribution of dinoflagellate cysts (Verleye and Louwye, 2010).

(2) The accuracy of the MAT is heavily dependent on the region analysed for the modern analogue. In this study, the modern-day calibration dataset used has no representative samples from the open waters of the central North Atlantic Ocean. Hence, the dataset does not strictly share the same environmental variables as the fossil assemblages being interpreted (Mantilla, 2013).

Overall, however, the validation tests (Figure 20) and the climate reconstructions performed from Site U1313 in the North Atlantic Ocean demonstrate the robustness of MAT, especially with regards to the SST. The SST, SSS and PP reconstructions show two major cooling events between 830 and 840 ka which is consistent with the two identified cooling periods during MIS 21 using stable isotopic data ($\delta^{18}\text{O}$).

7 SUMMARY AND CONCLUSIONS

Analysis of 111 palynological samples from the studied interval yielded a high-resolution dinoflagellate cyst record in which 18 genera and 22 species were identified. The stable isotope data and the high-resolution dinoflagellate cyst record together show interglacial MIS 21 to be climatically unstable. According to the dinoflagellate cyst record, MIS 21 was interrupted by two significant cold episodes between 830 and 840 ka. The two cold episodes are resolved using the relative abundance of cooler-water species and by tracking the abundance of *O. centrocarpum*, a species known in the North Atlantic to have affinities with the nutrient-elevated NAC. Activity of the NAC over Site U1313 is further supported by planktonic foraminiferal evidence, an increase in *N. pachyderma* at Site U1314 during the cold peaks implying the southward movement of the AF which displaced the NAC further southwards. Re-establishment

of oligotrophic waters over Site U1313 was achieved when the NAC shifted northwards.

The continuous presence of well-preserved *F.? fusiforma* at Site U1313 extends the stratigraphic range of this species from its previously documented range top in the Lower Pleistocene at 2.3 Ma (Versteegh, 1997) to ~812 ka in the present study. In addition, the continuous presence of *Acritarch* sp. 1 and *Acritarch* sp. 2 at Site U1313 is of interest. No information is available on these acritarchs from the literature. Additional morphological studies are needed to clarify their taxonomy, as their presence is significant in the studied interval, with the relative abundance of *Acritarch* sp. 1 reaching as high as 25.2% during 828 ka.

The application of MAT to central North Atlantic Site U1313 demonstrates that paleoenvironmental reconstructions are plausible but limited by the absence of central Atlantic Ocean samples in the calibration dataset. The SST, SSS and PP reconstructions nonetheless reflect two major cooling events between 830 and 840 ka as identified independently using $\delta^{18}\text{O}$ stable isotopic data.

In summary, the combination of stable isotopic data and the high-resolution dinoflagellate cysts data clarify paleoceanographic instability during MIS 21 including the presence of pronounced cooling events between 830 and 840 ka.

8 REFERENCES

Anderson, C., 1997, Transfer function vs. modern analog technique for estimating foraminiferal data, western equatorial Pacific Ocean Pliocene sea-surface temperatures based on planktic foraminiferal data, western equatorial Pacific Ocean: *Journal of Foraminiferal Research*, v. 27, no. 2, p. 123-132.

Backman, J., Moran, K., McInroy, D.B., Mayer, L.A., and the Expedition 302 Scientists Proceedings of the Integrated Ocean Drilling Program, Volume 302

Braak, C.T., 1986, Canonical Correspondence Analysis: A New Eigenvector Technique for Multivariate Direct Gradient Analysis: *Ecology*, Vol. 67, No. 5 pp. 1167-1179

Channell, J.E.T., Kanamatsu, T., Sato, T., Stein, R., Alvarez Zarikian, C.A., Malone, M.J., and the Expedition 303/306 Scientists Proceedings of the Integrated Ocean Drilling Program, Volume 303/306

de Vernal, A., Henry, M., Matthiessen, J., Mudie, P.J., Rochon, A., Boessenkool, K.P., Eynaud, F., Grosfeld, K., Guiot, J., Hamel, D., Harland, R., Head, M.J., Kunzpirrung, M., Levac, E., et al., 2001, Dinoflagellate cyst assemblages as tracers of sea-surface conditions in the northern North Atlantic, Arctic and sub-Arctic seas: The new "n= 677" data base and its application for quantitative palaeoceanographic reconstruction: *Journal of Quaternary Science*, v. 16, no. 7, p. 681–698, doi:10.1002/jqs.659.

de Vernal, A., and Mudie, P.J., 1989, Late Pliocene to Holocene palynostratigraphy at ODP Site 645, Baffin Bay: in Srivastava, S.P., Arthur, M., Clement B., et al., Proceedings of the Ocean Drilling Program, Scientific Results, v. 105, p. 387–399.

de Vernal, A., Turon, J.-L., and Guiot, J., 1993, Dinoflagellate cyst distribution in high latitude marine environments and quantitative reconstruction of sea-surface salinity, temperature, and seasonality: *Canadian Journal of Earth Sciences*, v. 31, p. 48–62.

de Vernal, A., Rochon, A., Radi, T., 2013, Paleooceanography, biological proxies: dinoflagellates: In: Elias S.A. (ed.) *The Encyclopaedia of Quaternary Science*, vol. 2, pp. 800-815.

Edward, L., 1984, Miocene dinocysts from deep sea drilling project leg 81, Rockall plateau, eastern north Atlantic Ocean: U.S. Geological Survey, pp. 582-594

Ferretti, P., Crowhurst, S.J., Hall, M.A., and Cacho, I., 2010, North Atlantic millennial scale variability 910 to 790 ka and the role of equatorial insolation forcing: *Earth and Planetary Science Letters*, v. 293, p. 28–41, doi: 10.1016/j.epsl.2010.02.016.

Ferretti, P., Crowhurst, B. David, A. Naafs, Carlo Barbante., The Marine Isotope Stage 19 in the mid-latitude North Atlantic Ocean: astronomical signature and intra-interglacial variability: *Quaternary Science Reviews* 108 (2015) p. 95-10

Gibbard, P.L., and Head, M.J., 2010. The newly-ratified definition of the Quaternary System/Period and redefinition of the Pleistocene Series/Epoch, and comparison of proposals advanced prior to formal ratification: *Episodes*, 33: 152–158.

Head, M.J., and Gibbard, P.L., 2005, Early–Middle Pleistocene transitions: an overview and recommendation for the defining boundary: Geological Society, London, Special Publications, v. 247, p. 1–18, doi: 10.1144/GSL.SP.2005.247.01.01.

Head, M.J., and Norris, G., 2003, New species of dinoflagellate cysts and other palynomorphs from the latest Miocene and Pliocene of DSDP Hole 603C, western North Atlantic: *Journal of Paleontology*, v. 77, no. 1, p. 1–15.

Head, M.J., Pillans, B., and Farquhar, S.A., 2008, The Early–Middle Pleistocene Transition: characterization and proposed guide for the defining boundary: *Episodes*, v. 31, no. 2, p. 255–259.

Hernandez-Almeida, Ivan., Sierro, F.J., Flores, J. A., Fillipelli, G. M, 2012, Paleoceanographic changes in the North Atlantic during the Mid-Pleistocene Transition (MIS 31-19) as inferred from planktonic foraminiferal and calcium carbonate records: *BOREAS an International Journal of Quaternary Research*. P. 1-20.

Kucera, M., 2007, Planktonic foraminifera as tracers of past oceanic environments: *Developments in Marine Geology*, Volume 1. P. 213-253

Lisiecki, L.E., and Raymo, M.E., 2005, A Pliocene–Pleistocene stack of 57 globally distributed benthic $\delta^{18}\text{O}$ records: *Paleoceanography*, v. 20, p. 1–17, doi:10.1029/2004PA001071.

Maslin, M.A., and Ridgwell, A.J., 2005, Mid-Pleistocene revolution and the “eccentricity myth”: In: Head, M.J., and Gibbard, P.L., *Early–Middle Pleistocene Transitions: the*

Land–Ocean Evidence; Geological Society, London, Special Publications, v. 247, p.19–34, doi: 10.1144/GSL.SP.2005.247.01.02

Mark A. Maslin, Christopher M. Brierley., 2015, The role of orbital forcing in the Early Middle Pleistocene Transition: *Quaternary International* xxx (2015) p. 1-9.

Mudelsee, M., Schulz, M., 1997, The Mid-Pleistocene climate transition: onset of 100 ka cycle lags ice volume build-up by 280 ka: *Earth and Planetary Science Letters* 151 p.117–123.

Naafs, B.D.A., Hefter, J., Ferretti, P., Stein, R., and Haug, G.H., 2011, Sea surface temperatures did not control the first occurrence of Hudson Strait Heinrich Events during MIS 16: *Paleoceanography*, v. 26, no. 4, p. 1–10, doi:10.1029/2011PA002135.

Naafs, B.D.A., Stein, R., Hefter, J., Khélifi, N., De Schepper, S., and Haug, G.H., 2010, Late Pliocene changes in the North Atlantic Current: *Earth and Planetary Science Letters*, v. 298, no. 3–4, p. 434–442, doi: 10.1016/j.epsl.2010.08.023.

Pospelova, V., de Vernal, A., and Pedersen, T.F., 2008, Distribution of dinoflagellate cysts in surface sediments from the northeastern Pacific Ocean (43–25°N) in relation to sea-surface temperature, productivity and coastal upwelling: *Marine Micropaleontology*, v. 68 (1–2), p. 21–48.

Pospelova, V., Esenkulova, S., Johannessen, S.C., O'Brien, M.C., and Macdonald, R.W., 2010, Organic-walled dinoflagellate cyst production, composition and flux from 1996 to 1998 in the central Strait of Georgia (BC, Canada): a sediment trap study: *Marine Micropaleontology*, v. 75, p. 17–37.

Pospelova, V., Pedersen, T.F., and de Vernal, A., 2006, Dinoflagellate cysts as indicators of climatic and oceanographic changes during the past 40 kyr in the Santa Barbara basin, southern California: *Paleoceanography*, v. 21 (2), doi:10.1029/2005PA001251.

Radi, T., de Vernal, A., 2008, Dinocysts as proxy of primary productivity in mid–high latitudes of the Northern Hemisphere: *Marine Micropaleontology* 68 p. 84–114.

Ravelo, C.A., Hillaire-Marcel, C., 2007, The Use of Oxygen and Carbon Isotopes of foraminifera in paleoceanography: *Developments in Marine Geology*, Volume 1, p. 735-760.

Rochon, A., de Vernal, A., Turon, J., Matthiessen, J., and Head, M.J., 1999, Distribution of recent dinoflagellate cysts in surface sediments from the North Atlantic Ocean and adjacent seas in relation to sea-surface parameters: AASP Contributions Series, no. 35, p. 1–152.

Shackleton, Nicholas J; Opdyke, Neil D (1973): Oxygen isotope and paleomagnetic stratigraphy of sediment core V28-239. doi:10.1594/PANGAEA.726599, Supplement to: Shackleton, NJ; Opdyke, ND (1973): Oxygen isotope and paleomagnetic stratigraphy of equatorial Pacific Core V28-238: oxygen isotope temperatures and ice volume on a 105 year and 106 year scale. *Quaternary Research*, 3, 39-55, doi:10.1016/0033-5894(73)90052-5

Stein, R., Kanamatsu, T., Alvarez-Zarikian, C., Higgins, S.M., Channell, J.E.T., Aboud, E., Ohno, M., Acton, G.D., Akimoto, K., Bailey, I., Bjorklund, H., Nielsen, S.H.H., Fang, N., Ferretti, P., Gruetzner, J., Guyodo, Y.J.B., Hagino, K., Harris, R., Hatakeda, K., Hefter, J., Judge, S.A., Kulhanek, D.K., Nanayama, F., Rashis, H., Sierro Sanchez, F.J., Voelker, A., Zhai, Q, 2006, North Atlantic Paleoceanography: The last five million years: *Eos*, Vol. 87, No. 13. p. 129-133.

Thorsteinsson, T., Waddington, D.E., Taylor, C.K., Alley, B.R. & Blankenship, D.D., 1999. Strain rate enhancement at Dye 3, Greenland, *J. Glaciol.*, 45, 338–345

Verleye, T.J., and Louwye, S., 2010, Recent geographical distribution of organic-walled dinoflagellate cysts in the southeast Pacific (25–53°S) and their relation to the prevailing hydrographical conditions: *Palaeogeography, Palaeoclimatology, Palaeoecology*, v. 298, no. 3–4, p. 319–340, doi: 10.1016/j.palaeo.2010.10.006.

Wetmore, K. 1997, <http://www.ucmp.berkeley.edu/fosrec/Wetmore.html>

Zonneveld, K.A.F., Versteegh, G.J.M., and de Lange G.J., 2001, Palaeoproductivity and post-depositional aerobic organic matter decay reflected by dinoflagellate cyst assemblages of the Eastern Mediterranean S1 sapropel: *Marine Geology*, v. 172, p.181–185.

Zonneveld, K.A.F., Bockelmann, F., and Holzwarth, U., 2007, Selective preservation of organic-walled dinoflagellate cysts as a tool to quantify past net primary production and bottom water oxygen concentrations: *Marine Geology*, v. 237, p. 109–126.

Zonneveld, K.A.F., Susek, E., and Fischer, G., 2010, Seasonal variability of the organic walled dinoflagellate cyst production in the coastal upwelling region off Cape Blanc (Mauritania): a five-year survey: *Journal of Phycology*, v. 46, p. 202–215.

Zonneveld, K.A.F., Marret, F., Versteegh, G.J.M., Bogus, K., Bonnet, S., Bouimetarhan, I., Crouch, E., de Vernal, A., Elshanawany, R., Edwards, L., Esper, O., Forke, S., Grøsfjeld, K., Henry, M., Holzwarth, U., Kielt, J.-F., So-Young, K., Ladouceur, S., Ledu, D., Chen, L., Limoges, A., Londeix, L., Lu, S.-H., Mahmoud, M.S., Marino, G., Matsouka[sic], K., Matthiessen, J., Mildenhall[sic], D.C., Mudie, P., Neil, H.L., Pospelova, V., Qi, Y., Radi, T., Richerol, T., Rochon, A., Sangiorgi, F., Solignac, S., Turon, J.-L., Verleye, T., Wang, Y., Wang, Z., and Young, M., 2013, Atlas of modern dinoflagellate cyst distribution based on 2405 datapoints: *Review of Paleobotany and Palynology*, v. 191, p. 1–197.

APPENDIX A PLATES

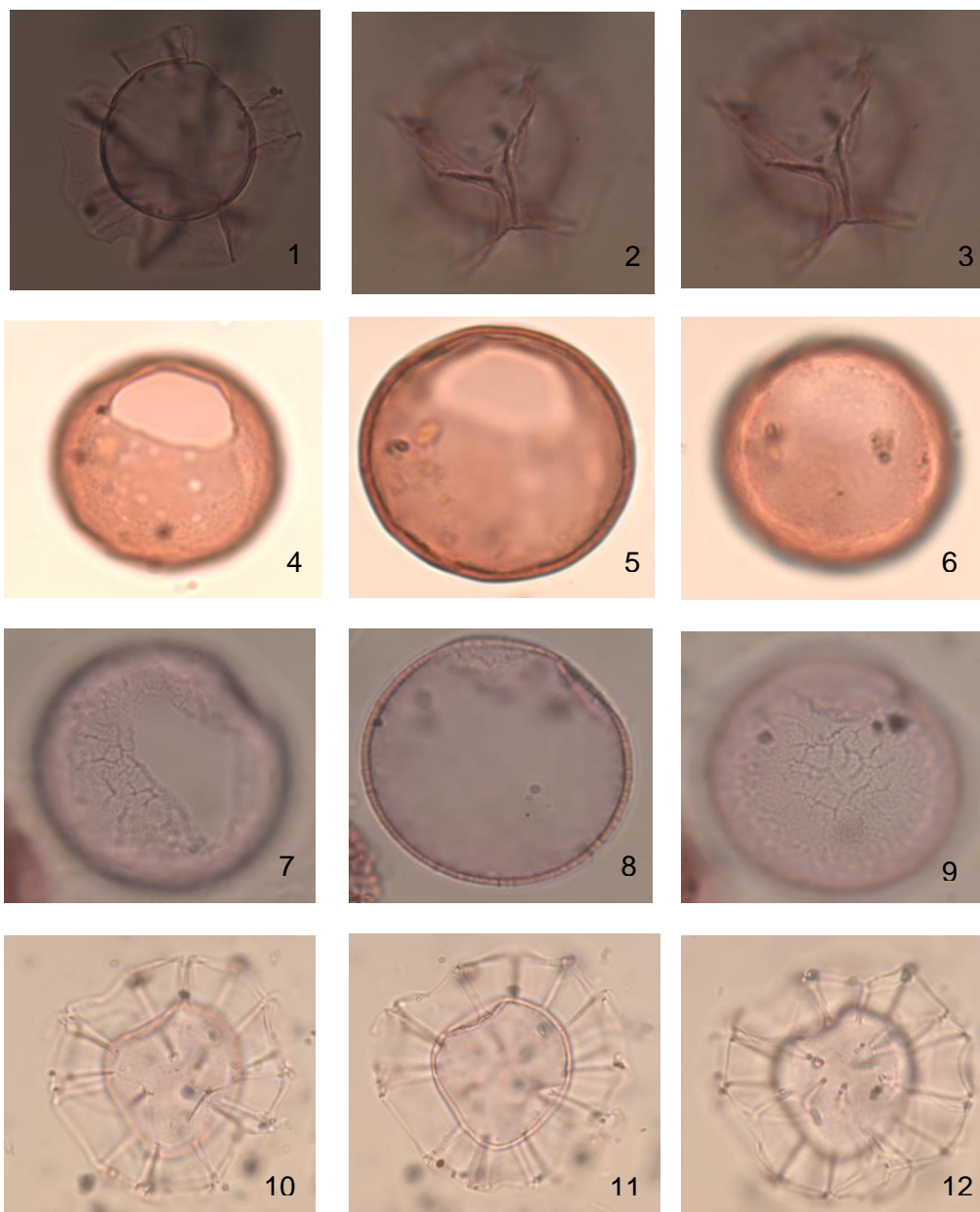


PLATE 1

Figs. 1–3: *Impagidinium cantabrigiense*. Central body: 40 μm . Sample ID: MD94; England Finder reference: P36/3.

Figs. 4–6: *Brigantedinium simplex*. Diameter of body 35 μm . Sample ID: MD94; England Finder reference: M45/2.

Figs. 7–9: *Pyxidinoopsis reticulata*. Diameter of body 40 μm . Sample MD94; England Finder reference: M28/0.

Figs. 10–12: *Nematosphaeropsis labyrinthus*. Diameter of central body 25 μm . Process length: 15 μm . Sample MD94; England Finder reference: M18/1.

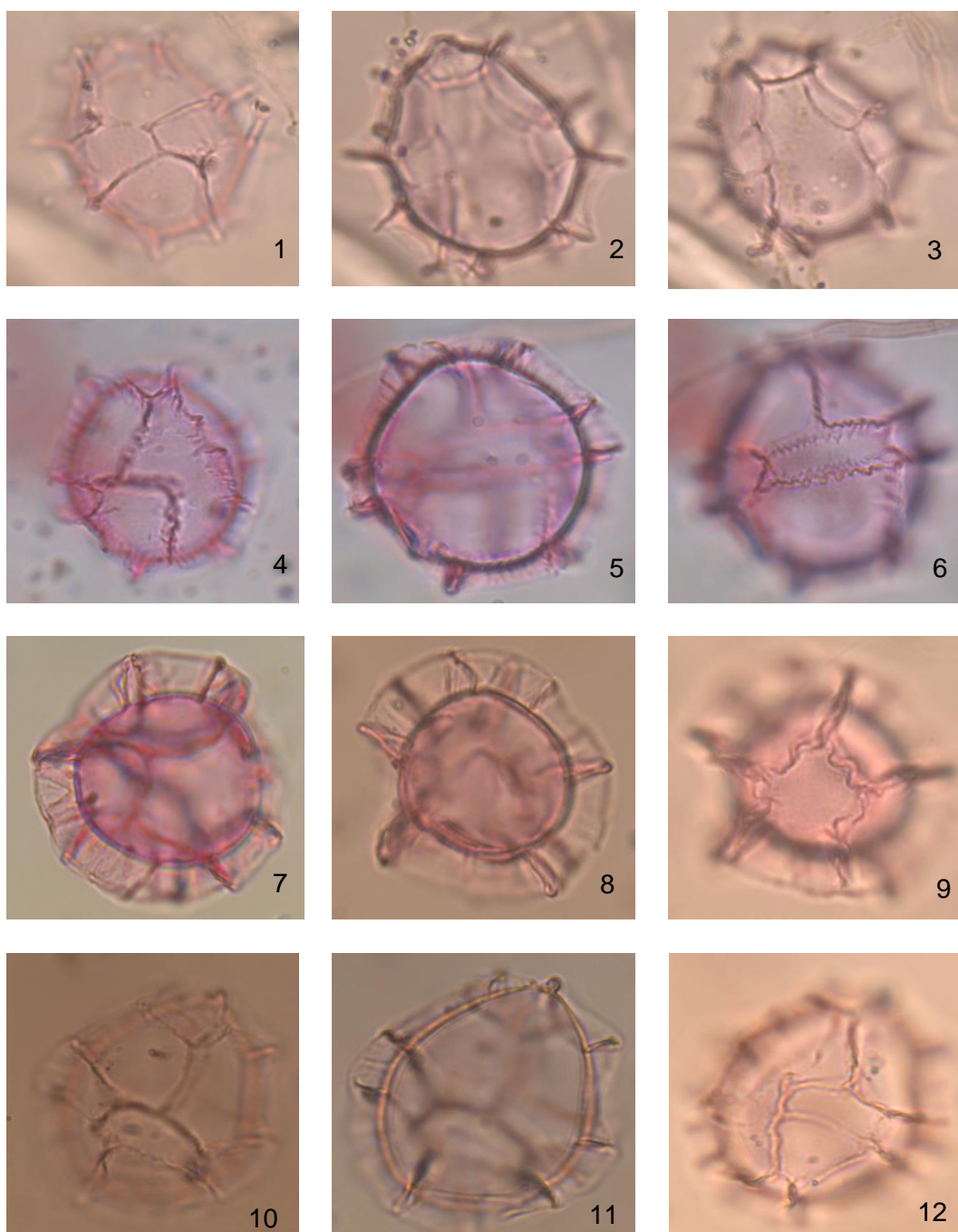


PLATE 2

Figs. 1–3: *Impagidinium aculeatum*. Dimensions of central body: 25x34 μm . Sample ID: MD94; England Finder reference: K34/3

Figs. 4–6: *Impagidinium plicatum*. Dimensions of central body: 20 μm . Sample ID: MD94; England Finder reference: K29/3

Figs. 7–9: *Impagidinium striatum*. Dimensions of central body: 25 μm . Sample ID: MD94; England Finder reference: K34/3

Figs. 10–12: *Impagidinium paradoxum*. Dimensions of central body: 20 μm . Sample ID: MD94; England Finder reference: K23/0.

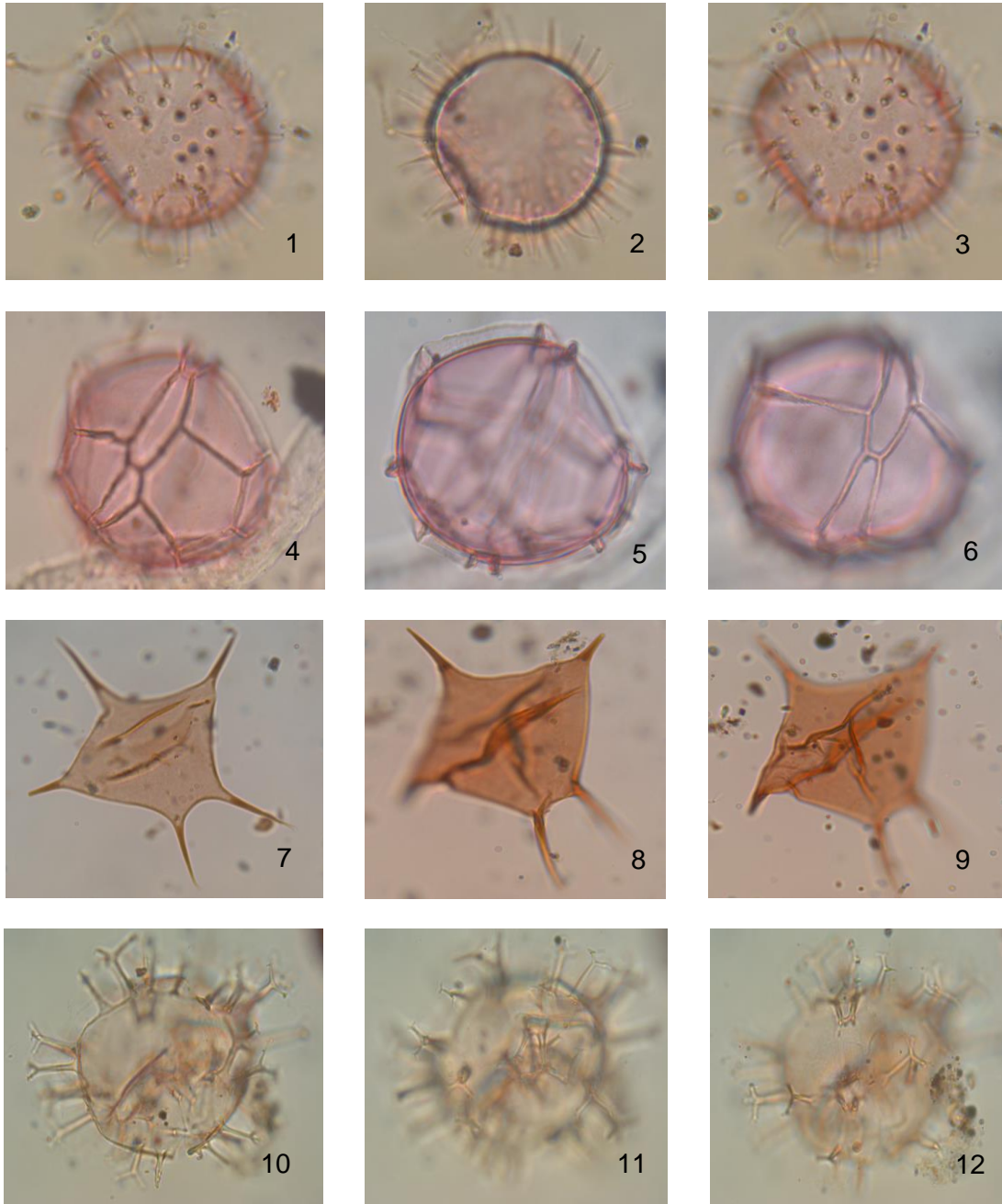


PLATE 3

Figs. 1–3: *Operculodinium centrocarpum* sensu Wall & Dale, 1966. Dimensions of central body: 30 μm . Process length 5 μm Sample ID: MD93; England Finder reference: L13/0.

Figs. 4–6: *Impagidinium patulum*. Diameter of central body: 65 μm . Crest length: 5 μm . Sample ID: MD93; England Finder reference: L26/3.

Figs. 7–9: Cyst of *Protoperidinium stellatum*. Body size: 65 μm . Sample ID: MD93; England Finder reference: P39/0.

Figs. 10–12: *Spiniferites hyperacanthus*. Diameter of central body: 50 μm . Process length: 15 μm . Sample ID: MD59; England Finder reference: R14/4

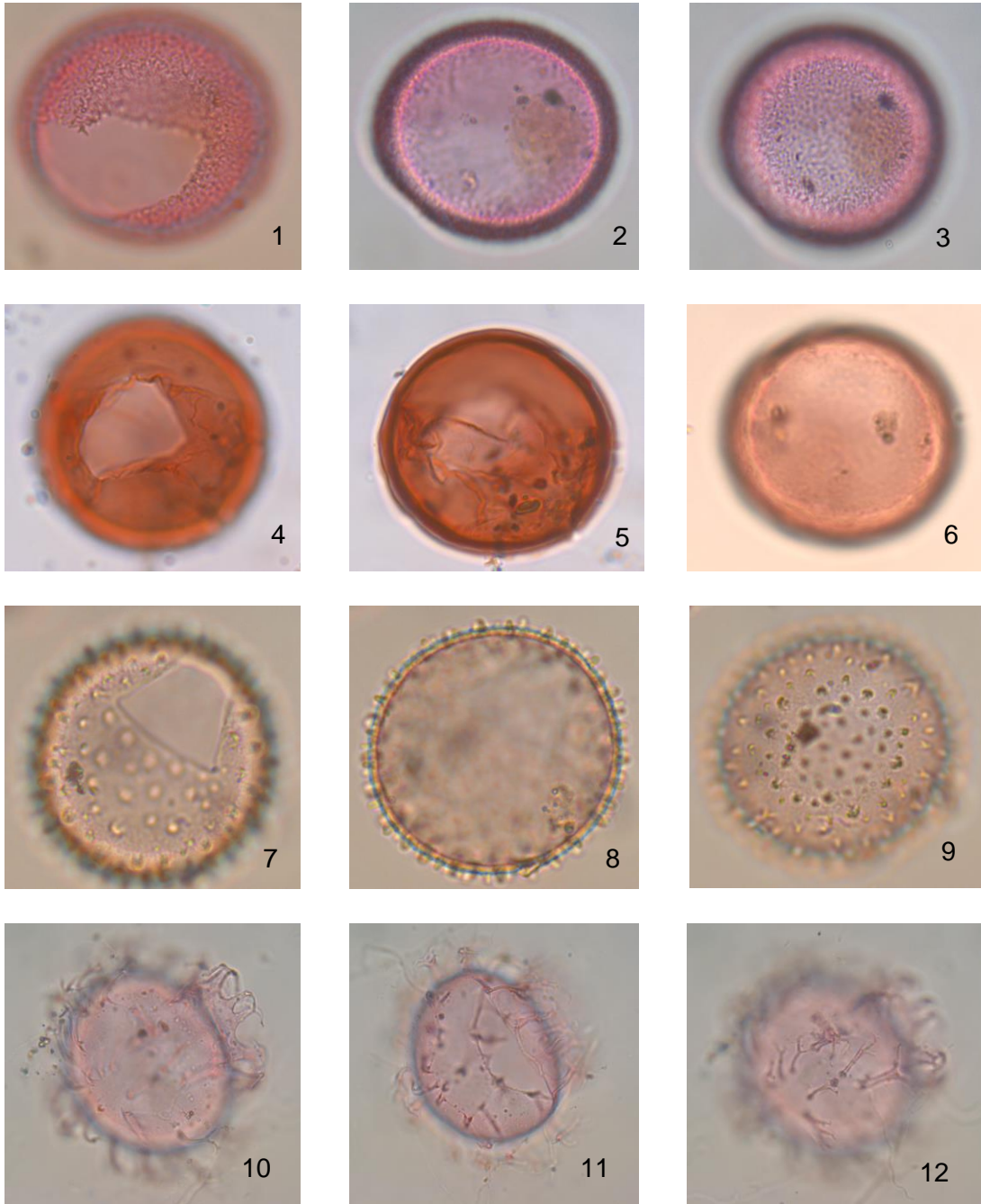


PLATE 4

Figs. 1–3: *Bitectatodinium tepikiense*. Diameter of cyst: 40 x 45 μm . Sample ID: MD03; England Finder reference: M17/4.

Figs. 4–6: *Brigantedinium cariacense*. Diameter of cyst 40 μm . Sample ID: MD05; England Finder reference: N24/0.

Figs. 7–9: “*Pyxidinoopsis striatoconulus*”. Diameter of central body: 35 μm . Process length: 1 μm . Sample ID: MD05; England Finder reference: M24/0.

Figs. 10–12: *Spiniferites mirabilis*. Diameter of central body: 60 μm . Process length: 20 μm . Sample ID: MD54; England Finder reference: K29/0.

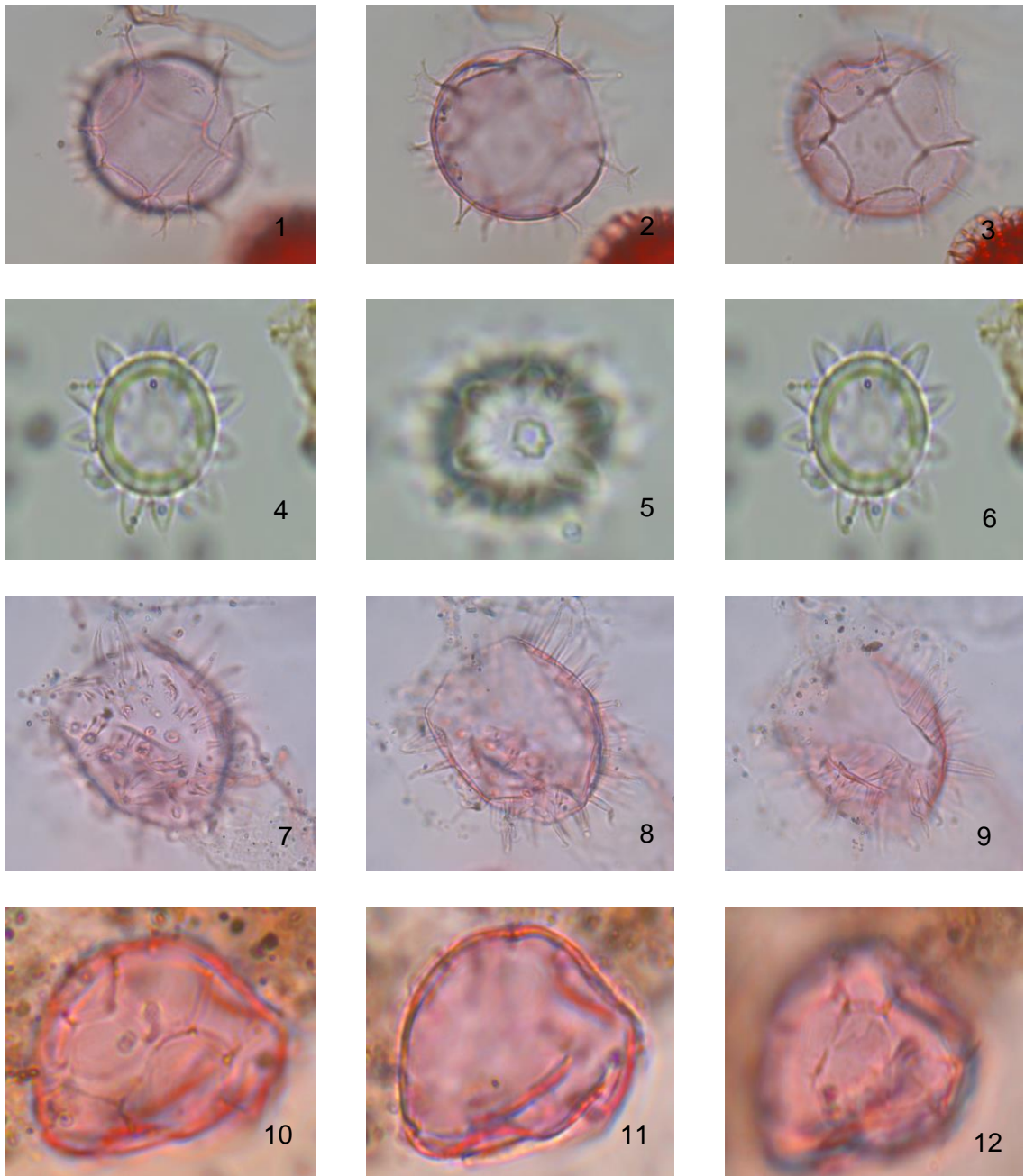


PLATE 5

Figs. 1–3: *Spiniferites* sp. 1. Diameter of central body: 35 μm . Process length: 5 μm . Sample ID: MD5403; England Finder reference: L14/4.

Figs. 4–6: Acritarch sp. 1 (ACR1). Diameter of central body: 15 μm . Process length: 3 μm . Sample ID: MD78; England Finder reference O15/0.

Figs. 7–9: *Lingulodinium machaerophorum*. Dimensions of central body: 60 x 50 μm . Process length: 20 μm . Sample ID: MD54; England Finder reference: N39/1.

Figs. 10–12: Acritarch sp. 2 (ACR2). Diameter of cyst: 25 μm . Sample ID: MD02; England Finder reference: N26/02.

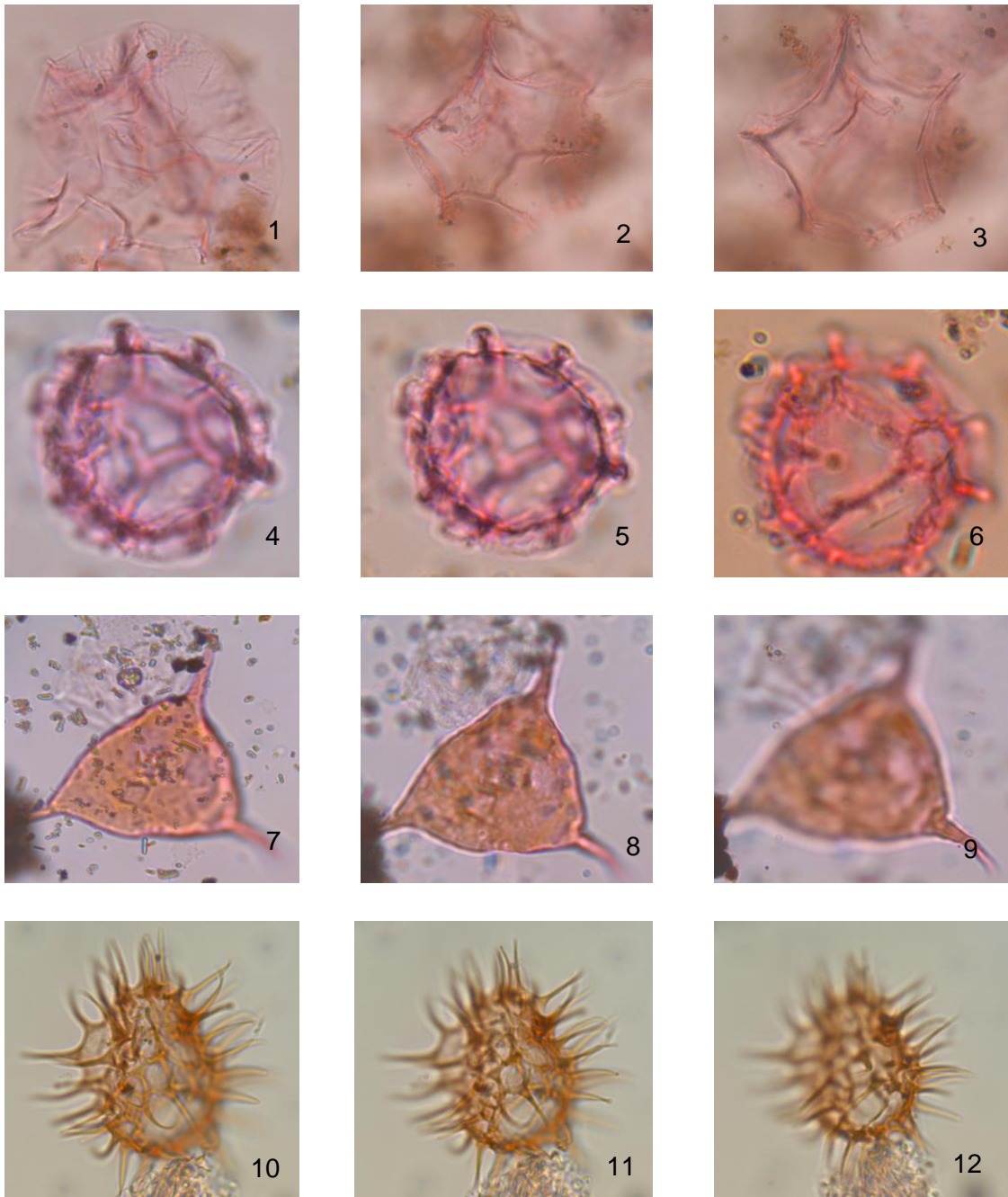


PLATE 6

Figs. 1–3: *Impagidinium pallidum*. Dimensions: 45 x 50 μm including crests. Crest length varies between 6 and 9 μm . Sample ID: MD02; England Finder reference: L24/2

Figs. 4–6: *Lavradosphaera* cf. *crista*. Diameter of central body: 20 μm . Crest length: 3 μm . Sample ID: MD02; England Finder reference: M40/2.

Figs. 7–9: *Veryhachium* sp. Dimensions: 30 μm from the process to the opposite edge. Sample ID: MD61; England Finder reference: R37/3.

Figs. 10–12: *Selenopemphix quanta*. Diameter: 30 μm . Sample ID: MD100; England Finder reference: K33/2.

APPENDIX B

PALYNOLOGICAL PROCESING AT BROCK UNIVERSITY

The following protocol for sample processing is adapted from methods already used at Brock University, with the specific aims of minimizing the loss of organic residue while maintaining the highest standards to prevent contamination. Minimizing processing losses is crucially important when the original sample size is small. The protocol described below, slightly modified from Abomriga (2018), was developed for deep-sea sediment samples that had been disaggregated in distilled water, and wet sieved at 63 μm to remove foraminifera for later geochemical analysis. The filtrate had been retained in a 1L glass beaker, allowed to settle, decanted, and dried. This dried sediment was scraped from the base of each glass beaker, and stored in plastic bags for future palynological analysis. The above preparation was conducted at the University of Cambridge under the direction of Dr Patrizia Ferretti who then supplied the dried sediment for the present study.

1. Wash 400 ml beakers in preparation for sample processing. First, soak in warm soapy water, then clean vigorously with a soft, non-abrasive cloth using non-abrasive soap. Clean with hot tap water and rinse thoroughly with distilled water to remove any tap water (which in the St. Catharines area comes from the Decew Falls Water Treatment Plant on a reservoir complex that includes lakes Moody and Gibson, adjacent to Brock University). The St Catharines tap water is likely to be contaminated with aquatic palynomorphs. A piece of parafilm is placed over the beaker to prevent airborne contamination prior to and during processing.

2. When the beakers are dry, remove any existing external markings with solvent. Using an indelible marker, number each beaker with a designated lab number (keeping the numbering simple, e.g. 1 to 24) in two places: high on one side and low on the opposite side (as a precaution). Write this number also on the sample bag to correlate

the sample number with the lab number. Note also in lab note book. If more than one person is using the lab, write initials on the beaker.

3. Crush the dried pieces of dried sediment gently between fingers in the plastic bag, breaking larger pieces into fragments of about 5 mm in diameter.

4. Place a paper baking cup onto the cleaned weighing plate of an electronic balance. Zero the balance. Transfer contents of the sample bag into the baking cup, and weigh the sediment. Note sample weight in grams to one decimal place.

5. Transfer contents of baking cup into a clean 400 ml beaker, ensuring that the sample is tipped gently onto the bottom of the beaker and thereby prevent a cloud of dust from forming. Dispose of empty baking cup. Re-seal beaker with Parafilm. Note that using a baking cup rather than pouring the sample directly from the sample bag into the beaker:

a) potentially reduces errors in weighing because of the minimal weight of the baking cup relative to the sample weight,

b) avoids the risk of transferring any contaminant from the outside of the bag into the beaker, and

c) allows the sample to be lowered gently to the base of the beaker.

6. When all samples have been weighed and placed in beakers, the beakers are transferred to the fume hood and small amounts of 20% conc. cold HCl are added in turn to each sample, using a squirt bottle. It is important to add the acid in minute increments to avoid any possibility of bubbling over. Gradually add 150 ml of acid to each beaker, swirling the sediment into suspension several times, and allow to stand overnight to dissolve all carbonates. Make sure that the Parafilm is securely attached to the top of the beaker.

7. After standing overnight, swirl the sediment into suspension and add distilled water

vigorously up to about 500 ml. Allow to stand for about 9 hours. Then vibrate the beaker by dragging briefly and by abrupt short twisting movements to flocculate any fine material adhering to the sides of the beaker as the result of electrostatic forces. Allow 3 more hours for this flocculant to settle.

8. Rinse a glass pipette with distilled water and connect it to the hose attached to the side of the siphon. Then open the faucet and allow water to run to produce suction (Venturi effect) through the pipette.

9. Carefully place the beaker next to the tap avoiding any abrupt movement or twisting that could bring sediment back into suspension; open the Parafilm cover and insert the pipette to suck the supernatant. While removing this supernatant, prevent the pipette from contacting the sides of the beaker to minimize the risk of contamination. Slowly begin tilting the beaker when the liquid reaches around 150 mL. This helps to prevent the tip of the pipette from getting too close to the sediment in the bottom. Remove the pipette when reaching the lowest safe level of supernatant to avoid any chance of losing sediment. Reseal beaker with Parafilm.

10. Rinse the tip of the pipette with tap water and allow re-circulation (tap water being sucked through the pipette), then repeat using distilled water. Keep the tap water running at all times to maintain the suction and prevent tap water back-flowing into the hose connected to the pipette.

11. Transfer the beaker to the fume hood and swirl the sediment back into suspension. Add distilled water vigorously up to 500 mL and allow to stand for 9 hours. Subsequently, repeat the procedure for flocculation mentioned in step 7.

12. Repeat steps 8 to 11 until reaching a pH of about 6 (pH of distilled water). When measuring the acidity, use one end of the pH paper to test the sample and add a small

amount of distilled water on the other end for comparison. Then, remove the supernatant as before.

13. Swirl the sediment into suspension and add 48% conc. cold HF up to 150 mL. Due to the hazardous nature of this acid, is essential to wear all the safety elements (lab coat, gloves, mask etc.) when manipulating it. Look for any drips at all times. If there is a suspicion of drips, rinse the affected area(s) with a sodium carbonate solution using a cloth. Also, dip gloves in this solution always before removing them from the fumehood.

14. Swirl the sediment into suspension 3 times a day for 5 days.

15. Twist and drag the beakers to produce flocculation of particles in the sides of the beaker. Allow to stand for three hours.

16. Peel back the Parafilm cover from the beaker. Make sure to avoid the drops condensed on its inner side since they could contain HF. Begin decanting the HF from the samples to a 1 L beaker by slow tilting to avoid any abrupt movement of the sediment that could bring it into suspension. Reverse the tilt if the sediment at the bottom of the beaker begins to cascade. Stop decanting if there is any chance of losing organic residue. Label a plastic bottle with "Waste HF" and then transfer the content of the 1 L beaker to this bottle. It is important not to accumulate too much HF in the 1 L beaker. Hence, it is recommended that the decanted acid be transferred to the waste HF bottle after every other sample.

17. Swirl beakers to bring the residue into suspension and add distilled water up to around 500 mL and allow to stand overnight.

18. Repeat steps 15 and 16 until the supernatant is neutral.

19. Label 50 mL screw-top disposable conical test tubes with the same designated lab number used in the beakers. Label in two different places: high on one side and low on the opposite side. Also label the screw top.
20. Decant the supernatant and transfer the residue from the beaker to a 50 mL test tube. Make sure the number in the test tube matches the number on the beaker.
21. Add about 40 mL of HCl to the test tubes and allow stand for 3 hours. This helps to remove any precipitates formed during HF treatment. Then fill the tubes with distilled water.
22. In a centrifuge, set the RPM at 3500 and spin the test tubes for 3 minutes, then remove the supernatant. Repeat until reaching a pH of 6, this being the pH of distilled water.
23. Add the desired number of *Lycopodium clavatum* tablets (usually around 1 to 3 per 10 grams of dry sediment) to each sample and dissolve them adding some HCl. Is important to aim approximately for an ideal ratio of dinoflagellate cysts to spores of *L. clavatum*, but this requires estimating the dinocyst concentration in advance which is best achieved by consulting previous studies of dinocysts under similar settings. Fill the test tube with distilled water after the tablet(s) is (are) completely dissolved.
24. Spin down the samples using the same parameters mentioned in step 22. Then, remove approximately 3/4 of the supernatant and mix the residue using the vortex mixer being careful always to bring all the residue into suspension.
25. Sieve the sediment using a 10 μ m nylon mesh. After sieving, make a wet preparation to see if ultrasound treatment is needed due to high amounts of AOM. Also it is possible to add more *Lycopodium* tablets at this point if necessary. Then transfer the sieved material to a 15 mL test and add two drops of stain if desired. Mix the

material with the stain using the vortex mixer then sieve again to remove superfluous stain. Transfer the residue back to the 15 mL test tube.

26. Place a cover slip on a slide warmer and using a pipette add 2 or 3 drops of glycerine jelly and 6 drops of distilled water. Mix using a toothpick or cocktail stick. Make sure to cover all the cover slip's surface with the mix. Use a pipette to mix the sieved residue thoroughly, and promptly transfer about 10 drops of residue evenly over the cover slip, then cover the slide warmer and let the cover slip dry for at least an hour.

27. Ensure that all superfluous water has evaporated from the cover slip. This can be done by placing a cold microscope slide over the cover slip to check for condensation. Put approximately 12 drops of glycerine jelly on a microscope slide and carefully invert the cover slip onto the glucerine jelly, avoiding any air bubbles from becoming trapped. Then remove the microscope slide quickly from the slide warmer and let it rest horizontally for a few hours. Slide-making follows the methodology of Evitt (1984).